Titre: Title:	Three Dimensional Inversion of Magnetic Survey Data Collected Over Kimberlite Pipes in Presence of Remanent Magnetization
Auteur: Author:	Pengzhi Zhao
Date:	2012
Type:	Mémoire ou thèse / Dissertation or Thesis
Référence: Citation:	Zhao, P. (2012). Three Dimensional Inversion of Magnetic Survey Data Collected Over Kimberlite Pipes in Presence of Remanent Magnetization [Mémoire de maîtrise, École Polytechnique de Montréal]. PolyPublie. https://publications.polymtl.ca/941/

Document en libre accès dans PolyPublie
Open Access document in PolyPublie

URL de PolyPublie: PolyPublie URL:	https://publications.polymtl.ca/941/
Directeurs de recherche: Advisors:	Michel C. Chouteau
Programme: Program:	Génie minéral

UNIVERSITÉ DE MONTRÉAL

THREE DIMENSIONAL INVERSION OF MAGNETIC SURVEY DATA
COLLECTED OVER KIMBERLITE PIPES IN PRESENCE OF REMANENT
MAGNETIZATION

PENGZHI ZHAO

DÉPARTEMENT DES GÉNIES CIVIL, GÉOLOGIQUE ET DES MINES

ÉCOLE POLYTECHNIQUE DE MONTRÉAL

MÉMOIRE PRÉSENTÉ EN VUE DE L'OBTENTION
DU DIPLÔME DE MAÎTRISE ÈS SCIENCES APPLIQUÉES

(GÉNIE MINÉRAL)

AOÛT 2012

UNIVERSITÉ DE MONTRÉAL

ÉCOLE POLYTECHNIQUE DE MONTRÉAL

Ce mémoire intitulé:

THREE DIMENSIONAL INVERSION OF MAGNETIC SURVEY DATA COLLECTED
OVER KIMBERLITE PIPES IN PRESENCE OF REMANENT MAGNETIZATION

Présenté par: ZHAO Pengzhi

en vue de l'obtention du diplôme de: Maîtrise ès sciences appliquées

a été dûment accepté par le jury d'examen constitué de:

M. JI Shaocheng, Ph.D., président

M. CHOUTEAU Michel, Ph.D., membre et directeur de recherche

M. VALLÉE Marc-Alex, Ph.D., membre

To my parents Yong Zhao and Shuhua Yu

To my wife Huicong Zhang

ACKNOWLEDGMENTS

Here, I would like to express my sincere gratitude to all the people who have helped me during my master study. Without their help, I am sure that I will not accomplish my master degree.

Foremost, I am grateful to my supervisor, Professor Michel Chouteau. He is an exceptional individual, with a vast knowledge of geophysics, and I truly appreciate the invaluable insight he has provided me during the research and writing process. In particular, I am thankful for the countless hours of his guidance, encouragement, and help during my master study. Furthermore, without his acceptance and financial support, I could not come to Canada to study.

I would like to thank the Ecole Polytechnique de Montreal. The school provides the perfect learning environment. I acknowledge China Scholarship Council for the exemption of my foreign student tuition fees.

Special mention must also give to the members of group of geophysics. Thanks for their support and smile. When I meet the problem during my research, they answer my questions and offer suggestions with all their forces.

I also want to thanks all my friends in Canada and in China. Accompanied by them, my study life will be unforgettable memory though out my life.

With all of my love, I must thank my family for their unconditional love, support and trust.

RÉSUMÉ

La méthode magnétique est une technique géophysique couramment utilisée pour explorer les kimberlites. L'analyse et l'interprétation des données magnétiques fournissent les informations des propriétés magnétiques et géométriques des cheminées de kimberlite détectées. Un paramètre crucial de l'interprétation magnétique des kimberlites est l'aimantation rémanente, parce que le classement des kimberlites est dominé par la rémanence. Toutefois, l'aimantation rémanente entrave l'interprétation des données magnétiques et elle détermine la quantité difficilement. La présence de l'aimantation rémanente peut poser des défis dans l'interprétation quantitative des données magnétiques quand les anomalies magnétiques sont inclinées ou déplacées latéralement par rapport à la source située sous la surface (Haney et Li, 2002). Par conséquent, l'identification des effets de rémanence et la détermination de l'aimantation rémanente sont importantes dans l'interprétation magnétique.

Ce projet présente une méthode pour déterminer les propriétés magnétiques et géométriques des cheminées de kimberlite en présence d'aimantation rémanente forte. Cette méthode se compose de deux étapes. La première étape consiste à estimer l'aimantation totale et les propriétés géométriques de l'anomalie magnétique. La deuxième étape consiste à séparer l'aimantation rémanente de l'aimantation totale.

Dans la première étape, le signal analytique est dérivé à partir des données magnétiques par filtrage dans le domaine de Fourier; par la suite, l'inversion paramétrique pour obtenir l'aimantation totale et les propriétés géométriques d'anomalie magnétique est réalisée. L'algorithme d'inversion est basé sur la méthode de Gauss-Newton et combine l'intensité du champ magnétique total et son signal analytique. L'inversion conjointe du champ magnétique et du signal analytique a été testée avec des données synthétiques et appliquée pour interpréter les anomalies magnétiques de kimberlites du Lac de Gras, Territoires du Nord-Ouest, au Canada.

Les résultats obtenus sur les exemples synthétiques et sur les données réelles montrent que l'algorithme d'inversion conjointe du champ magnétique et du signal analytique permet une bonne détermination des paramètres géométriques et physiques. L'algorithme développé est robuste et stable.

Dans la deuxième étape, la méthode électromagnétique fréquencielle est utilisée pour estimer la susceptibilité magnétique de la structure magnétique, et de séparer l'aimantation remanente de l'aimantation totale en utilisant une formulation mathématique simple. La susceptibilité est calculée à l'aide du code d'inversion électromagnétique dans le domaine de fréquence "EM1DFM", qui a été publié par l'Université de Colombie Britannique. Il a été conçu pour déterminer des modèles 1D de la susceptibilité magnétique et de la conductivité électrique, en utilisant n'importe quel type de données mesurées par un systéme dipolaire, et en utilisant l'une des quatre variantes de l'algorithme d'inversion.

La méthode décrite propose une nouvelle idée pour déterminer les propriétés magnétiques et géométriques de cheminées de kimberlite en présence d'aimantation rémanente forte. L'inversion conjointe du champ magnétique et du signal analytique permet de surmonter l'influence de l'aimantation rémanente et d'obtenir l'aimantation totale et les propriétés géométriques. La précision et la stabilité de l'inversion conjointe sont accrues par rapport à celles obtenues avec l'inversion du champ magnétique et de l'inversion du signal analytique séparément. La technique électromagnétique permet la détermination de la susceptibilité de sorte que l'aimantation rémanente est séparée de l'aimantation totale.

ABSTRACT

Magnetic method is a common geophysical technique used to explore kimberlites. The analysis and interpretation of measured magnetic data provides the information of magnetic and geometric properties of potential kimberlite pipes. A crucial parameter of kimberlite magnetic interpretation is the remanent magnetization that dominates the classification of kimberlite. However, the measured magnetic data is the total field affected by the remanent magnetization and the susceptibility. The presence of remanent magnetization can pose severe challenges to the quantitative interpretation of magnetic data by skewing or laterally shifting magnetic anomalies relative to the subsurface source (Haney and Li, 2002). Therefore, identification of remanence effects and determination of remanent magnetization are important in magnetic data interpretation.

This project presents a new method to determine the magnetic and geometric properties of kimberlite pipes in the presence of strong remanent magnetization. This method consists of two steps. The first step is to estimate the total magnetization and geometric properties of magnetic anomaly. The second step is to separate the remanent magnetization from the total magnetization.

In the first step, a joint parametric inversion of total-field magnetic data and its analytic signal (derived from the survey data by Fourier transform method) is used. The algorithm of the joint inversion is based on the Gauss-Newton method and it is more stable and more accurate than the separate inversion method. It has been tested with synthetic data and applied to interpret the field data from the Lac de Gras, North-West Territories of Canada. The results of the synthetic examples and the field data applications show that joint inversion can recovers the total magnetization and geometric properties of magnetic anomaly with a good data fit and stable convergence.

In the second step, the remanent magnetization is separated from the total magnetization by using a determined susceptibility. The susceptibility value is estimated by using the frequency domain electromagnetic data. The inversion method is achieved by a code, named "EM1DFM", developed by University of British Columbia was designed to construct one of four types of 1D model, using any type of geophysical frequency domain loop-loop data with one of four variations of the inversion algorithm. The results show that the susceptibility of magnetic body is recovered, even if the depth and thickness are not well estimated.

This two-step process provides a new way to determine magnetic and geometric properties of kimberlite pipes in the presence of strong remanent magnetization. The joint inversion of the total-field magnetic data and its analytic signal obtains the total magnetization and geometric properties. The frequency domain EM method provides the susceptibility. As a result, the remanent magnetization can be separated from the total magnetization accurately.

TABLE OF CONTENTS

LIST OF TABLES

LIST OF FIGURES

LIST OF SYMBOLS AND ABBREVIATIONS

f	Total-field magnetic anomaly
g	Analytic signal
$\vec{J}_{tot}$	Total magnetization
$\vec{J}_i$	Induced magnetization
$\vec{J}_r$	Remanent magnetization
J_{tot}	Intensity of total magnetization
J_i	Intensity of induced magnetization
J_r	Intensity of remanent magnetization
I_{tot}	Inclination of total magnetization
I_i	Inclination of induced magnetization
I_r	Inclination of remanent magnetization
D_{tot}	Declination of total magnetization
D_i	Declination of induced magnetization
D_r	Declination of remanent magnetization
Q	Königsberger ratio
κ	Magnetic susceptibility
μ	Magnetic permeability
μ_0	Magnetic permeability of vacuum
σ	Electric conductivity
TM	Total magnetization
IM	Induced magnetization

RM	Remanent magnetization
JIMA	Joint inversion of magnetic field and analytic signal
MFI	Magnetic field inversion
ASI	Analytic signal inversion
Mag.	Total magnetization intensity
In.	Total inclination of the magnetic field
De.	Total declination of the magnetic field
Dia.	Diameter of the cylinder
Dep.	Depth of the cylinder
RMS	Root mean squares error
Dep.	Depth of the cylinder
β	Trade-off parameter
λ	Damping factor
Nor	Normalization factor
SI	International system

INTRODUCTION

Diamond is the fifth mineral in economic importance after iron, gold, copper and zinc (Baumier, 1993). The diamond is generally found in two types of rock: kimberlite and lamproite. The total volume of known kimberlite in the world is more than 5,000 cubic kilometers and lamprophyre in the world is less than 100 cubic kilometers (Mitchell and Bergman, 1991). Most of diamonds are extracted from kimberlite rocks.

The definition for kimberlite was present by Mitchell (1986): inequigranular alkalic peridotites containing rounded and corroded megacrysts of olivine, phlogopite, magnesian ilmenite and pyrope set in fine grained groundmass of second generation euhedral olivine and phlogopite together with primary and secondary diamond. The surrounding rock of kimberlite can be any sedimentary, metamorphic or igneous. Mitchell (1986) provided an idealized kimberlite model (Figure 1.1) that illustrates the relationships between crater, diatreme and hypabyssal facies rocks. The diatreme root zone is composed primarily of hypabyssal rocks. The diameter of kimberlite pipe is from a few meters to hundreds of meters, and the depth extent is from a few meters to thousands of meters.

Macnae (1995) describes the geometry of kimberlite pipe: "kimberlites tend to have circular, ellipsoidal or kidney shaped shallow expressions in plan. The least eroded pipes (generally larger in surface area) will have shallower dips at the pipe walls than more deeply eroded pipes. Geophysical modeling should not require a non-vertical dip for the axes of a pipe. Blind secondary or satellite pipes on the other hand may, however, cause response asymmetries. " The classical model of a pipe is a carrot shaped or conical geometry with steeply dipping walls and diameter vanishing with increasing depth (Skinner, 1986) as in Figure 1.1.
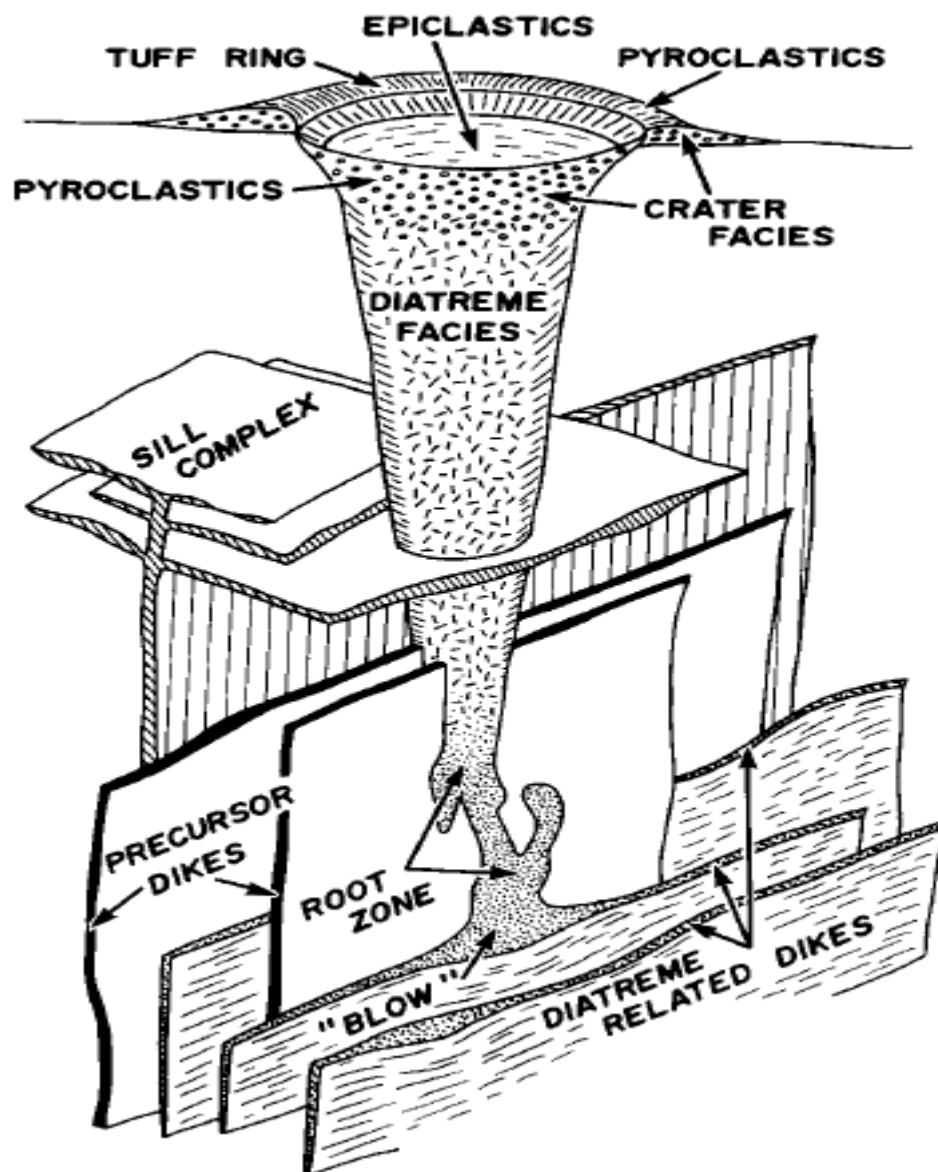
Figure 1.1: Model of an idealized kimberlite magnetic system illustrating the relationships between crater, diatreme and hypabyssal facies rocks. The diatreme root zone is composed primarily of hypabyssal rocks (After Mitchell, 1986).

The magnetic properties are an important feature of kimberlite, because the magnetism of igneous rocks is larger than metamorphic rock or sedimentary rock generally. The existing geophysical literature in rock magnetism (Clark, 1983; Hargraves, 1989) shows that the kimberlite magnetic response is mainly caused by the direction and amplitude of remanent magnetization (RM in brief for the remaining of the thesis). For example, Hargraves (1989) The magnetic properties are an important feature of kimberlite, because the magnetism of igneous

rocks is larger than metamorphic rock or sedimentary rock generally. The existing geophysical literature in rock magnetism (Clark, 1983; Hargraves, 1989) shows that the kimberlite magnetic response is mainly caused by the direction and amplitude of remanent magnetization (RM in brief for the remaining of the thesis). For example, Hargraves (1989) published extensive paleomagnetic results over kimberlites in Southern Africa, and determined that RM was very consistent in direction within each sampled pipe.

Because of the magnetic properties of kimberlite, magnetic method is one of the most useful geophysical techniques to accurately determine the geometrical and magnetic properties, such as pipe shape, depth to top, magnetization. The magnetics show not only high sensitivity to kimberlite occurrence, but also it is relatively low cost and highly efficient, especially the airborne magnetics.

Magnetic interpretation provides information about the magnetization, location and size of the kimberlite pipe. A crucial parameter of kimberlite magnetic interpretation is the RM which dominates the classification of kimberlite, but the presence of RM can pose severe challenges to the quantitative interpretation of magnetic data by skewing or laterally shifting magnetic anomalies relative to the subsurface source (Haney and Li, 2002).

When the strong RM is present, the magnetic data is responding to total magnetization (TM in brief for the remaining of the thesis), which is consisted of a variety set of induced magnetization (IM in brief for the remaining of the thesis) and RM. However, the RM cannot be estimated directly or separated from the TM just utilizing the magnetic interpretation. Most of the methods use the mathematical relationships or direction bias to estimation the RM, such as minimizing the amplitude of RM. These methods can't estimate RM with certainty, because the RM not only biases the direction of TM but also change its magnitude. Figure 1.2 shows an example to explain this problem. If the TM is known, both magnitude and direction of RM are changed ($\vec{J}_r$ changes to the $\vec{J}_r'$) when the magnitude of IM changes ($\vec{J}_i$ changes to the $\vec{J}_i'$). Therefore, the magnitude of IM or susceptibility must be known when the remanent magnetization has to be separated from the TM.
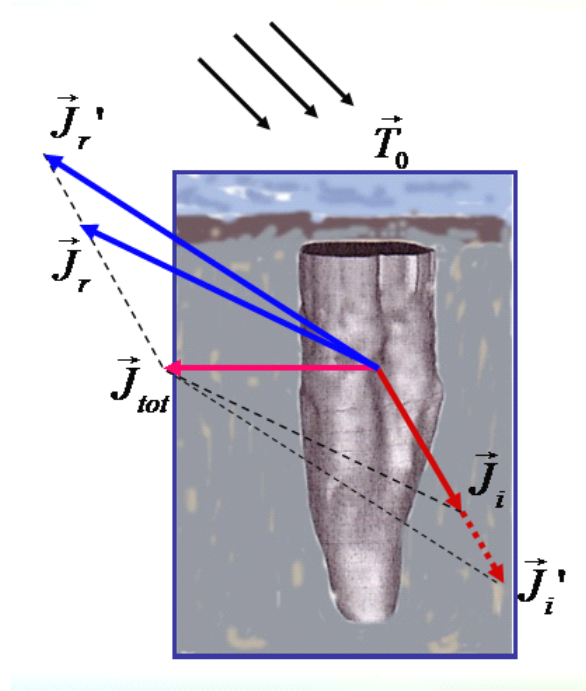
Figure 1.2: Relations between the remanent magnetization and induced magnetization when the total magnetization is known.

The objective of my thesis is to determine the RM and geometrical properties of kimberlite pipe. Furthermore, the magnetic interpretation method must be stable in presence of different typical noises.

To achieve this objective, I use a two-step strategy to interpret the magnetic data. The first step is to determine the TM from the total magnetic data in presence of strong RM. The second step is to obtain the magnetic susceptibility and then to separate the RM from the TM.

A three-dimensional (3D) parametric inversion algorithm was developed to determine the TM and geometrical properties of kimberlite pipe by using the magnetic total-field anomaly and its analytic signal in presence of strong RM. In general magnetic interpretation, the direction of magnetization is identical to the one of the geomagnetic field. However, the strong RM changes the direction of magnetization and generates the "false targets". The parametric inversion is a mean to solve this problem, because the direction of magnetization is independent on the geomagnetic field that is one of parameters to be interpreted.

For the interpretation of magnetic survey data collected over kimberlite, the parametric inversion assumes that a single magnetic body is present in selected area. However, the magnetic

anomaly can be affected with geological and processing noise, regional anomaly, interfering anomalies from other magnetic bodies. Thus the inversion algorithm needs to overcome those effects. The analytic signal is therefore used to improve interpretation of the magnetic data, because its sensitivity is different to total-field magnetic data in presence of noise. The joint inversion of the total magnetic field and the analytic signal is superior over the separated inversion of each set of data. It increases the resolution and stability of the results. The inversion algorithm uses Gauss-Newton method solved by singular value decomposition and Marquardt's method.

As mentioned above, the RM cannot be estimated uniquely, unless the susceptibility is known. Traditionally, the RM or susceptibility of minerals and rocks are measured from orientated cores and active source experiments. However, these methods are not always feasible and have limitations because of its cost and they are time consuming (Shearer, 2005). Fortunately, the susceptibility can be estimated by using electromagnetic method, which is not affected by RM. The 1D inversion of EM data proposed by Zhang and Oldenburg (1996) is used to estimate the magnetic susceptibility and the electric conductivity. Then, the RM can be separated from the TM according to the relationship between the RM, susceptibility and TM.

In order to verify the joint inversion of magnetic field and analytic signal, four different synthetic models are used. The first model is a vertical cylinder at an intermediate depth, an inclination and a declination close to the geomagnetic inclination and declination. The second model is an intermediate depth vertical cylinder with inclination and declination differing with the Earth's field inclination and declination. The third model is a shallow large diameter vertical cylinder with inclination and declination differing with the Earth's field inclination and declination. The fourth model is a deep small diameter vertical cylinder similar to a vertical dipole, its inclination closes to the vertical and its declination closes to the Earth's field declination.

The main scientific contributions from my thesis are: (1) the analytic signal is derived by using Fourier transform method; (2) a joint inversion of magnetic field and analytic signal is implemented, which adds stability and precision to the solution; (3) the magnetic technique and EM technique are combined to separate the RM from the TM.

There are five chapters in this thesis:

Chapter 1 is an overview of the magnetic techniques. I introduce the history and concepts of magnetics and illustrate the main interpretation methods including the one with strong RM. Then I present development of magnetic technique for detecting the kimberlite.

Chapter 2 describes the analytic signal methodology that contains the basic principle of analytic signal and its calculations. First, I introduce the theory of analytic signal and the expression of its absolute value. Then, I review the expression of magnetic total-field anomaly due to a vertical right circular cylinder. After that, I introduce the computational method to obtain the analytic signal by Fourier transform. Finally, I illustrate the algorithm with synthetic examples.

Chapter 3 describes the inversion methodology that contains the theory and computation of joint inversion of magnetic field and analytic signal. Firstly, I introduce the inversion theory to solve the general problem. Then, I present the specific computation and structure diagram to complete the joint inversion of the magnetic total-field anomaly and its analytic signal due to a vertical right circular cylinder with arbitrary polarization. Finally, I illustrate the algorithm with synthetic examples.

Chapter 4 examines how to resolve the RM. I first introduce the RM computation from the TM and IM. Then the frequency EM survey is proposed to estimate the magnetic susceptibility. Finally, I illustrate the algorithm with synthetic examples.

Chapter 5 examines the performance of the joint inversion using synthetic tests. It discusses the advantages and usability of joint inversion of magnetic field and analytic signal. First, all model responses of total-field magnetic data and its analytic signal are contaminated with Gaussian noise only. Then, the regional noise is added. After that, I also consider a model response generated by two pipes and contaminated with Gaussian noise. Finally, a field example is used to illustrate the usability of joint inversion of magnetic field and analytic signal.

CHAPTER 1   BACKGROUND

The purpose of this chapter is to briefly overview the developments magnetic techniques. Firstly, I introduce the history and concepts of magnetics. Then, I illustrate main methods of magnetic interpretation. After that, I introduce methods to interpret magnetic data with strong RM. Lastly, I present development of magnetic technique for detecting the kimberlite.

1.1 Concept of magnetics

The magnetism was used for navigation as early as several centuries B.C in China, and recognized Earth's field by 11th century. In end of 12th century, the magnetic compass was developed in Europe. The magnetics method has become a geophysical exploration technique first studied by occidental scientists since William Gilbert (1544-1603), who is regarded by some as the father of magnetism and published "De Magnete" in 1960. He carved sphere from lodestone and found field similar to Earth's. In the middle of seventeen century, Swedish geophysicists have used magnetic compass to detect magnetite. Until 1843, Von Wrede first used variations in the field to locate deposits of magnetic ore. In 1879, Thalen examined magnetite deposits with magnetics. The magnetics is used variations of the magnetic field were used to map the distribution of magnetic materials buried underground. Schmidt invented the quartz blade magnetometer and since then magnetics have been used for mineral exploration at large in 1915. In the 1940s, the vertical component of magnetic field has been measured. After World War Second, the Fluxgate magnetometer was invented that made the aeromagnetic measurement possible, and aeromagnetic measurement became popular in geophysical exploration later. After that, Proton-precession magnetometers and Optically pump alkali-vapor magnetometers came out, caused the measurements more accurate. At present, the digital technique is using in recording and processing of magnetic data.

1.1.1 Magnetic elements

In general, the magnetic field could be described by rectangular coordinates. Supposed that origin of coordinate is observation point, x-axes directs north, y-axes directs east, z-axes directs the Earth's core. The magnetic features of this point can be expressed by seven magnetic

elements. Figure 1.2 presents the geometrical relationship of magnetic elements, and the expressions of the relationships of magnetic elements are written as follow:
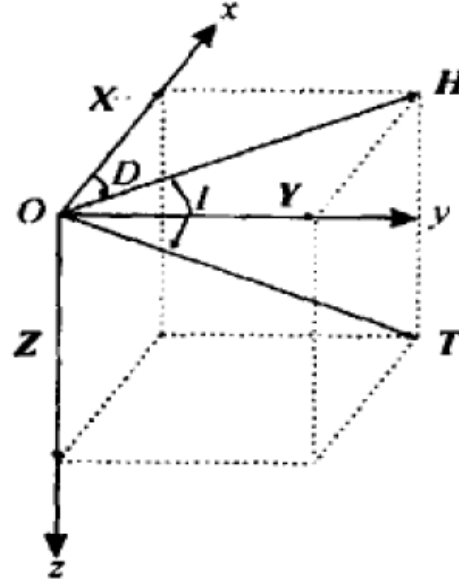
Figure 1.3: Geometry relationship of magnetic elements. Inclination (I) is the angle between the magnetic field vector and the local horizontal plane of the Earth. Declination (D) is the angle between the magnetic field projections to the Earth's surface and geographic north.

$$\begin{cases} T^2 = H^2 + Z^2 = X^2 + Y^2 + Z^2 \\ X = H\cos D, \quad Y = H\sin D, \quad \tan D = Y/X \\ H = T\cos I, \quad Z = T\sin I, \quad \tan I = Z/H \end{cases}$$

$$(1.2.1\text{-}1)$$

where, T is the magnetic intensity vector, H is the horizontal component of T, Z is the vertical component of T, X is the x axes component of T, Y is the y axes component of T, I is the inclination which is the angle between the magnetic field vector and the horizontal plane. D is the declination, which is the angle between Geographical meridional plane and the horizontal component of magnetic field vector. The unit of T, H, X, Y, Z is Tesla (T) in SI system and gamma (γ) in cgs system ($1T = 1Wb/m^2$, $1\gamma = 1nT = 10^{-9}T$).

According to the expressions of magnetic elements, all the elements can be expressed by arbitrarily three elements. The magnetic intensity vector, inclination and declination are generally used in magnetic exploration.

1.1.2 Magnetization

Material in magnetic field produces magnetic phenomenon calls magnetization. It is a function of location and varies from point to point (Blakeley, 1996). Different materials in the same magnetic field or same materials in the different magnetic field are magnetized differently. Magnetization can be defined according to the following equation:

$$\vec{J} = \frac{\sum \vec{m}}{\Delta V}$$

(1.2.2-1)

where, $\vec{J}$ represents magnetization, $\vec{m}$ is the individual magnetic dipole moment, ΔV represents summation volume of dipole moments.

Macro to see, the magnetization is called total magnetization ($\vec{J}_{tot}$) is composed of induced magnetization ($\vec{J}_i$) and remanent magnetization ($\vec{J}_r$). Figure 1.3 shows the relationship of magnetizations which is expressed that:
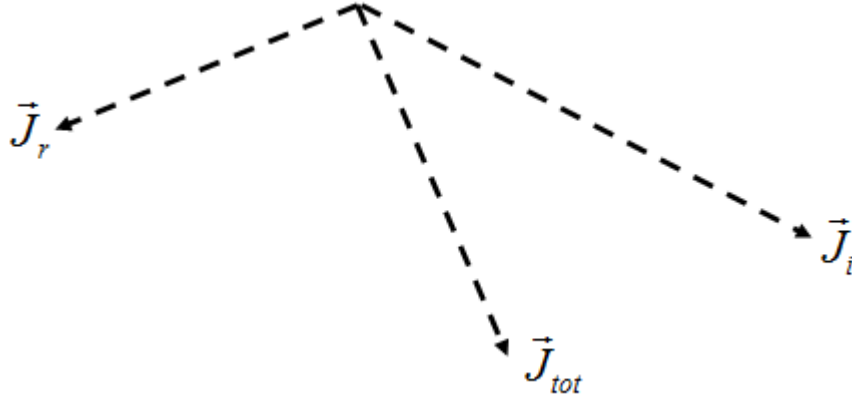
Figure 1.4: Relationship between types of magnetizations. Total magnetization is vector sum of induced magnetization and remanent magnetization.

$$\vec{J}_{tot} = \vec{J}_i + \vec{J}_r$$

(1.2.2-2)

The unit of magnetization is ampere/meter (A/m) in SI system and gauss (G) in cgs system ($1G = 10^3 A/m$).

1.1.3 Induced magnetization

The induced magnetization is the material magnetic polarization in reaction to an external magnetic field. In the subsurface, magnetic domains in magnetically susceptible mineral and rocks act as a collection of small magnets, with each domain having a dipole moment. In the absence of an external magnetic field, the individual dipole will be randomly orientated. With this arbitrary orientation, the net magnetization is zero (Shearer, 2005).
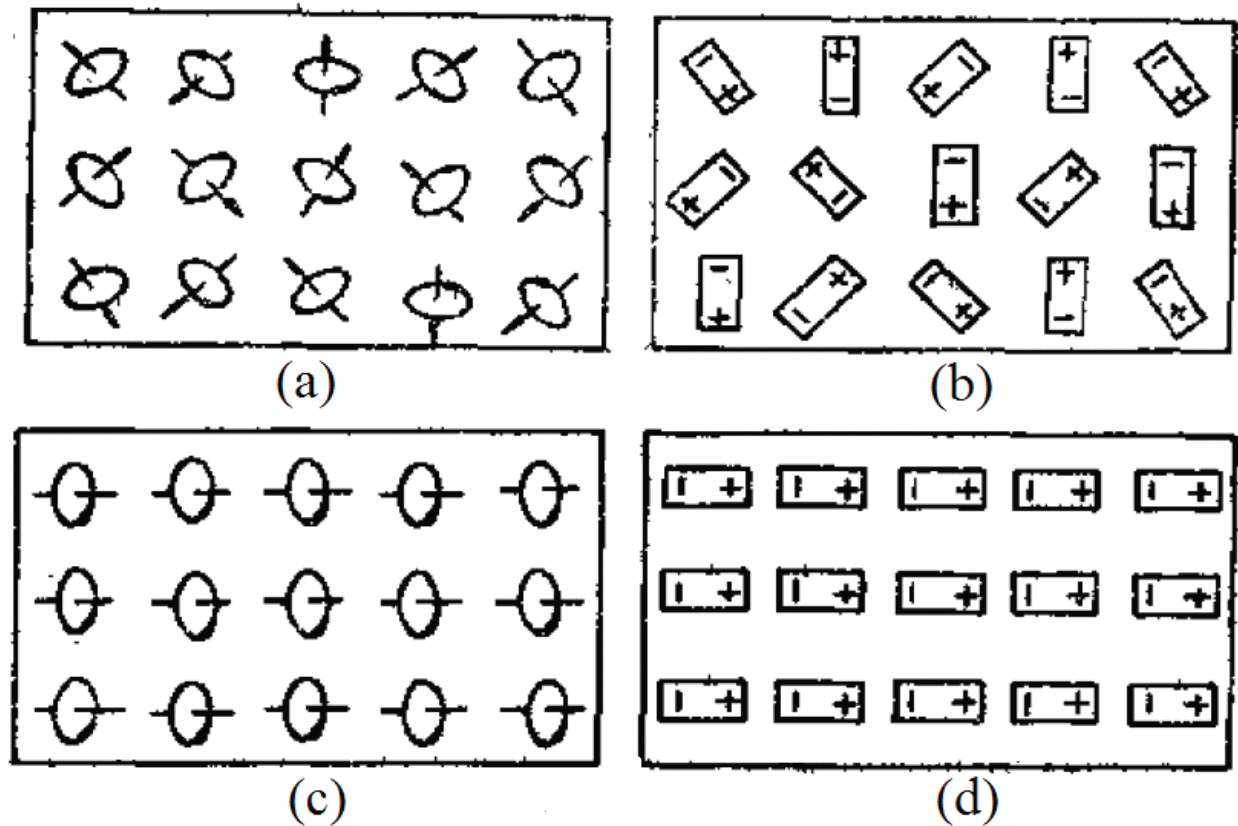
Figure 1.5 Arrangements of atoms or dipole moments within or without the magnetic field: (a) is the arrangement of atoms of magnetizable material without the magnetic field; (b) is the arrangement of dipole moments without the magnetic field; (c) is the arrangement of atoms of magnetizable material within the magnetic field; (d) is the arrangement of dipole moments within the magnetic field.

Magnetic susceptibility is the physical property describing the ability of materials to be magnetized into an inducing external field. "The physics of induced internal magnetization in small fields such as the Earth's is mathematically expressed by a linear relationship" (Macnae 1995). The expression of relationship is written as followed:

$$J_i = \kappa T_0$$

(1.2.3-1)

where, J_i is the induced magnetization, κ is the magnetic susceptibility and T_0 is the external inducting magnetic field.

In general, the mineral magnetism is defined by susceptibility. Consequently, basic and ultrabasic rocks have the highest susceptibility, acid igneous and metamorphic rocks have intermediate to low values, and sedimentary rocks have very small susceptibilities in general (Chen, 2009). Sharma (1997) shows the list of magnetic susceptibility values for common mineral and rock types in Table 1.1.

Table 1.1: List of magnetic susceptibility values for common minerals and rocks.

Mineral or rock type	Magnetic Susceptibility $\left(\kappa \times 10^{-6} SI\right)$
Granite (with magnetite)	20 - 40,000
Slates	0 - 1,200
Basalt	500 - 80,000
Oceanic basalts	300 - 36,000
Limestone (with magnetite)	10 - 25,000
Gneiss	0 - 3,000
Sandstone	35 - 950
Hematite (ore)	420 - 10,000
Magnetite (ore)	7×10^4 - 14×10^6
Magnetite (crystal)	150×10^6

Whole rock susceptibilities can considerably vary owing to a number of factors in addition to mineralogical composition. Susceptibilities depend upon the alignment and shape of the magnetic grains dispersed throughout the rock (Reynolds, 1997).

1.1.4 Remanent magnetization

Certain materials not only have atomic moments, but neighboring moments interact strongly with each other. Such materials are said to be ferromagnetic. The ferromagnetic materials have an ability to retain the magnetization in the absence of external magnetic field. This permanent magnetization is called remanent magnetization (Blakely, 1996).

The remanent magnetization is a function of quantity, atomic, crystallographic, chemical makeup, and grain size of the magnetic minerals. Small magnetic grains support strong, stable remanent magnetizations. It is also affected by the geologic, tectonic, and thermal history of the mineral or rock (Blakely, 1996). The various processed by which rocks can acquire a remanent magnetization are detailed in the table 1.2 (Shearer, 2005).

Table 1.2: Types of remanent magnetization (Shearer, 2005).

Remanent Magnetization	Acronym	Rock Types	Description
Natural	NRM	ALL	Summation of all remanent magnetization components (primary and secondary).
Thermal	TRM	Igneous, Metamorphic	Primary remanent magnetization acquired during cooling from a temperature above the Curie temperature in the presence of an external magnetic field.
Viscous	VRM	All	Secondary remanent magnetization acquired over time, related to thermal agitation and causes decay of primary remanent magnetization.
Depositional	DRM	Sedimentary	Primary remanent magnetization acquired during deposition in the presence of an external field by the physical rotation of magnetic mineral particles. Usually occurs as grains settle out of water.
Post-depositional	PDRM	Sedimentary	Acquired during post-depositional retention of interstitial grains.
Chemical	CRM	All	Remanent magnetization acquired during growth of magnetic minerals in presence of an external field. Includes growth by nucleation or replacement.
Isothermal	IRM	All	Secondary remanent magnetization acquired over a short time at one temperature in a strong, external field.

Natural remanence (NRM) is the main property to control the kimberlite magnetic responses. It is the phenomenon most studies by paleomagnetists (Figure 1.5) whose interest lies in ancient magnetic fields, specifically their intensity and direction (Macnae, 1995). TRM and CRM are two important causes of NRM.
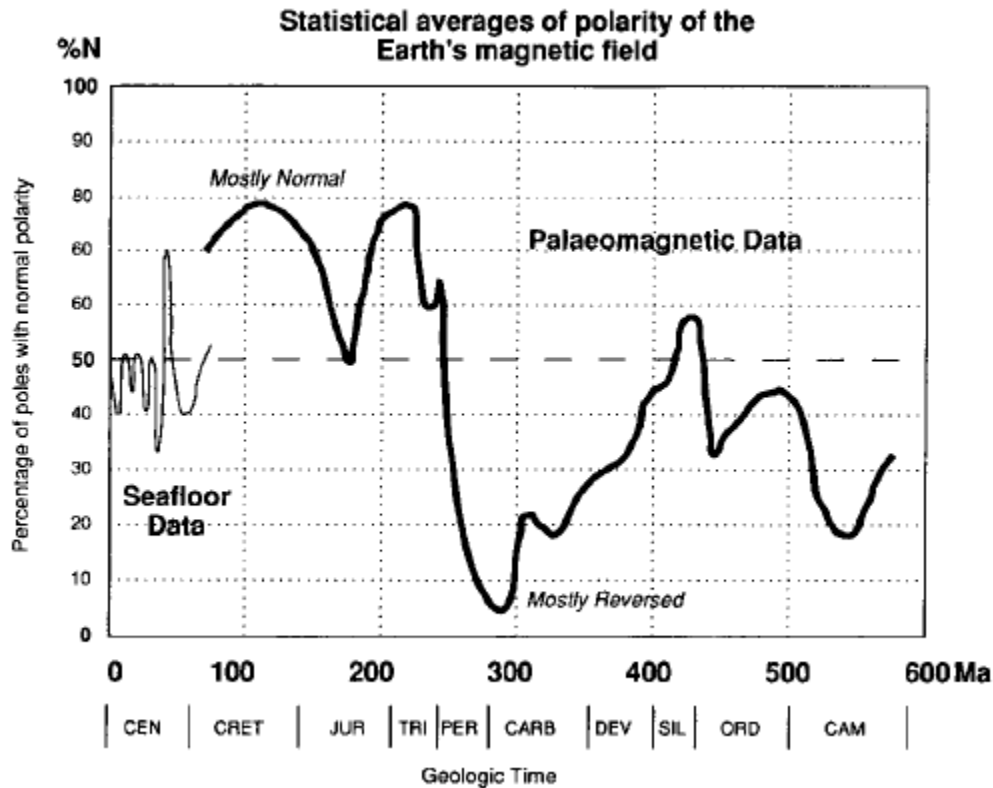
Figure 1.6: Polarity of the Earth's magnetic field as a function of geological time. The paleomagnetic record is less detailed than the sea-floor data. Through the Cambrian to the Permian the field was mostly reversed, Triassic through Cretaceous mostly normal, and about half and half in the recent Cenozoic. (Macnae, 1995)

Commonly the amplitude of hard remanence measured by rock magnetists is larger than the amplitude of induced magnetism, and the Koningsberger ratio (Q) has been defined as the ration of remanent to induced response (Macnae, 1995). Usually the kimberlite breccias are characterized by a low (ranging from 0.2 - 0.8, rarely 2 - 3), however for the hypabyssal kimberlite type, the indicator displays remanence magnitudes of 4 to 6 (Dortman, 1984).

Viscous remanent magnetization (VRM) is an extremely important property to control the kimberlite magnetic responses. VRM is the continuing development of an internal remanent magnetic field parallel to the external field. The intensity of VRM if often a significant fraction of the NRM and induced magnetization, and may exceed either or both in amplitude. VRM intensities are quoted for continental samples; they vary from a few percent of the total NRM up to amplitudes equal to or greater than hard remanent magnetization. VRM will tend to increase

the fraction of the total internal magnetization that will be approximately parallel to the Earth's present field, and may explain why detected anomalies are of normal polarity even when quoted Q values such as those by Clark (1983) indicate that remanence should dominate (Macnae, 1995).

1.2 Magnetic interpretation

Magnetic interpretation is an automatic numerical procedure that constructs a model of subsurface geology from measured magnetic data and other information, with the additional condition that input data are reproduced within a given error tolerance (Nabighian and al., 2005). In order to solve different problems, three interpretation methods were successfully developed: depth estimation, parametric inversion and physical property inversion. Shearer (2005) reviewed a variety of numerical interpretation approaches.

1.2.1 Depth estimation

Depth estimation techniques are initial and useful method to obtain a semi-quantitative representation of the source location. This type of technique initially presumes a regular geometric body shape (contacts, dikes, plates, cylinders and so on) in order to solve nonlinear inversion problems. The estimation parameters is vastly reduced that the problem is an over-determined Shearer (2005).

Naudy (1971) introduced a method to calculate profile over a vertical dike or thin plate by a matched filter, which is applied to observed and reduced-to-the-pole components. O'Brien (1972) introduced CompuDepth method, a frequency-domain technique that determines location and depth to 2D magnetic sources.

Hartman (1971) and Jain (1976) introduced Werner deconvolution method, that utilize total field as well as vertical and horizontal derivative information to estimate the depth, dip, horizontal position and susceptibility contrast of an assumed dike or interface source body. Phillips (1979) introduced ADEPT method, which estimates source parameters from an autocorrelation of an evenly sampled magnetic anomaly profile with dike or contact models.

Thompson (1982) introduced Euler Deconvolution method that solves Euler equation to find depth estimations based on a structural index and increasing window sizes. This method uses first order for each derivatives to determine location and depth for various simple targets, such as

sphere and cylinder, each characterized by specific structural index. Reid (1990) extended this method to 3D domain, offering a technique for analyzing mapped magnetic data. Nabighian and Hansen (2001) introduce an extended Euler deconvolution based on 3D Hilbert transform.

1.2.2 Parametric inversion

Parametric inversion is a quantitative inversion technique for recovering the simple geometry of causative bodies that forward modeling. This method requires certain a prior information, such as a known magnetization direction. This type of nonlinear inversion solves an over-determined problem and recovers parameters for simple bodies, such as prisms and dikes (shearer, 2005).

Bhattacharyya (1980) introduced a 3D iterative method to characterize the magnetized region that fits the measured anomalous response of the subsurface. The horizontal dimensions of the rectangular blocks that comprise the model region are based on the height of observation surface, and the vertical extents of the blocks are adjusted to find a least squares fit between the observed and calculated field values. This method uses the RM to constrain the magnetization direction of each block.

Zeyen and Pous (1991) introduced 3D inversion method to recover parameters for the top and base of vertical rectangular prisms, susceptibility and RM. This method is strongly dependent on the initial model which is modeling by a mount of a prior information, that will restrict the solution to a subset of possible models and does not let the inversion recover a set of parameters that fall outside this model space. Therefor, this method is limited to areas where details about causative body geometry, parameter and property values are well known.

Wang and Hansen (1990) extended the CompuDepth method (O'Brien, 1972) to figure out the corners of 3D homogeneous polyhedral bodies. The depth and location of polyhedral vertices are described by a series of calculated coefficients. The method has the limitation in constructing causative bodies from discrete vertices, even though Wang and Hansen (1990) used other parametric inversion to improve the problem.

1.2.3 Physical property inversion

Physical property inversion is an inversion technique for recovering the subsurface distribution of a physical property, such as magnetic susceptibility (Li and Oldenburg, 1996). This type of linear or nonlinear inversion solves an under-determined problem and recovers parameters for the distribution of physical property.

Li and Oldenburg (1996) introduced a generalized magnetic inversion for distributions of susceptibility, which is useful in areas of multiple anomalies on a variety of scales. The method solves an underdetermined problem by minimizing a global objective function comprised of a model objective function and data misfit. The non-uniqueness of the solution, which is caused by underdetermined problem, is reduced by prior information and constraints (positivity, depth weighting, geologic reasonability).

Pilkington (1997) introduced a 3D inversion method that uses a preconditioned conjugate gradient method for computational efficiency to estimation the distribution of magnetic susceptibility.

Shearer and Li (2004) developed a 3D inversion method to recover the subsurface distribution of magnetic susceptibility. The method inverted amplitude of the anomalous magnetic field and total gradient data directly to recover the magnitude of magnetization without precise knowledge of its direction.

1.3 Magnetic interpretation with strong remanent magnetization

The RM has hampered the magnetic interpretation for a long time, but has not received much attention for two reasons. First, the TM direction is similar to the orientation of the inducing field in the majority of exploration problems. The reason is that the direction of the RM is approximately collinear (aligned or antiparallel) with the current inducing field or the amplitude of the RM is weak. Second, the earlier interpretation techniques are weakly dependent on the TM direction, such as depth estimation techniques. However, RM is often strong and cannot be disregarded in numerous cases, such as archaeology, some mineral exploration, basement imaging in petroleum exploration, and crustal and planetary studies (Shearer, 2005).

Most of methods interpret the magnetic data in the presence of strong RM through direction estimation and exploitation of mathematical relationships, often utilizing quantities that have no or minimal dependence on magnetization direction.

Roest and Pilkington (1993) utilized the total gradient and pseudo gravity to estimate the TM direction and determine the location of source bodies using the properties of the magnetic anomaly. Haney and Li (2002) extracted the TM direction and dip from total field measurements using continuous wavelet transforms. Shearer and Li (2004) developed a 3D physical property inversion algorithm that utilized the minimal dependence on magnetization direction by quantities such as total gradient in presence of RM with Tikhonov regularization method to recover the subsurface distribution of magnetic susceptibility. Chemam (2006) and Chen (2009) utilized amplitude of magnetic anomaly and its analytic signal to do the parametric inversion using the model of vertical cylinder in presence of RM with Gauss-Newton method to recover the magnetic and geometrical properties of kimberlite pipe.

1.4 Magnetic technique for detecting the kimberlite

Burley and Greenwood (1972) found magnetic anomalies over all known kimberlites in Lesotho. Macnae (1979) gave an example of an aeromagnetic survey that was flown by Geoterrex Ltd., of Ottawa, Canada. Nixon (1981) mentions that magnetic anomalies may occur within individual pipes, as in Letseng-la-Terae, Lesotho, indicating separate diamondiferous intrusions. Atkinson (1989) states that the variable and complex nature of magnetic responses found over kimberlites is more likely to reflect the nature of the body itself than the differential weathering of the pipe. Sarma (1999) used the ground magnetic vertical intensity contour map to map the Majhgawan kimberlite pipe near Panna in central India successfully.

Airborne magnetics and grounds magnetics are common techniques using in magnetic survey for kimberlite. The most cost-effective geophysical reconnaissance technique has been airborne magnetics (Macnae, 1995). Keating and Sailhac (2004) indicated that most kimberlites have a distinctive aeromagnetic signature that is a roughly circular anomaly in general, but the anomaly at ground level is more complex and it can have internal highs or be elongated. Therefore, most of pipes were first detected by means of an airborne reconnaissance survey.

The magnetic interpretation of kimberlite is to determine the nature remanent component, the viscous and induced components and geometry properties of anomaly. Paterson (1991) introduced the 3D Euler deconvolution to automatically locate circular anomalies, but this technique tends to generate a large number of "false targets". Keating (1995) introduced matched filter that is based on first-order regression analysis between a window of the gridded data and a typical target theoretical anomaly, but the filter dose not deal with low magnetic latitudes and strong magnetic remanence very well. Keating (2004) improved this method that changed window between the analytic signal of the observed magnetic field and the theoretical analytic signal of a magnetic vertical cylinder. Paulo (2007) introduced a technique based on joint analysis of analytic signal and Euler deconvolution. Cheman (2006) worked about the parametric and physical property inversion of magnetic field and analytic signal data due to the vertical right cylinder with arbitrary polarization in presence of remanence using the model of kimberlite pipe. He presented the RM to the inversion, and did the initial works for the separation the RM from the TM for the anomalies from the kimberlites. Chen (2009) continued and improved parametric and physical property inversion of magnetic field and analytic signal data due to the vertical right cylinder with arbitrary polarization in the presence of the remanence using the model of cylinder.

As discussed above, the results of magnetic interpretations always get the false targets. In order to reduce the "false targets", the other information must to be operated into the interpretation, such as geological (structural and tectonic), geochemical and other geophysical data (gravity, EM, resistivity, spectrometry).

CHAPTER 2   ANALYTIC SIGNAL METHODOLOGY

The purpose of this chapter is to introduce the basic principle of analytic signal and derive for its calculation. First, I introduce the theory of analytic signal and the expression of absolute value of the analytic signal. Then, I review the expression of total magnetic field anomaly due to a vertical right circular cylinder. I then introduce the computational of analytic signal by Fourier transform. Lastly, I illustrate the algorithm with synthetic examples.

2.1   Introduction

The analytic signal is computed from the gradients along the three axes of magnetic data. It is weakly dependent of the total magnetization direction. Nabighian (1972) computed the amplitude of the two-dimensional gradient vector from a given magnetic profile. The vertical derivative of magnetic field can be calculated from the horizontal derivative by Hilbert transforms. In 1984, Nabighian further developed the relationship between horizontal and vertical derivatives by Hilbert transforms that expanded method to three dimensions. Paine et al. (2001) examine the total gradient of the vertically integrated magnetic anomaly and vertical integration of the total gradient due to weak dependence on magnetization direction and both quantities processing the dimensions of the magnetic field.

The three-dimensional $\vec{g}$ of a potential-field anomaly can be defined as follow:

$$\vec{g} = \left(\frac{\partial f}{\partial x} \vec{i} + \frac{\partial f}{\partial y} \vec{j} + \frac{\partial f}{\partial z} \vec{k} \right),$$

(2.1-1)

where f is responses of magnetic field, and $\vec{i}$, $\vec{j}$, $\vec{k}$ are unit vectors in the x, y, z directions respectively.

The absolute value of the analytic signal is defined as the square root of the sum of squared vertical and two horizontal derivatives of the total magnetic field anomaly. The expression of the analytic signal is written as follows:

$$g = |\vec{g}| = \sqrt{\left(\frac{\partial f}{\partial x} \right)^2 + \left(\frac{\partial f}{\partial y} \right)^2 + \left(\frac{\partial f}{\partial z} \right)^2}$$

(2.1-2)

2.2 Modeling the magnetic field

In order to model the analytic signal field anomalous due to a vertical right circular cylinder, the total magnetic field anomalous must be used. In this section, I introduce the solution for the total magnetic field anomalous due to a vertical right circular cylinder.

Singh and Sabina (1978) presented the analytical solution for the total anomalous magnetic field due to a vertical right circular cylinder with arbitrary polarization under the assumption that the magnetization is uniform.

The geometry is shown in Figure 2.1.
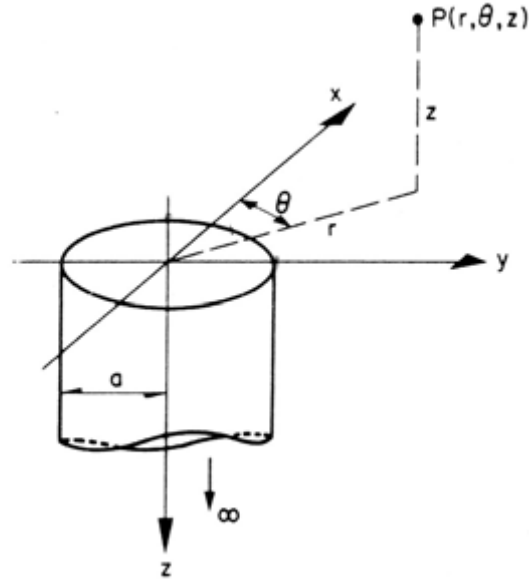
Figure 2.1: Geometry of semi-infinite vertical cylinder

The expression of the total field anomaly due to the right circular cylinder is written as follows:

$$F = 2\pi a \cdot J_{tot}[(C-A)\cdot I(1,0;0)-(E-A)\cdot\frac{1}{r}I(1,1;-1)-BI(1,1;0)],$$

(2.2-1)

$$C = nN,$$

$$A = lL\cdot\cos^2\theta + (lM+mL)\sin\theta\cos\theta + mM\sin^2\theta,$$

$$E = lL\sin^2\theta - (lM+mL)\sin\theta\cos\theta + mM\cos^2\theta,$$

$$B = (lN + nL)\cos\theta + (mN + nM)\sin\theta,$$

$$l = \cos I_o \cdot \cos D_0, \qquad L = \cos I_m \cdot \cos D_m,$$

$$m = \cos I_o \cdot \sin D_0, \qquad M = \cos I_m \cdot \sin D_m,$$

$$n = \sin I_o, \qquad\qquad N = \sin I_m,$$

$$I(1,0;0) = \begin{cases} -\dfrac{k|z|}{4a\sqrt{ar}}F_0(k) - \dfrac{1}{2a}\Lambda_0(\beta,k) + \dfrac{1}{a}, & (a>r) \\[3mm] -\dfrac{k|z|}{4a^2}F_0(k) + \dfrac{1}{2a}, & (a=r) \\[3mm] -\dfrac{k|z|}{4a\sqrt{ar}}F_0(k) + \dfrac{1}{2a}\Lambda_0(\beta,k), & (a<r) \end{cases}$$

$$I(1,1;-1) = \begin{cases} \dfrac{|z|E_0(k)}{2k\sqrt{ar}} - \dfrac{k|z|}{4ar\sqrt{ar}}\left(a^2 + r^2 + \dfrac{z^2}{2}\right)F_0(k) + \dfrac{a^2 - r^2}{4ar}\Lambda_0(\beta,k) + \dfrac{r}{2a}, & (a>r) \\[3mm] \dfrac{|z|E_0(k)}{2ka} - \dfrac{k|z|}{4a^3}\left(2a^2 + \dfrac{z^2}{2}\right)F_0(k) + \dfrac{1}{2}, & (a=r) \\[3mm] \dfrac{|z|E_0(k)}{4k\sqrt{ar}} - \dfrac{k|z|}{4ar\sqrt{ar}}\left(a^2 + r^2 + \dfrac{z^2}{2}\right)F_0(k) + \dfrac{r^2 - a^2}{4ar}\Lambda_0(\beta,k) + \dfrac{a}{2r}, & (a<r) \end{cases}$$

$$I(1,1;0) = \frac{1}{k\sqrt{ar}}\left[\left(1 - \frac{k^2}{2}\right)F_0(k) - E_0(k)\right],$$

$$k^2 = \frac{4ar}{(a^2 + r^2) + z^2}.$$

$$\sin^2\beta = \frac{z^2}{(a^2 - r^2) + z^2}.$$

$$F_0(k) = \frac{2}{\pi}K(k) \quad and \quad E_0(k) = \frac{2}{\pi}E(k).$$

(I_0, D_0) represent inclination and declination of the Earth magnetic field, (I_m, D_m) are the inclination and declination of the total magnetic field intensity. $K(k)$ and $E(k)$ are two complete elliptic integrals :

$$K(k) = K\left(\frac{\pi}{2}, k\right) = \int_0^{\frac{\pi}{2}} \frac{d\varphi}{\sqrt{1 - k^2 \sin^2 \varphi}},$$

$$E(k) = E\left(\frac{\pi}{2}, k\right) = \int_0^{\frac{\pi}{2}} \sqrt{1 - k^2 \sin^2 \varphi} \cdot d\varphi.$$

$\Lambda_0(\beta, k)$ is the Lambda function :

$$\Lambda_0(\beta, k) = \frac{2}{\pi} \left[K(k) \cdot E\left(\beta, \sqrt{1 - k^2}\right) + \left(E(k) - K(k)\right) \cdot K\left(\beta, \sqrt{1 - k^2}\right) \right].$$

where $K\left(\beta, \sqrt{1-k^2}\right)$ and $E\left(\beta, \sqrt{1-k^2}\right)$ represent the complete elliptic integrals of first and second order respectively.

2.3 Calculating the analytic signal field by Fourier transform

The faster and easier method to compute the analytic signal from the total magnetic field anomaly is through two-dimensional Fourier transforms. The vertical derivative of the magnetic field can be calculated from the horizontal derivative, allowing for a fast and accurate method of computing the vertical derivative from a given datum of magnetic survey. In this section, I introduce Fourier transform to calculate the analytic signal.

2.3.1 Fourier transform derivation

The two-dimension Fourier transform is a mathematical operation that expresses spatial domain as the wavenumber domain. The following convention is used for the two-dimension Fourier transform and inverse.

$$F(k_x, k_y) = \int_{-\infty}^{\infty} \int_{-\infty}^{\infty} f(x, y) \cdot e^{-i(k_x \cdot x + k_y \cdot y)} dxdy$$

(2.3.1-1)

$$f(x, y) = \frac{1}{4\pi^2} \int_{-\infty}^{\infty} \int_{-\infty}^{\infty} F(k_x, k_y) \cdot e^{i(k_x \cdot x + k_y \cdot y)} dk_x dk_y$$

(2.3.1-2)

where, $f(x,y)$ is the function in spatial domain, $F\left(k_x, k_y\right)$ is the function in wavenumber domain. x and y are the horizontal directions, k_x and k_y are the wavenumber in x and y directions.

According to the differentiation property of Fourier transform, the horizontal and vertical derivatives are obtained. The expressions are written as follow:

$$\frac{\partial f}{\partial x} = \frac{1}{4\pi^2} \int_{-\infty}^{\infty} \int_{-\infty}^{\infty} \left(-ik_x\right) \cdot F\left(k_x, k_y\right) \cdot e^{i\left(k_x \cdot x + k_y \cdot y\right)} dk_x dk_y$$

(2.3.1-3)

$$\frac{\partial f}{\partial y} = \frac{1}{4\pi^2} \int_{-\infty}^{\infty} \int_{-\infty}^{\infty} \left(-ik_y\right) \cdot F\left(k_x, k_y\right) \cdot e^{i\left(k_x \cdot x + k_y \cdot y\right)} dk_x dk_y$$

(2.3.1-4)

and

$$\frac{\partial f}{\partial z} = \frac{1}{4\pi^2} \int_{-\infty}^{\infty} \int_{-\infty}^{\infty} \left(-ik_z\right) \cdot F\left(k_x, k_y\right) \cdot e^{i\left(k_x \cdot x + k_y \cdot y\right)} dk_x dk_y$$

(2.3.1-5)

where, z is the vertical direction and k_z is wavenumber in z direction which are unknown.

I consider that the spatial domain is source free. The spatial domain can be expressed by Laplace equation:

$$\Delta f = 0$$

(2.3.1-6)

where, Δ is Laplace operator.

The equation (2.3.1-6) also can be expressed that:

$$\frac{\partial^2 f}{\partial x^2} + \frac{\partial^2 f}{\partial y^2} + \frac{\partial^2 f}{\partial z^2} = 0$$

(2.3.1-7)

Substitution (2.3.1-3), (2.3.1-4) and (2.3.1-5) into (2.3.1-7), the equation is written as follow that:

$$\frac{1}{4\pi^2} \int_{-\infty}^{\infty} \int_{-\infty}^{\infty} \left[\left(-ik_x\right)^2 + \left(-ik_y\right)^2 + \left(-ik_z\right)^2\right]\left(-ik_x\right) \cdot F\left(k_x, k_y\right) \cdot e^{i\left(k_x \cdot x + k_y \cdot y\right)} dk_x dk_y = 0$$

(2.3.1-8)

$$\left(-ik_x\right)^2 + \left(-ik_y\right)^2 + \left(-ik_z\right)^2 = 0$$

(2.3.1-9)

Hence,

$$-ik_z = \sqrt{k_x^2 + k_y^2}$$

(2.3.1-10)

Substitution (2.3.1-9) into (2.3.1-5), the vertical derivative is rewritten as followed:

$$\frac{\partial f}{\partial z} = \frac{1}{4\pi^2} \int_{-\infty}^{\infty} \int_{-\infty}^{\infty} \sqrt{k_x^2 + k_y^2} \cdot F(k_x, k_y) \cdot e^{i(k_x \cdot x + k_y \cdot y)} dk_x dk_y$$

(2.3.1-11)

2.3.2 Fourier transform derivation computational

In practice, DFT (discrete Fourier transform) is used to compute the horizontal and vertical derivatives. Meanwhile the forward and inverse DFT (discrete Fourier transform) is computed by FFT (fast Fourier transform).

The forward and inverse 2D DFT are defined as followed:

$$F[k_m, k_n] = \sum_{m=0}^{M} \sum_{n=0}^{N} e^{-i\left(\frac{2\pi}{M}mk_m + \frac{2\pi}{N}nk_n\right)} f[m, n]$$

(2.3.2-1)

$$f[m, n] = \frac{1}{MN} \sum_{k_m=0}^{M} \sum_{k_n=0}^{N} e^{i\left(\frac{2\pi}{M}mk_m + \frac{2\pi}{N}nk_n\right)} F[k_m, k_n]$$

(2.3.2-2)

where, $f[m, n]$ is the discrete function in spatial domain, $F[k_m, k_n]$ is the discrete function in wavenumber domain. M and N are the sample number of datum in the horizontal x and y directions, $(m = 0,1,\cdots, M-1)$ and $(n = 0,1,\cdots, N-1)$ are the sample index of datum in the horizontal x and y directions, $(k_m = 0,1,\cdots, M-1)$ and $(k_n = 0,1,\cdots, N-1)$ are the sample index of wavenumber in the horizontal x and y directions.

Having being analyzed the equation of forward and inverse two-dimension discrete Fourier transform, the relationship of value and sample index is obtained as followed:

$$x = m \cdot \Delta x$$

(2.3.2-3)

$$y = n \cdot \Delta y$$

(2.3.2-4)

$$k_x = \frac{2\pi}{M \cdot \Delta x} \cdot k_m$$

(2.3.2-5)

$$k_y = \frac{2\pi}{N \cdot \Delta y} \cdot k_n$$

<div align="right">(2.3.2-6)</div>

where, Δx and Δy are the sample interval in the horizontal x and y directions.

The (2.3.1-3), (2.3.1-4) and (2.3.1-11) can be discretized as followed:

$$\frac{\partial f}{\partial x} = \frac{1}{MN} \sum_{k_m=0}^{k_M} \sum_{k_n=0}^{k_N} \left(-i \frac{2\pi}{M \cdot \Delta x} \cdot k_m \right) \cdot e^{i\left(\frac{2\pi}{M} mk_m + \frac{2\pi}{N} nk_n \right)} F[k_m, k_n]$$

<div align="right">(2.3.2-7)</div>

$$\frac{\partial f}{\partial y} = \frac{1}{MN} \sum_{k_m=0}^{k_M} \sum_{k_n=0}^{k_N} \left(-i \frac{2\pi}{N \cdot \Delta y} \cdot k_n \right) \cdot e^{i\left(\frac{2\pi}{M} mk_m + \frac{2\pi}{N} nk_n \right)} F[k_m, k_n]$$

<div align="right">(2.3.2-8)</div>

$$\frac{\partial f}{\partial z} = \frac{1}{MN} \sum_{k_m=0}^{k_M} \sum_{k_n=0}^{k_N} \sqrt{\left(\frac{2\pi}{M \cdot \Delta x} \cdot k_m \right)^2 + \left(\frac{2\pi}{N \cdot \Delta y} \cdot k_n \right)^2} \cdot e^{i\left(\frac{2\pi}{M} mk_m + \frac{2\pi}{N} nk_n \right)} F[k_m, k_n]$$

<div align="right">(2.3.2-9)</div>

where, the $k_M = (M-1)/2$ and $k_N = (N-1)/2$, are the indices up to the Nyquist frequency.

Hence, substituting the (2.3.2-7), (2.3.2-8) and (2.3.2-9) into (2.1-2), the analytic signal can be solved.

2.4 Calculating the analytic signal field by finite difference method

The finite difference method is a conventional method to calculate the vertical and the two horizontal derivatives. Keating and Saihac (2004) calculated the horizontal derivatives by finite difference method. The expression (2.5-1) is the solution of finite difference to obtain the analytic signal.

$$g = \sqrt{\left(\frac{f(x+\delta x/2) - f(x-\delta x/2)}{\delta x} \right)^2 + \left(\frac{f(y+\delta y/2) - f(y-\delta y/2)}{\delta y} \right)^2 + \left(\frac{f(z+\delta z/2) - f(z-\delta z/2)}{\delta z} \right)^2}$$

<div align="right">(2.4-1)</div>

where f is responses of magnetic field which was calculated by Singh and Sabina (1978), g is the analytic signal. x and y are the horizontal directions, z is the vertical direction respectively. δx, δy and δz are the spacing in x, y and z respectively.

The finite difference method is a conventional method to compute the derivative. Here, it is used to prove the Fourier transform method is feasibility and accuracy.

2.5 Analytic signal technique

I present the program structure diagram (Figure 2.2) to describe the analytic signal computational process.

I note that there are two types of data of total magnetic field anomaly to compute the analytic signal. They are the forward modeled data and observed data. There are two different methods to process these data. For forward modeled data, it is calculated using eq.2.2-1, so the area can be extended directly by computing the data on an area larger that the target. For observation data, it is extended out of the target area using some smoothness technique (maximum entropy). The mapped zone is extended by the 20% of survey area width on each side.

According to the Fourier transform principle, the boundary must be smooth and near zero. I choose the 10% cosine taper filter to smooth the boundary in each side. In the wavenumber domain, I low pass filter the data to reduce noise generated by the filter linearly increasing with frequency related to the derivatives. The filter used is again a 10% cosine taper decreasing to zero at the Nyquist frequency.
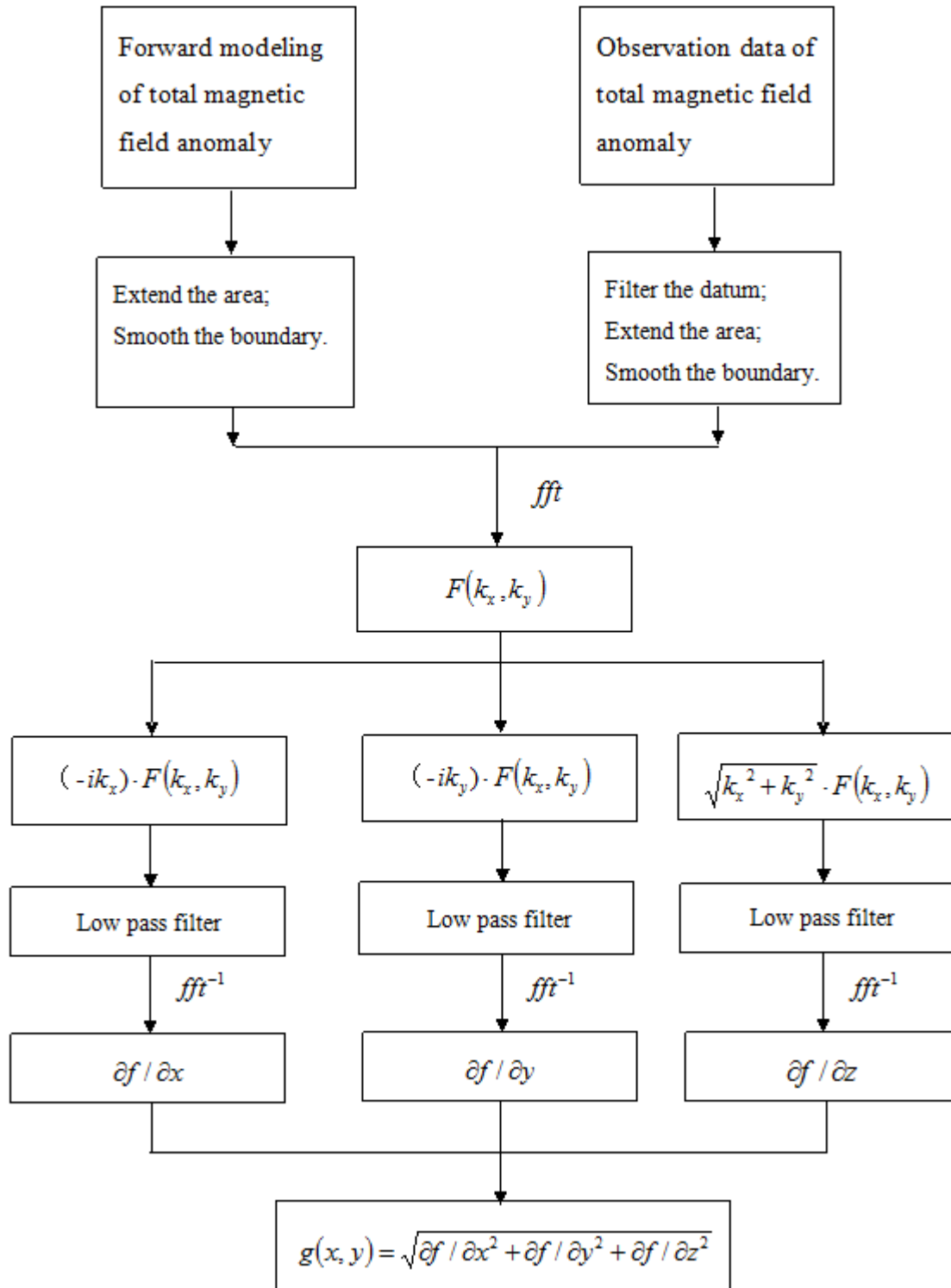
Figure 2.2: Flow chart for the analytic signal computation

2.6 Synthetic example

In this section, I present four semi-infinite vertical cylinder models to simulate the kimberlite pipes. The geomagnetic field is the same for each model with amplitude of 57,000nT, inclination 74˚ and declination -12˚. The survey area for which the modeled responses are computed is 1,000m by 1,000m and is sampled by 101 x 101 sites (10201 receivers); the data spacing is 10m.

The first model is a semi-infinite vertical cylinder with a diameter of 248m, centered in the survey area and located at a depth of 69m. The amplitude of TM is $J_{tot} = 768nT$, the direction of TM is $I_{tot} = 69^o$ and $D_{tot} = -19^o$. The responses of magnetic total-field anomaly and its analytic signal are shown in Figure 2.3. The computation time using the Fourier transform and the finite difference methods are 0.16s and 9.90s respectively. The calculation was completed using Matlab installed in a CPU core i3 and 4G memory computer with Windows7 system (the computer for the remaining of calculations in the thesis).

Figure 2.3a shows the magnetic total-field anomaly caused by a circular pipe with a magnetization direction near the geomagnetic field. The magnetic field anomaly can be clearly observed but because of asymmetry the size and location of the pipe are difficult to determine. Figure 2.3b and 2.3c show the analytic signal due to the same model. The analytic signal of anomaly is highlight and shows clearly the size and location of the pipe and asymmetry is low compared to the magnetic anomaly.

Geomagnetic field:

$T_0 = 57000 nT$;

$I_{tot} = 74^o$, $D_{tot} = -12^o$.
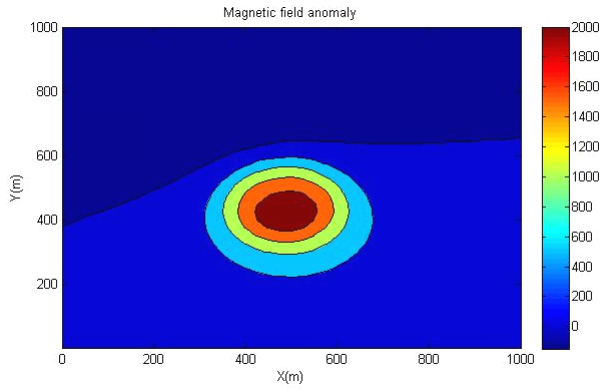
Model parameters:

$J_{tot} = 768 nT$;

$I_{tot} = 69^o$, $D_{tot} = -19^o$;

Diameter=248m; Depth=69m.

C=(500m, 500m).

(a)
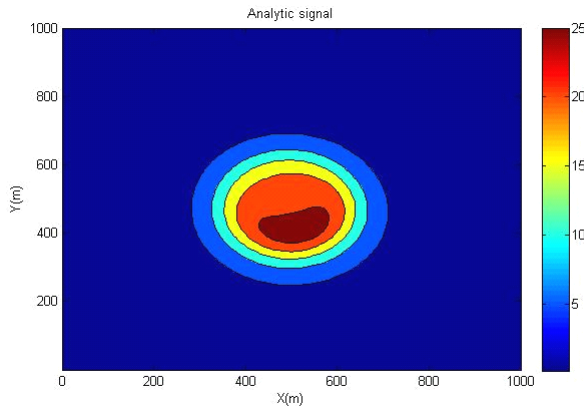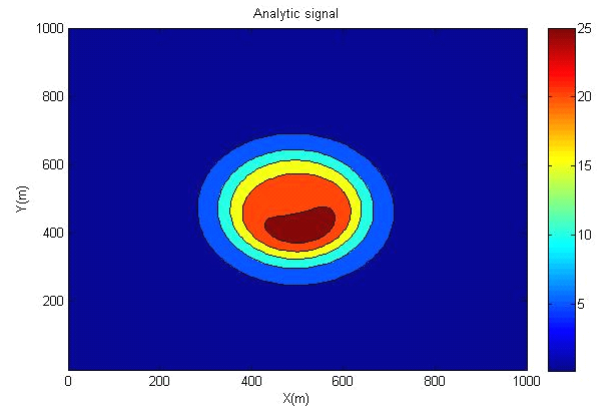
(b)   (c)

Figure 2.3: Model 1: magnetic field anomaly and its analytic signal. X-axes is directed to the east and Y-axes is directed to the north. (a) Total-field magnetic anomaly, (b) analytic signal computed using the Fourier transform method, (c) analytic signal computed using the finite difference method.

The second model is a semi-infinite vertical cylinder with a diameter of 248m, centered in the survey area and located at a depth of 69m. The amplitude of TM is $J_{tot} = 768nT$, the direction of TM is $I_{tot} = -22^{o}$ and $D_{tot} = 47^{o}$. The responses of magnetic total-field anomaly and its analytic signal are shown in Figure 2.4. The computation time using the Fourier transform and the finite difference methods are 0.15s and 9.88s respectively.

Figure 2.4a shows the magnetic total-field anomaly caused by a circular pipe with a magnetization direction far from the geomagnetic field. The magnetic field anomaly does not clearly delineate the size and location of the pipe. Figure 2.4b and 2.4c show the analytic signal due to the same model. The analytic signal anomaly better locates the pipe however some asymmetry prevails that makes difficult estimation of its size.

(a)

Geomagnetic field:

$T_0 = 57000 nT$;

$I_{tot} = 74^o$, $D_{tot} = -12^o$.
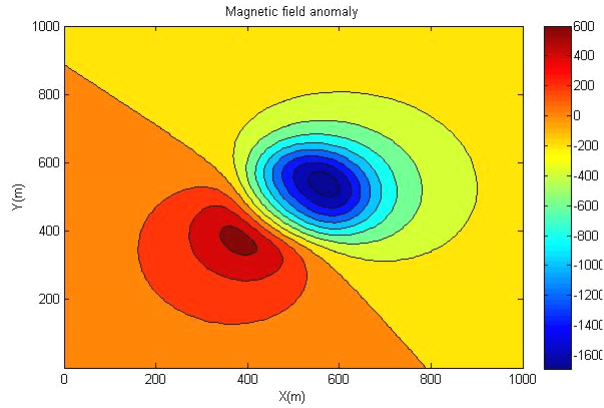
Model parameters:

$J_{tot} = 768 nT$;

$I_{tot} = -22^o$, $D_{tot} = 47^o$;

Diameter=248m; Depth=69m.

C=(500m, 500m).
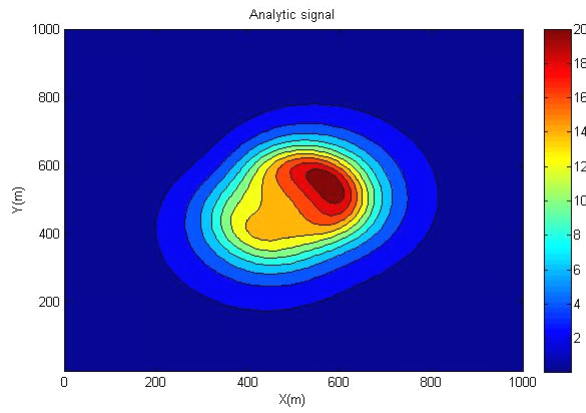
(b)
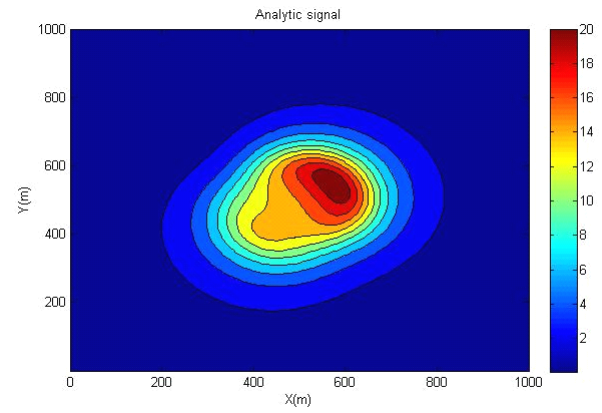
(c)

Figure 2.4: Model 2: magnetic field anomaly and its analytic signal for model. X-axes is directed to the east and Y-axes is directed to the north. (a) Total-field magnetic anomaly, (b) analytic signal computed using the Fourier transform method, (c) analytic signal computed using the finite difference method.

The third model is a semi-infinite vertical cylinder with a diameter of 334m, centered in the survey area and located at a depth of 26m. The amplitude of TM is $J_{tot} = 289nT$, the direction of TM is $I_{tot} = 143^o$ and $D_{tot} = -31^o$. The responses of magnetic total-field anomaly and its analytic signal are shown in Figure 2.5. The computation time using the Fourier transform and the finite difference methods are 0.16s and 11.11s respectively.

Figure 2.5a shows the magnetic total-field anomaly caused by a shallow circular pipe with a magnetization direction near the vertical. The magnetic field anomaly clearly delineates its size and indicates its location. Figure 2.5b and 2.5c show the analytic signal measured over the model. The analytic signal anomaly does show limits of the pipe.

(a)

Geomagnetic field:

$T_0 = 57000 nT$;

$I_{tot} = 74^o$, $D_{tot} = -12^o$.
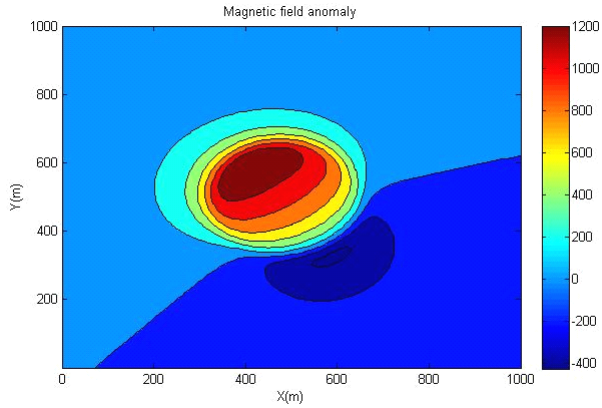
Model parameters:

$J_{tot} = 289 nT$;

$I_{tot} = 143^o$, $D_{tot} = -31^o$;

Diameter=334m; Depth=26m.

C=(500m, 500m).
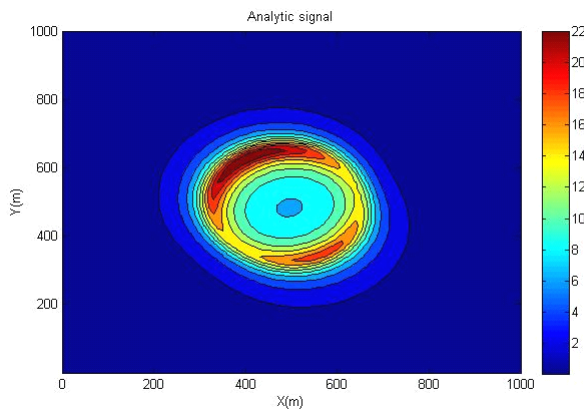
(b)
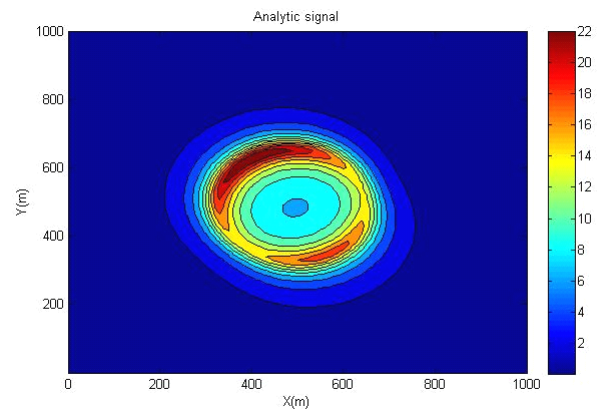
(c)

Figure 2.5: Model 3: magnetic field anomaly and its analytic signal. X-axes is directed to the east and Y-axes is directed to the north. (a) Total-field magnetic anomaly, (b) analytic signal computed using the Fourier transform method, (c) analytic signal computed using the finite difference method.

The fourth model is a semi-infinite vertical cylinder with a diameter of 154m, centered in the survey area and located at a depth of 163m. The amplitude of TM is $J_{tot} = 2488nT$, the direction of TM is $I_{tot} = 83^o$ and $D_{tot} = -8^o$. The responses of magnetic total-field anomaly and its analytic signal are shown in Figure 2.6. The computation time using the Fourier transform and the finite difference methods are 0.19s and 11.35s respectively.

Figure 2.6a shows the magnetic total-field anomaly caused by a deep circular pipe with a direction of magnetization near the vertical. The magnetic field anomaly clearly delineates the size and location of the pipe, and there is little assymetry. Figure 2.6b and 2.6c shows the analytic signal computed for the same model. The analytic signal anomaly is obvious giving a strong indication about the size and location of the pipe with little to none asymmetry.

(a)

Geomagnetic field:

$T_0 = 57000nT$;

$I_{tot} = 74^o$, $D_{tot} = -12^o$.
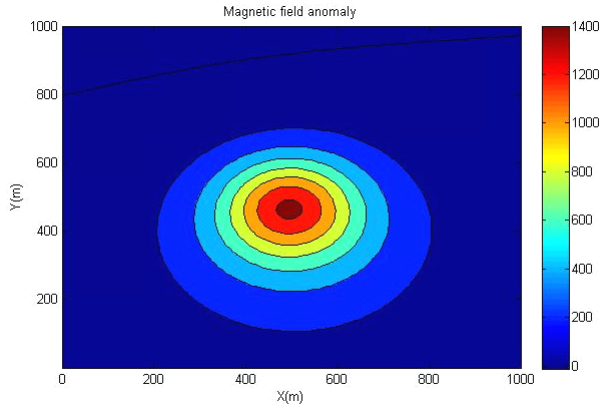
Model parameters:

$J_{tot} = 2488nT$;

$I_{tot} = 83^o$, $D_{tot} = -8^o$;

Diameter=154m; Depth=163m.

C=(500m, 500m).
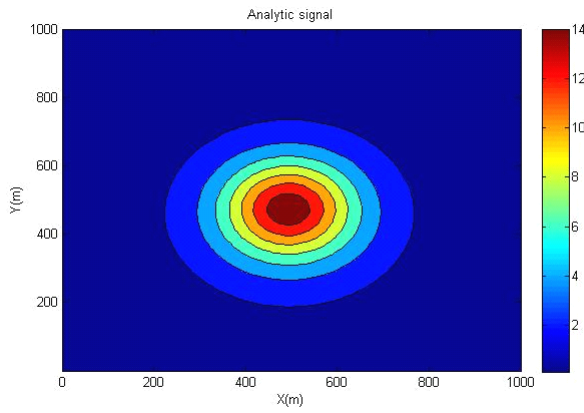
(b)
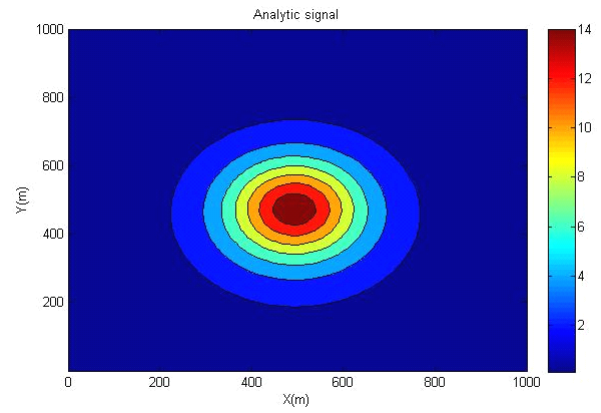
(c)

Figure 2.6: Model 4: magnetic field anomaly and its analytic signal. X-axes is directed to the east and Y-axes is directed to the north. (a) Total-field magnetic anomaly, (b) analytic signal computed using the Fourier transform method, (c) analytic signal computed using the finite difference method.

Comparing figures 2.3 to 2.6, the analytic signal is weakly dependent on the direction of magnetization. The analytic signal anomaly is centered near the pipe location. Figure 2.5 is the shallow pipe that the anomaly responses of analytic signal is near the boundary. Comparing to the (b) and (c) in figure 2.3 to figure 2.6, the Fourier transform method leads to an almost identical response of the analytic signal as the finite difference method. Meanwhile, the Fourier transform method is 50 times faster than finite difference method. The feasibility, accuracy and high efficiency of Fourier transform to calculate the analytic signal is proved.

2.7 Conclusion

Based on the result of figure 2.3 to figure 2.6, the total magnetic field and analytic signal forward modeling is present with different models. Compared to the total magnetic field anomaly, the analytic signal is weakly dependent on magnetization direction. It is diagnostic of the size and location of the pipe and whatever the magnetization direction there is little asymmetry. From these results, the analytic signal is insensitive to depth.

Fourier transform is a general method for estimating the analytic signal and other methods; Hilbert transform can also be used. Both Fourier and Hilbert transform can obtain the vertical derivative from the two horizontal derivatives, because the gradient divergence is zero in absence of sources. The Fourier transform method is used to calculate the analytic signal because of its efficiency and convenience. In general, the total-field magnetic data have to be processed using operators such as high pass filtering, upward continuation, etc., in wavenumber domain using the Fourier transform.

CHAPTER 3   INVERSION METHODOLOGY

The purpose of this chapter is to introduce the theory and computation of joint inversion of magnetic field and analytic signal data. Firstly, I introduce the inversion theory to solve the general problem. Then, I present the specific computation and structure diagram to complete the joint inversion of the total anomalous magnetic field and analytic signal due to a vertical right circular cylinder with arbitrary polarization. Lastly, I illustrate the algorithm with synthetic examples.

3.1 Inversion theory

According to the forward modeling of the magnetic field and analytic signal anomalies, joint inversion of the magnetic field and analytic signal data is a nonlinear ill-posed inversion.

Least-squares method is one of the popular methods for solving ill-posed problem. Lines and Treitel (1984) give a tutorial on least-squares inversion and its application to geophysical problems.

3.1.1 Nonlinear inversion

The basic strategy is to minimize the sum of squares of the errors between the model response and the observations. Let the N observations for a set of both of magnetic field data and analytic signal data be represented by the vector:

$$d^o = col\left(d^o_{\ 1}, d^o_{\ 2}, \cdots, d^o_{\ N}\right).$$

(3.1.1-1)

and the model response by the vector:

$$d^o = col\left(d^o_{\ 1}, d^o_{\ 2}, \cdots, d^o_{\ N}\right).$$

(3.1.1-2)

where, $k = 1, 2, \cdots, M$ is the iteration number.

The model is a function of parameters that are elements of a vector:

$$m = col\left(m_1, m_2, \cdots, m_P\right).$$

(3.1.1-3)

where, P is the number of parameters.

Let m_{j0} be an initial estimate of parameter m_j, and let d^c_0 be the initial model response.

The model response can be represented by the first-order Taylor expansion:

$$d^c_1 = d^c_0 + \sum_{j=1}^{P} \frac{\partial d^c_1}{\partial m_{j0}} \left(m_{j1} - m_{j0} \right)$$

(3.1.1-4)

or, in matrix notation:

$$d^c_k = d^c_{k-1} + A_{ijk} \delta m_k$$

(3.1.1-5)

where A is the $N \times P$ Jacobian matrix of partial derivatives (or sensitivity matrix) with elements:

$$A_{ijk} = \frac{\partial d^c_{ik}}{\partial m_{jk}},$$

and $\delta m_k = m_k - m_{k-1}$ is the parameter change vector.

Our choice of perturbations in m will be made so as to minimize the sum of squares of the errors between the model response and the data. Let ε represent the error vector expressing the difference between the model response d^c_k and the observed data d^o:

$$\varepsilon = d^o - d^c_k$$

(3.1.1-6)

Substituting (3.1.1-5) into (3.1.1-6) yields:

$$\varepsilon = \delta d_k - A_k \delta m_k$$

(3.1.1-7)

where $\delta d_k = d^o - d^c_k$.

For convenience, the subscript k (iteration number) is dropped; the expression then is:

$$\varepsilon = \delta d - A \delta m$$

(3.1.1-8)

According to the simplest least-squares or "Gauss-Newton" approach, I seek to minimize the cumulative squared error $S = \varepsilon^T \varepsilon$ with respect to the parameter change vector δm.

From (3.1.1-8), I have:

$$S = \varepsilon^T \varepsilon = (\delta d - A \delta m)^T (\delta d - A \delta m)$$

(3.1.1-9)

Minimization of S with respect to δm requires that:

$$\frac{\partial S}{\partial \delta m} = 0$$

(3.1.1-10)

Differentiation with respect to a vector is described by Graybill (1969) and implies that $\partial S / \partial \delta m_j = 0$ for $j = 1, 2, \cdots, p$.

Substituting (3.1.1-9) into (3.1.1-10) gives:

$$\frac{\partial}{\partial \delta m} \left(\delta m^T A^T A \delta m - \delta d^T A A \delta m - \delta m^T A^T \delta d + \delta d^T \delta d \right) = 0$$

(3.1.1-11)

Carrying out the differentiation with respect to δm, I obtain the so-called "normal equations":

$$A^T A \delta m = A^T \delta d$$

(3.1.1-12)

whose solution for the parameter change vector δm is:

$$\delta m = \left(A^T A \right)^{-1} A^T \delta d$$

(3.1.1-13)

which is also known as the Gauss-Newton solution.

3.1.2 Joint inversion of magnetic field and analytic signal

Joint inversion consists in finding a model that fits two sets of data. According to the Least-squares approach, I seek to minimize the cumulative squared error $S = \beta_f \varepsilon_f^T \varepsilon_f + \beta_g \varepsilon_g^T \varepsilon_g$ for two sets of data with respect to the parameter change vector δm.

From equation (3.1.1-9), I have:

$$S = \left(\beta_f \delta f - \beta_f A_f \delta m \right)^T \left(\beta_f \delta f - \beta_f A_f \delta m \right) + \left(\beta_g \delta g - \beta_g A_g \delta m \right)^T \left(\beta_g \delta f - \beta_g A_g \delta m \right)$$

(3.1.2-1)

where, β_f and β_g are the trade-off parameters for magnetic field and analytic signal respectively. δf and δg are difference between observation data and model response for magnetic field and analytic signal respectively. A_f and A_g are sensitivity matrixes for magnetic field and analytic signal respectively.

According to above, the solution for the parameter change vector δm is:

$$\delta m = \left(\beta_f^2 A_f^T A_f + \beta_g^2 A_g^T A_g\right)^{-1}\left(\beta_f^2 A_f^T \delta f + \beta_g^2 A_g^T \delta g\right)$$

(3.1.2-2)

I can combine the two sets of data for magnetic field and analytic signal. They are written as follow:

$$A = \begin{bmatrix} \beta_f A_f \\ \beta_g A_g \end{bmatrix}$$

(3.1.2-3)

and:

$$\delta d = \begin{bmatrix} \beta_f \delta f \\ \beta_g \delta g \end{bmatrix}$$

(3.1.2-4)

Substituting, the equation (3.1.2-3) and (3.1.2-4) in to (3.1.2-2), I can obtain the equation:

$$\delta m = \left(A^T A\right) A^T \delta d.$$

(3.1.2-5)

Equation (3.1.2-5) is the same as the equation (3.1.1-13).

3.1.3 Singular value decomposition and Marquardt's factor

It is well known that the matrix $A^T A$ is singular or nearly singular. This may cause divergence of the solution or slow down convergence. In order to reduce these difficulties, I impose a constraining condition. There are two popular methods to solve this problem.

First I can use the Marquardt-Levenberg method that was introduced by Levenberg (1944) and later described in detail by Marquardt (1963). The main idea of this method is to add a "damping factor", which is the energy of the elements of the parameter change, to prevent unbounded oscillations in the solution. The expression is written as follow:

$$\delta m = \left(A^T A + \lambda I \right)^{-1} A^T \delta d$$

<div align="right">(3.1.3-1)</div>

where λ is "damping factor".

Second I can use the SVD decomposition that was developed by Golub and Reinsch (1970) into an efficient algorithm. The main idea of this method is to erase the singular or nearly singular value among the singular matrix. The expression is written as follow:

$$A = U \Lambda V^T$$

<div align="right">(3.1.3-2)</div>

where U is the $N \times N$ matrix and V is the $P \times P$ Jacobian matrix,

$$\Lambda = \begin{vmatrix} s_1 & 0 & \cdots & 0 \\ 0 & s_2 & & \vdots \\ \vdots & & \ddots & \vdots \\ 0 & \cdots & \cdots & s_P \\ \vdots & & & \vdots \\ 0 & \cdots & \cdots & 0 \end{vmatrix}_{N \times P}$$

<div align="right">(3.1.3-3)</div>

Hence:

$$\delta m = V \Lambda^{-1} U^T \delta d$$

<div align="right">(3.1.3-4)</div>

In their article Lines and Treitel (1984) introduce a method of including Marquardt's method in the SVD formulation. This prescription for avoiding singularities has been treated by Lawson and Hanson (1974) and by Vozoff and Jupp (1975), among others.

I recall that the solution to the modified normal equations (3.1.3-1) is:

$$\delta m = \left(A^T A + \beta I \right)^{-1} A^T \delta d$$

<div align="right">(3.1.3-5)</div>

Substitution (3.1.3-2) into $A^T A$

$$A^T A = V \Lambda^2 V^T$$

<div align="right">(3.1.3-6)</div>

So that:

$$\left(A^T A + \lambda I \right) = V \Lambda^2 V^T + \lambda I$$

<div align="right">(3.1.3-7)</div>

The matrix can be changed to:

$$\left(A^T A + \lambda I\right) = V\left(\Lambda^2 + \lambda I\right)V^T$$

(3.1.3-8)

Hence,

$$\left(A^T A + \lambda I\right)^{-1} = V\left(\Lambda^2 + \lambda I\right)^{-1}V^T$$

(3.1.3-9)

where the $\left(\Lambda^2 + \lambda I\right)^{-1}$ is the $P \times P$ diagonal matrix of the form:

$$\left(\Lambda^2 + \lambda I\right)^{-1} = \begin{vmatrix} \dfrac{1}{s_1^2 + \lambda} & 0 & \cdots & 0 \\ 0 & \dfrac{1}{s_2^2 + \lambda} & & \vdots \\ \vdots & & \ddots & \vdots \\ 0 & \cdots & \cdots & \dfrac{1}{s_P^2 + \lambda} \end{vmatrix}_{P \times P}$$

Substitution of (3.1.3-2) and (3.1.3-9) into (3.1.3-5) lead to:

$$\delta m = V\left(\Lambda^2 + \lambda I\right)^{-1} V^T V \Lambda U^T \delta d$$

(3.1.3-10)

Replace $\left(\Lambda^2 + \lambda I\right)^{-1} V^T V \Lambda$ by a matrix to obtain:

$$\delta m = V diag\left(\dfrac{s_i}{s_i^2 + \lambda}\right) U^T \delta d$$

(3.1.3-11)

where $diag\left(\dfrac{s_i}{s_i^2 + \lambda}\right)$ is a $P \times N$ matrix of the form:

$$diag\left(\dfrac{s_i}{s_i^2 + \lambda}\right) = \begin{vmatrix} \dfrac{s_1}{s_1^2 + \lambda} & 0 & \cdots & 0 & \cdots & 0 \\ 0 & \dfrac{s_2}{s_2^2 + \lambda} & & \vdots & & \vdots \\ \vdots & & \ddots & \vdots & & \vdots \\ 0 & \cdots & \cdots & \dfrac{s_P}{s_p^2 + \lambda} & \cdots & 0 \end{vmatrix}_{P \times N}$$

and λ is Marquardt's damping factor. It now becomes clear how λ can obviate the problem of matrix singularities; even if $\lambda \to 0$, division by zero does not occur.

3.2 Computational aspect

The solution (model parameters) can be found by starting with an initial estimation of the parameters and iteratively computing a correction to the parameters until an acceptable fit is found between the observed and the computed data. This is the basic way to resolve the inversion problem. There are some specific calculations to the joint inversion of the total anomalous magnetic field and analytic signal data due to a vertical right circular cylinder with arbitrary polarization.

In this section, I present the details for resolving the problem, including forward modeling, normalization of the dataset, sensitivity matrix, trade off parameter, and convergence. Finally, I draw the structure diagram to perform joint inversion.

3.2.1 Forward modeling of magnetic field anomaly and analytic signal

The first step for carrying out joint inversion is forward modeling of the magnetic field anomaly and analytic signal. I use the expression (2.2-1) for the magnetic anomaly by Singh and Sabina (1978), and the expression (2.1-2) for the analytic signal by FFT. The two expressions are recalled as follow:

$$f = 2\pi a \cdot J_{tot}\left[(C-A)\cdot I(1,0;0)-(E-A)\cdot\frac{1}{r}I(1,1;-1)-BI(1,1;0)\right]$$

$$(3.2.1\text{-}1)$$

and,

$$g = |\vec{g}| = \sqrt{\left(\frac{\partial f}{\partial x}\right)^2+\left(\frac{\partial f}{\partial y}\right)^2+\left(\frac{\partial f}{\partial z}\right)^2}.$$

$$(3.2.1\text{-}2)$$

The detailed computation of these expressions has been discussed in chapter 2.

3.2.2 Normalizing magnetic field anomaly and analytic signal

In order to combine the two sets of data, both sets which are either observation data or modeled response data have to be normalized by the root-mean-square of observation data (magnetic field and analytic signal).

Normalization of the magnetic field observations is done as follow:

$$Nor_f = \frac{1}{\sqrt{\sum_{i=1}^{N} f_i^2 / N}}$$

(3.2.2-1)

where f_i is the observed magnetic field data , N is the number of the observation data.

Normalization of the analytic field data is done in a same way:

$$Nor_g = \frac{1}{\sqrt{\sum_{i=1}^{N} g_i^2 / N}}$$

(3.2.2-2)

Where g_i is observed analytic data, N is the number of the observation data.

Hence:

$$f^o = Nor_f f^o,$$

(3.2.2-3)

$$f^c = Nor_f f^c,$$

(3.2.2-4)

$$g^o = Nor_g g^o,$$

(3.2.2-5)

$$g^c = Nor_g g^c.$$

(3.2.2-6)

where f^o and g^o are the observed magnetic field and analytic signal data respectively, f^c and g^c are the modeled magnetic field and analytic signal respectively data .

The observed and modeled magnetic field and analytic signal data are normalized during the joint inversion computation.

3.2.3 Sensitivity calculation

The sensitivity matrix is the data kernel that relates the model and its response. In this case, the sensitivity matrix A is the $N \times P$ Jacobian matrix with elements that are partial derivatives with regards to the parameters. The number of rows (N) is the number of observation data and the number of columns (P) is the number of model parameter.

The element of sensitivity matrix can be expressed as follow:

$$A_{ij} = \frac{\partial d_i}{\partial m_j}$$

(3.2.3-1)

where, $(i = 1, \quad 2, \quad \cdots, \quad N)$ is the number of observation data and $(j = 1, \quad 2, \quad \cdots, \quad P)$ is the number of parameters.

The finite difference method is used to calculate elements of the sensitivity matrix. The step of difference is 1. The expression (3.2.3-1) is rewritten as follow:

$$A_{ij} = d_i\left(m_1, \cdots, m_j + 0.5, \cdots m_P\right) - d_i\left(m_1, \cdots, m_j - 0.5, \cdots m_P\right)$$

(3.2.3-2)

3.2.4 Trade-off parameters between magnetic field and analytic signal

The trade-off parameters are the weighting to the two sets of data. It is to minimize the cumulative squared errors of the magnetic field anomaly and analytic signal. So the trade-off parameters are changed for each iteration.

According to the solution of joint inversion, I recall the equation (3.1.2-1) is:

$$S = \left(\beta_f \delta f - \beta_f A_f \delta m\right)^T \left(\beta_f \delta f - \beta_f A_f \delta m\right) + \left(\beta_g \delta g - \beta_g A_g \delta m\right)^T \left(\beta_g \delta f - \beta_g A_g \delta m\right)$$

(3.2.4-1)

In order to constrain the trade-off parameters, I assume that:

$$\beta_f + \beta_g = 1$$

(3.2.4-2)

Substituting (3.2.4-2) into (3.2.4-1) I obtain:

$$S = \left(1 - \beta_g\right)^2 \left(\delta f - A_f \delta m\right)^T \left(\delta f - A_f \delta m\right) + \beta_g^2 \left(\delta g - A_g \delta m\right)^T \left(\delta g - A_g \delta m\right) \tag{3.2.4-3}$$

Minimization of S with respect to β_g requires that:

$$\frac{\partial S}{\partial \beta_g} = 0 \tag{3.2.4-4}$$

Substituting (3.2.4-3) into (3.2.4-4) I obtain:

$$2(\beta_g - 1)(\delta f - A_f \delta m)^T (\delta f - A_f \delta m) + 2\beta_g (\delta g - A_g \delta m)^T (\delta g - A_g \delta m) = 0 \tag{3.2.4-5}$$

Hence:

$$\beta_g = \frac{\left(\delta f - A_f \delta m\right)^T \left(\delta f - A_f \delta m\right)}{\left(\delta f - A_f \delta m\right)^T \left(\delta f - A_f \delta m\right) + \left(\delta g - A_g \delta m\right)^T \left(\delta g - A_g \delta m\right)} \tag{3.2.4-6}$$

and:

$$\beta_f = \frac{\left(\delta g - A_g \delta m\right)^T \left(\delta g - A_g \delta m\right)}{\left(\delta f - A_f \delta m\right)^T \left(\delta f - A_f \delta m\right) + \left(\delta g - A_g \delta m\right)^T \left(\delta g - A_g \delta m\right)} \tag{3.2.4-7}$$

3.2.5 Convergence

The convergence of successive iterations is monitored by the root-mean-squares (rms) error criterion:

$$rms_k = \sqrt{S / N} \tag{3.2.5-1}$$

where, S is the squares cumulative squared error which is calculated by (3.1.2-1). N is the number of observation data. $\left(k = 1, 2, \cdots, M\right)$ is the number of iterations.

3.2.6 Joint inversion technique

I present the program structure diagram (Figure 3.1) that displays the computational process of joint inversion of the magnetic field anomaly and its analytic signal.
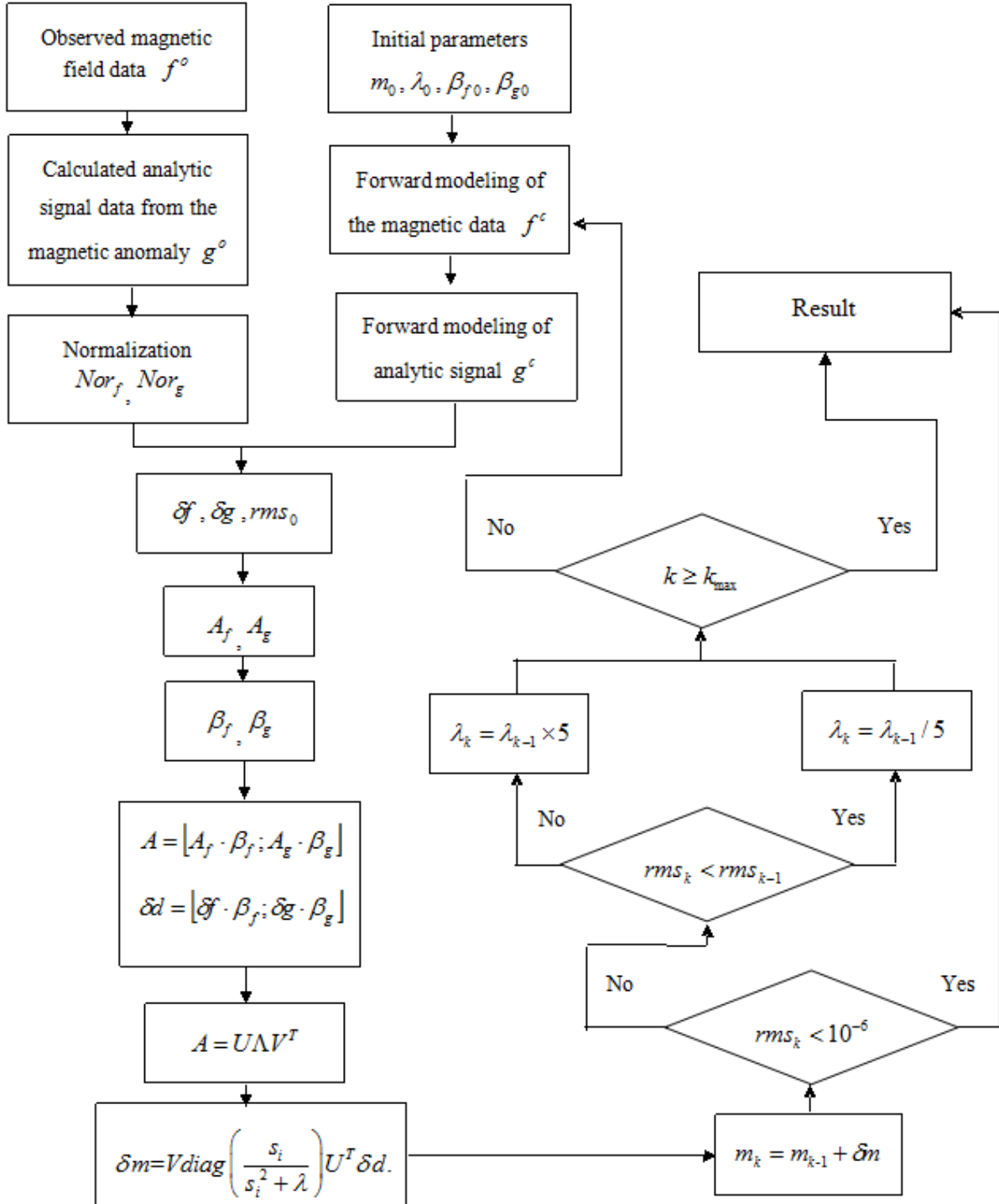
Figure 3.1: Flow chart for joint inversion computation

3.3   Synthetic examples

In this section, I present three semi-infinite vertical cylinder models to simulate the kimberlite pipes. The geomagnetic field is the same for each model with amplitude of 57,000nT, inclination 74˚ and declination -12˚. It is the geomagnetic field observed in the region of Ekati, Canada. The survey area for which the modeled responses are computed is 1,000m by 1,000m and is sampled by 41 x 41 sites (1681 receivers); the data spacing is 25m. The number of iterations is 30, the initial damping factor is 1 and the initial trade off parameter is 0.5. When the data misfit of magnetic field and analytic signal is less than 10^{-6} , the iteration of inversion is broken.

The first model is a semi-infinite vertical cylinder with a diameter of 248m, centered in the survey area and located at a depth of 69m. The amplitude of TM is $J_{tot} = 768nT$, the direction of TM is $I_{tot} = 69^{o}$ and $D_{tot} = -19^{o}$.

Table 3.1 and figure 3.2 show that the results of joint inversion of magnetic field and analytic signal clearly recover the model parameters for model 1. Figure 3.3 shows that the data misfits of magnetic field and analytic signal tend to minimum respectively, and the parameter changes tend to zero. The damping factor decreases with increasing iteration number. The CPU time for joint inversion is 156.67s. The inversion is stopped at iteration eighteenth.

Table 3.1: Joint inversion of magnetic field and analytic signal for model 1.

	Mag.(nT)	In.(˚)	De.(˚)	X.(m)	Y.(m)	Dia.(m)	Dep.(m)
Model	768	69	-19	500	500	248	69
Initial	100	45	-45	300	300	140	150
Final	768	69	-19	500	500	248	69
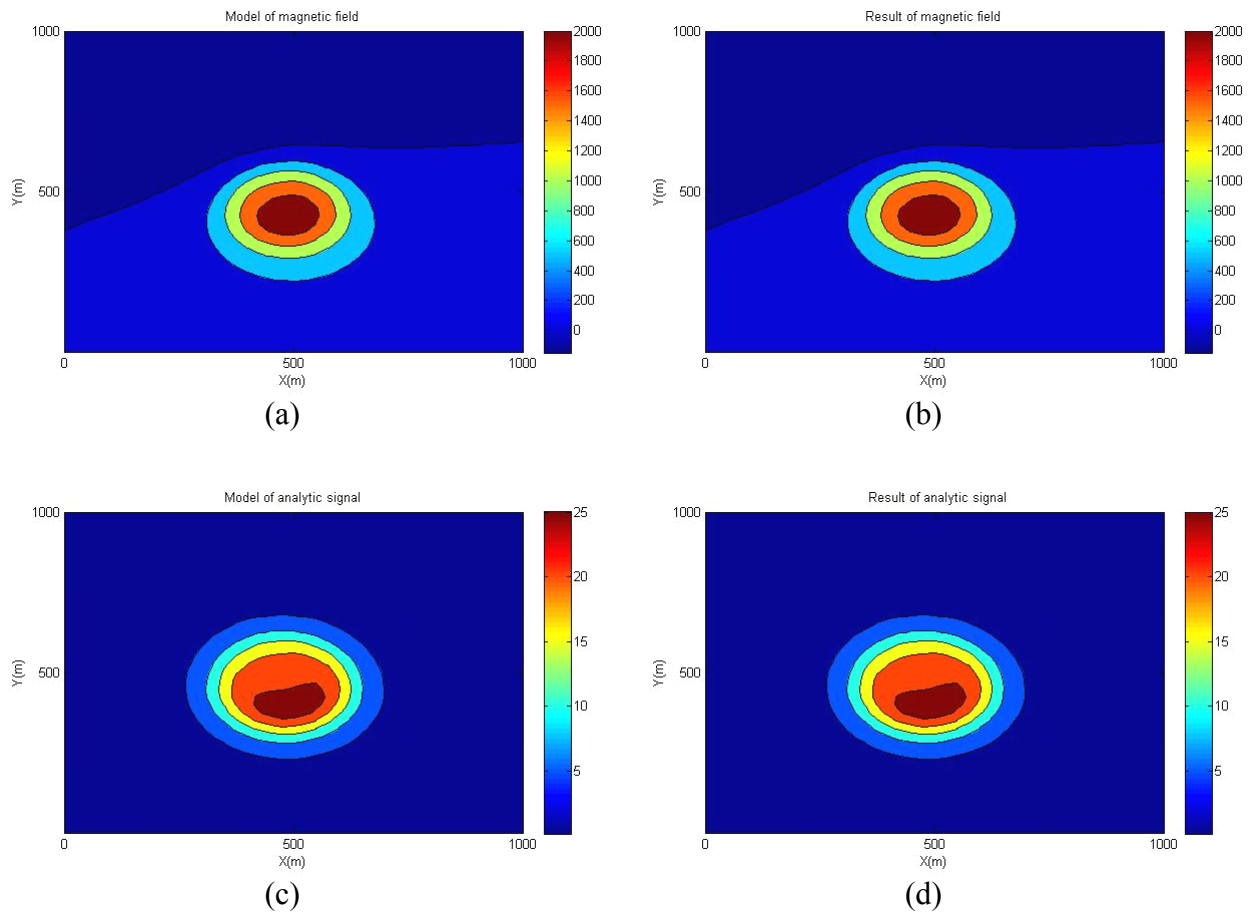
Figure 3.2: Model 1: joint inversion of magnetic field and analytic signal. X-axes is directed to the east and Y-axes is directed to the north. (a) Modeled total-field magnetic anomaly, (b) total magnetic field response to the inverted model, (c) modeled analytic signal, (d) analytic signal response to the inverted model.
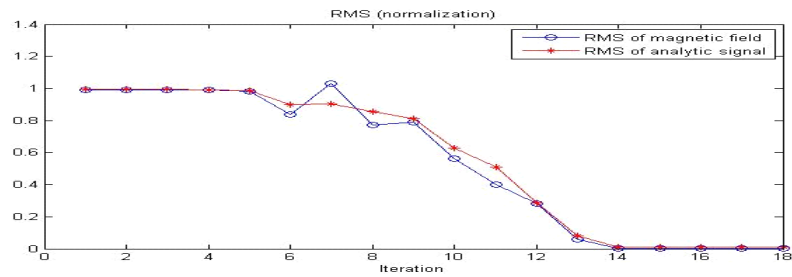
(a)
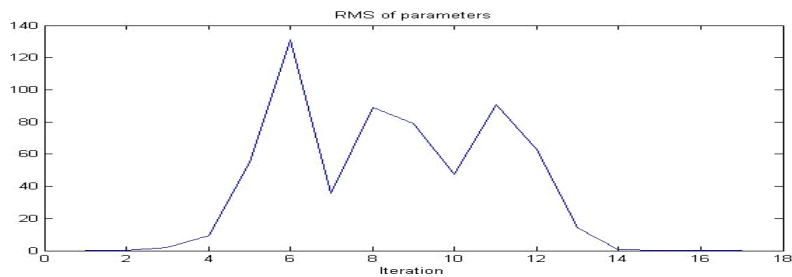
(b)
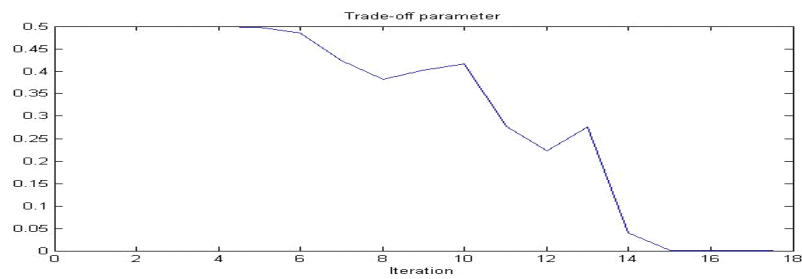
(c)
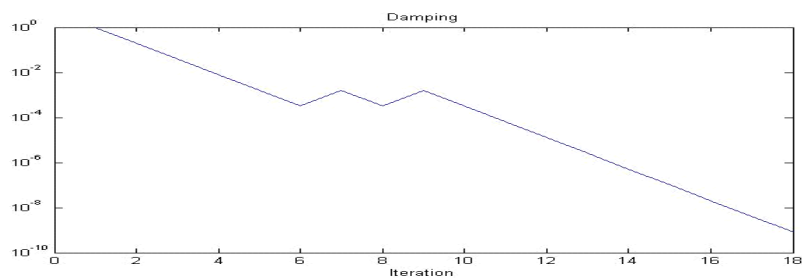
(d)

Figure 3.3: Model 1: (a) data misfits of magnetic field and analytic signal respectively, (b) parameter changes, (c) trade-off parameter, and (d) damping factor.

The second model is a semi-infinite vertical cylinder with a diameter of 248m, centered in the survey area and located at a depth of 69m. The amplitude of TM is $J_{tot} = 768nT$, the direction of TM is $I_{tot} = -22^{o}$ and $D_{tot} = 47^{o}$. Table 3.2 and figure 3.4 show that the results of joint inversion of magnetic field and analytic signal clearly recover the model parameters for model 2. Figure 3.5 shows that the data misfits of magnetic field and analytic signal tend to minimum respectively, and the parameter changes tend to zero. The damping factor decreases with increasing iteration number. The CPU time of joint inversion is 149.87s. The inversion is stopped at iteration seventeenth.

Table 3.2: Joint inversion of magnetic field and analytic signal for model 2.

	Mag.(nT)	In.(˚)	De.(˚)	X.(m)	Y.(m)	Dia.(m)	Dep.(m)
Model	768	-22	47	500	500	248	69
Initial	100	-45	15	300	300	140	150
Final	768	-22	47	500	500	248	69
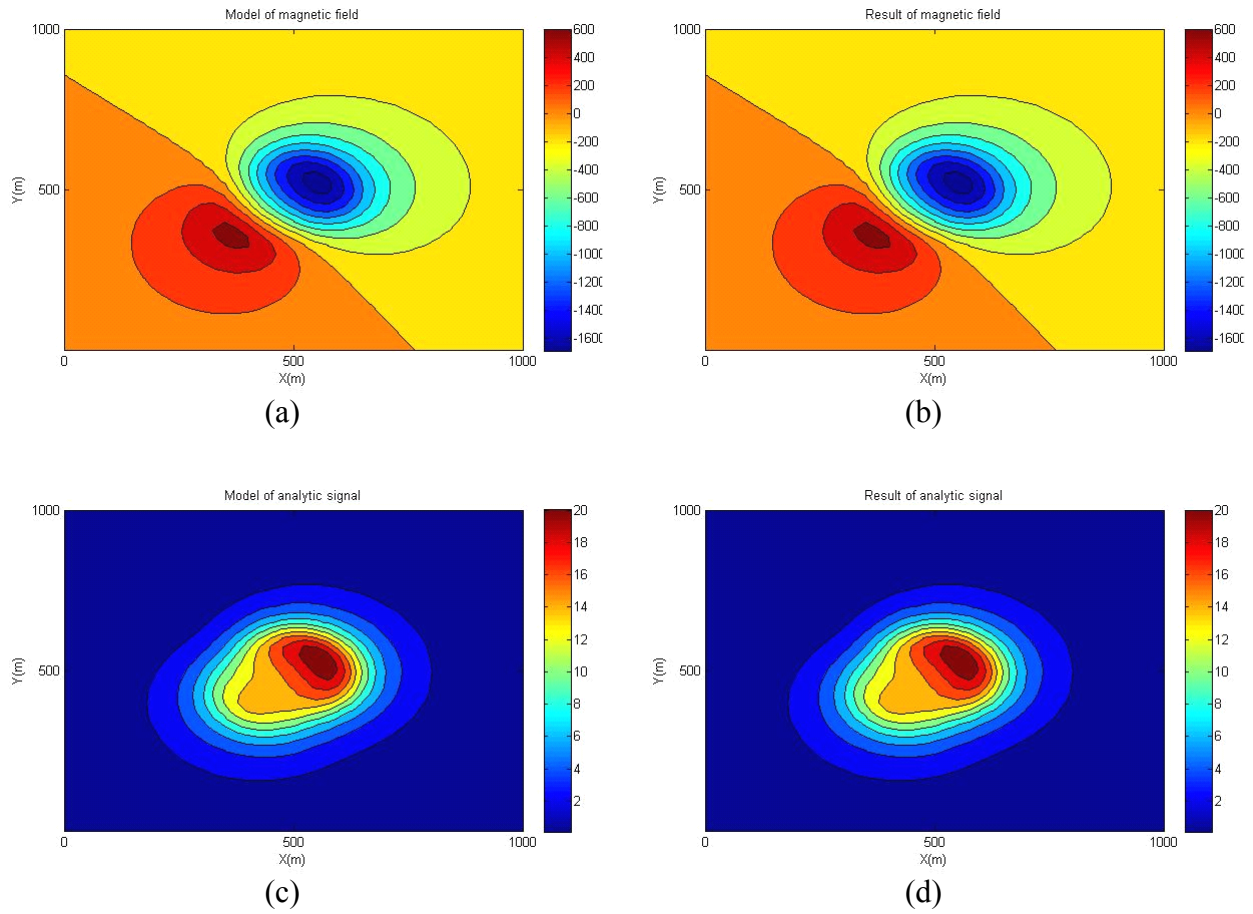
Figure 3.4: Model 2: joint inversion of magnetic field and analytic signal. X-axes is directed to the east and Y-axes is directed to the north. (a) Modeled total-field magnetic anomaly, (b) total magnetic field response to the inverted model, (c) modeled analytic signal, (d) analytic signal response to the inverted model.
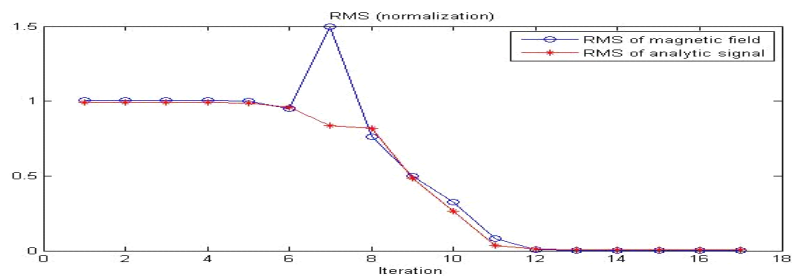
(a)
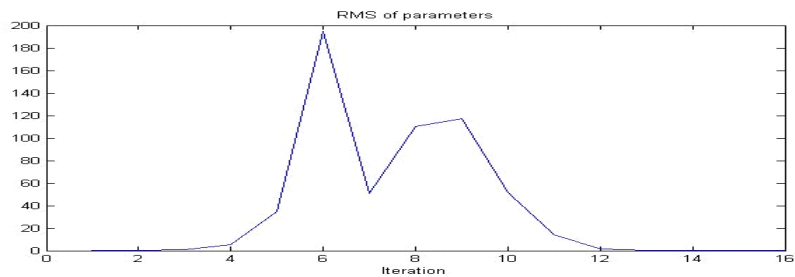
(b)
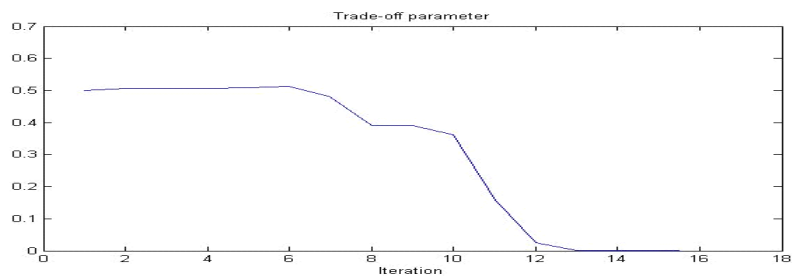
(c)
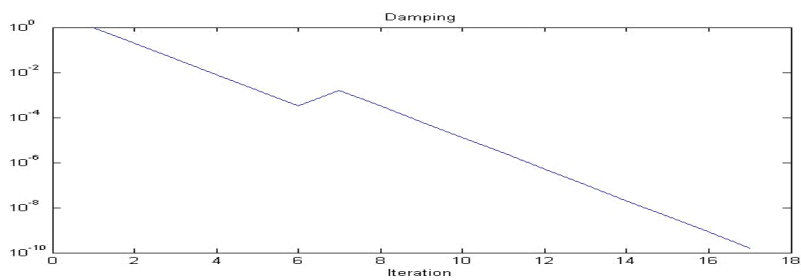
(d)

Figure 3.5: Model 2: (a) data misfits of magnetic field and analytic signal respectively, (b) parameter changes, (c) trade-off parameter, and (d) damping factor.

The third model is a semi-infinite vertical cylinder with a diameter of 334m, centered in the survey area and located at a depth of 26m. The amplitude of TM is $J_{tot} = 289nT$, the direction of TM is $I_{tot} = 143^o$ and $D_{tot} = -31^o$.

Table 3.3 and figure 3.6 show that the results of joint inversion of magnetic field and analytic signal clearly recover the model parameters for model 3. Figure 3.7 shows that the data misfits of magnetic field and analytic signal tend to minimum respectively, and the parameter changes tend to zero. The damping factor decreases with increasing iteration number. The CPU time of joint inversion is 168.43s. The inversion is stopped at iteration nineteenth.

Table 3.3: Joint inversion of magnetic field and analytic signal for model 3.

	Mag.(nT)	In.(˚)	De.(˚)	X.(m)	Y.(m)	Dia.(m)	Dep.(m)
Model	289	143	-31	500	500	334	26
Initial	1000	90	0	300	300	140	100
Results	289	143	-31	500	500	334	26
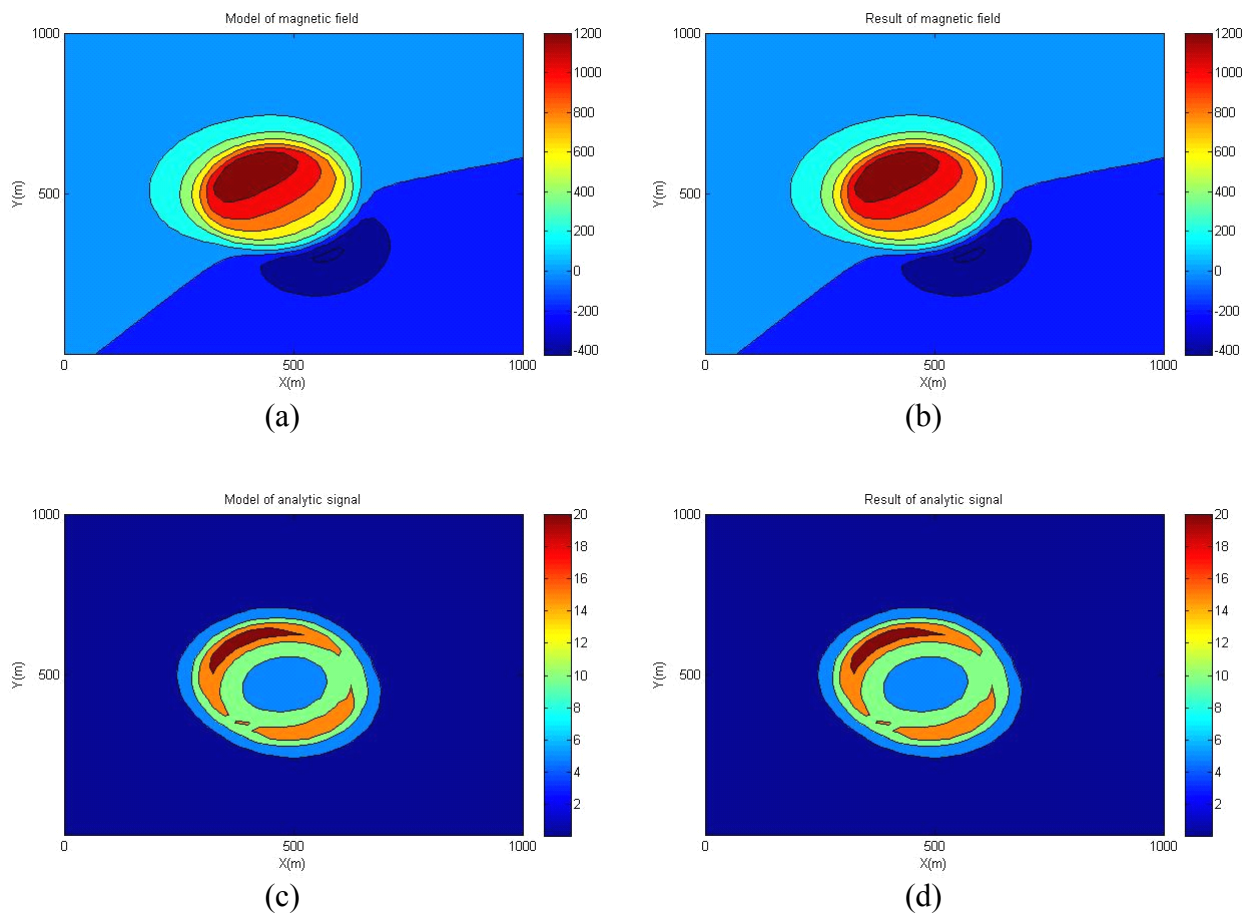
Figure 3.6: Model 3: joint inversion of magnetic field and analytic signal. X-axes is directed to the east and Y-axes is directed to the north. (a) Modeled total-field magnetic anomaly, (b) total magnetic field response to the inverted model, (c) modeled analytic signal, (d) analytic signal response to the inverted model.
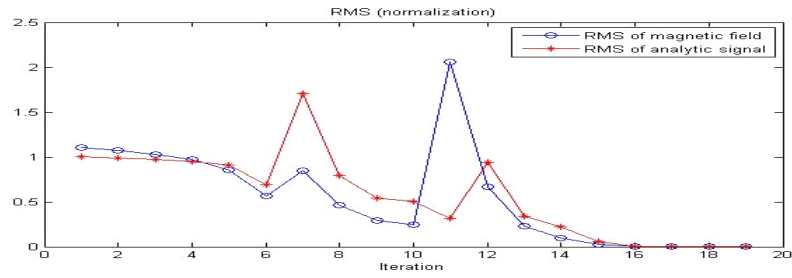
(a)
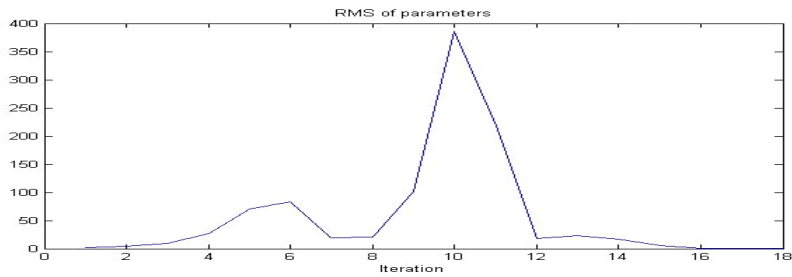
(b)
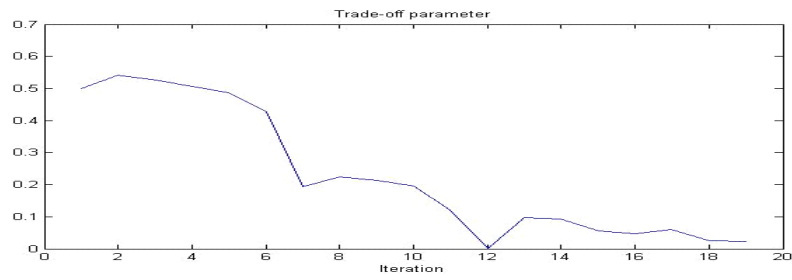
(c)
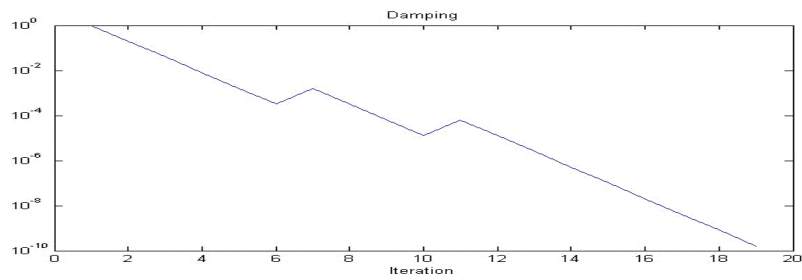
(d)

Figure 3.7: Model 3: (a) data misfits of magnetic field and analytic signal respectively, (b) parameter changes, (c) trade-off parameter, and (d) damping factor.

The fourth model is a semi-infinite vertical cylinder with a diameter of 154m, centered in the survey area and located at a depth of 163m. The amplitude of TM is $J_{tot} = 2488nT$, the direction of TM is $I_{tot} = 83^o$ and $D_{tot} = -8^o$.

Table 3.4 and figure 3.8 show that the results of joint inversion of magnetic field and analytic signal clearly recover the model parameters for model 4. Figure 3.9 shows that the data misfits of magnetic field and analytic signal tend to minimum respectively, and the parameter changes tend to zero. The damping factor decreases with increasing iteration number. The CPU time of joint inversion is 158.29s. The inversion is stopped at iteration eighteenth.

Table 3.4: Joint inversion of magnetic field and analytic signal for model 4.

	Mag.(nT)	In.(˚)	De.(˚)	X.(m)	Y.(m)	Dia.(m)	Dep.(m)
Model	2488	83	-8	500	500	154	163
Initial	200	-45	-45	300	300	320	60
Results	2488	83	-8	500	500	154	163
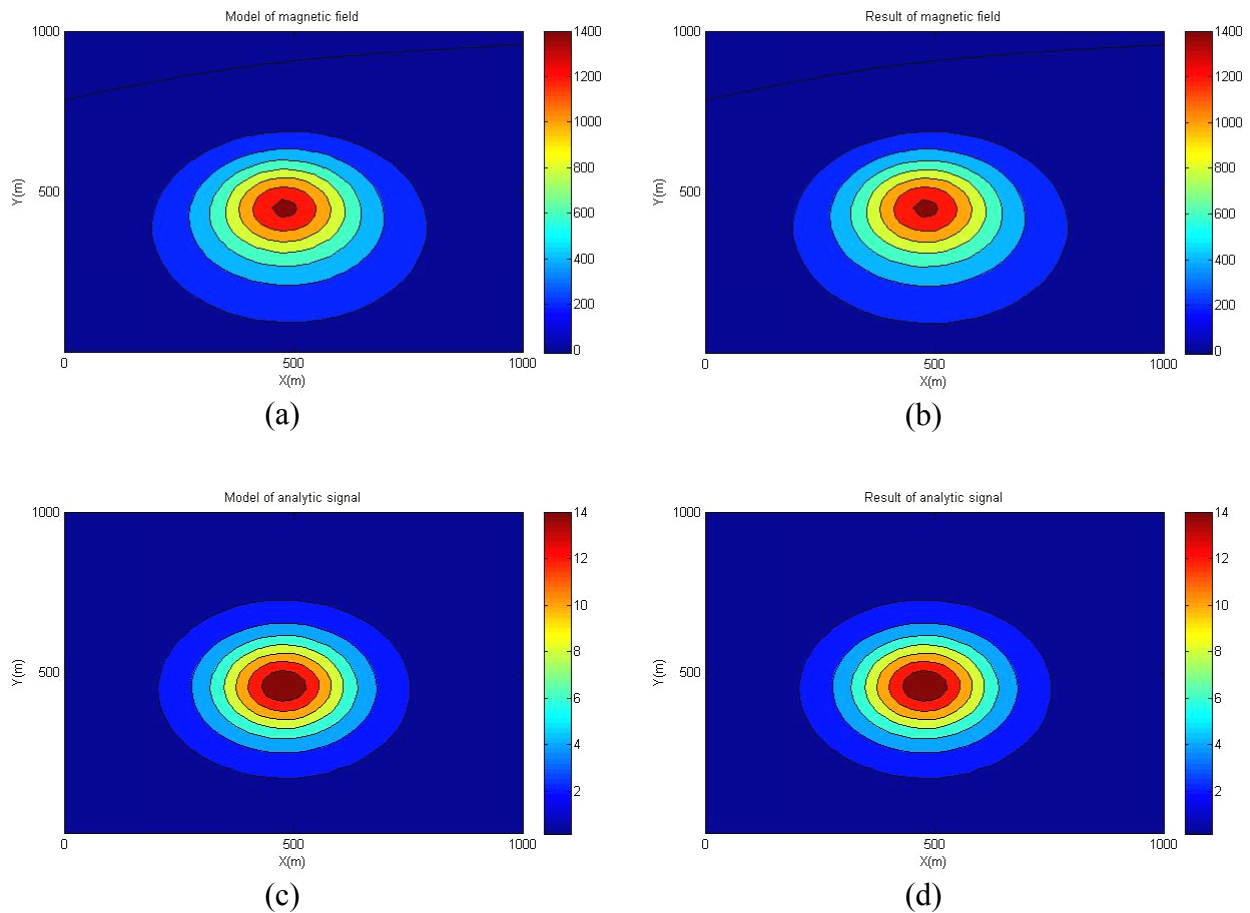
Figure 3.8: Model 4: joint inversion of magnetic field and analytic signal. X-axes is directed to the east and Y-axes is directed to the north. (a) Modeled total-field magnetic anomaly, (b) total magnetic field response to the inverted model, (c) modeled analytic signal, (d) analytic signal response to the inverted model.
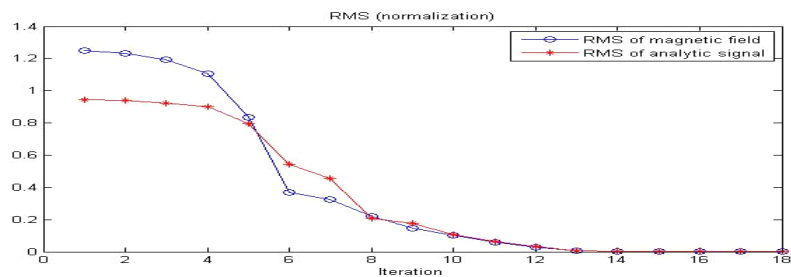
(a)
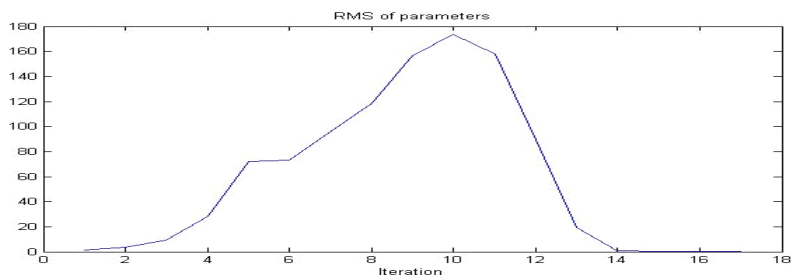
(b)
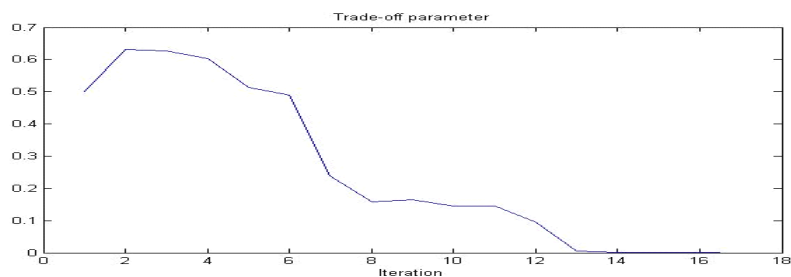
(c)
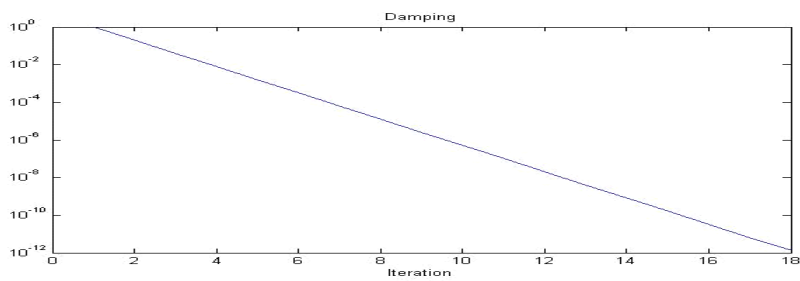
(d)

Figure 3.9: Model 4: (a) data misfits of magnetic field and analytic signal respectively, (b) parameter changes, (c) trade-off parameter, and (d) damping factor.

From the tables 3.1 to 3.4 and figures 3.2 to 3.9, the results of joint inversion of magnetic field and analytic signal clearly recovers the model parameters for each model, the initial parameters being arbitrarily selected. The data misfits of magnetic field and analytic signal both tend to a minimum, and the rms of parameter changes tend to zero. The damping factor decreases with increasing iteration number. Therefore, the proposed joint inversion of magnetic field and analytic signal is stable and leads to accurate estimation of the parameters.

The curves of trade-off parameters for each model are asymptotic to zero, rather than 0.5. The reason is the data misfits of magnetic field and analytic signal are approached to zero respectively that similar to the singular values without noise. Therefore, the trade-off parameters cannot reflect the real weighting of two set of data. Therefore, the joint inversion of magnetic field and analytic signal is stable and accuracy.

3.4 Conclusion

The joint inversion of magnetic field and analytic signal has been successfully implemented. The algorithm is 3D parametrical inversion of total-field magnetic data and its analytic signal magnetic data. It is based on Gauss-Newton method solved by singular value decomposition and Marquardt's factor. Validation and robustness of the algorithm have been tested using synthetic examples without noise. It is not sensitive to the right selection of initial parameters and reference parameters are unnecessary to recover the exact model parameters. Therefore, the algorithm is stable and accurate.

Chemam (2006) and Chen (2009) utilized amplitude of magnetic anomaly and its analytic signal to do the parametric inversion using the model of vertical cylinder in presence of RM with Gauss-Newton method to recover the magnetic and geometrical properties of kimberlite pipe. Although these algorithms are similar to the algorithm presented in this thesis, they are dependent on the initial parameters and reference parameters.

This inversion algorithm improves the parametric inversion techniques already developed using total-field and analytic signal magnetic data for recovering the geometrical parameters of a magnetic kimberlite pipe represented by a vertical cylinder.

CHAPTER 4   DETERMINING REMANENT MAGNETIZATION

The purpose of this chapter is to introduce the method to estimate the RM. First, I introduce the RM computation from the TM and the IM. Then, the frequency EM survey is proposed for estimating the magnetic susceptibility. Lastly, I illustrate the algorithm with synthetic examples.

4.1   Remanent magnetization computation

From the previous chapters I have shown how to obtain the TM from the magnetic anomaly and its analytic signal. It is the vector sum of IM and RM. Cheman (2006) introduced the formula to compute the RM. Figure 4.1, presented by Chen (2009), shows the relationship between the IM and RM. The TM can be expressed using the IM and RM as followed:

$$J_r = QJ_i \tag{4.1-1}$$

$$J_{tot} \cdot \sin\left(I_{tot}\right) = J_i \sin\left(I_i\right) + J_r \cdot \sin\left(I_r\right) \tag{4.1-2}$$

$$J_{tot} \cdot \cos\left(I_{tot}\right) \cdot \cos\left(D_{tot}\right) = J_i \cdot \cos\left(I_i\right) \cdot \cos\left(D_i\right) + J_r \cdot \cos\left(I_r\right) \cdot \cos\left(D_r\right) \tag{4.1-3}$$

$$J_{tot} \cdot \cos\left(I_{tot}\right) \cdot \sin\left(D_{tot}\right) = J_i \cdot \cos\left(I_i\right) \cdot \sin\left(D_i\right) + J_r \cdot \cos\left(I_r\right) \cdot \sin\left(D_r\right) \tag{4.1-4}$$

where, Q is the Königsberger ratio. J_{tot}, J_i and J_r are the intensities of total, induced and remanent magnetizations. I_{tot}, I_i and I_r are the inclinations of total, induced and remanent magnetizations. D_{tot}, D_i and D_r are the declinations of total, induced and remanent magnetizations.
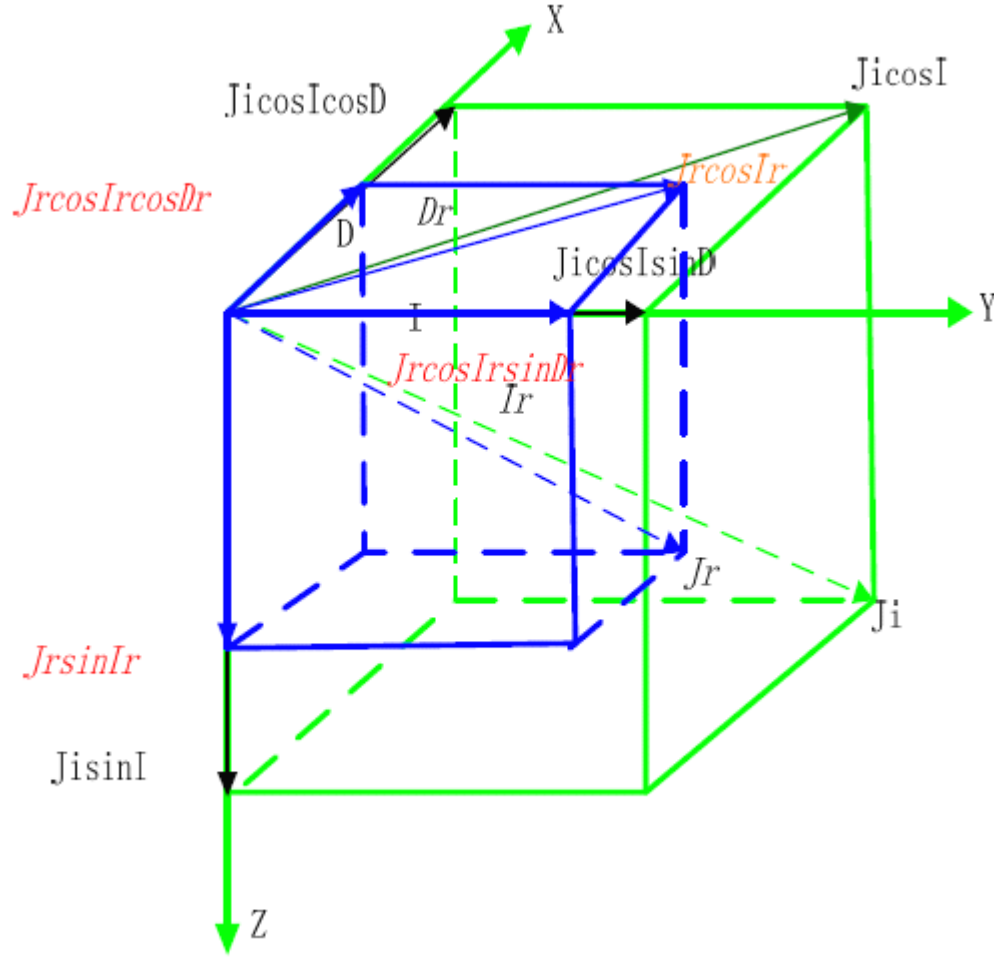
Figure 4.1: Geometry relationship between induced and remanent magnetizations

In general, most methods estimate the RM from the TM parameters and the direction of the IM. According to the four equations (4.1-1) to (4.1-4), there are five unknown parameters. This is an underdetermined system of equations with infinity of solutions. In order to obtain the RM, the intensity of IM or the Königsberger ratio has to be known.

If the intensity of IM is known, the solution of RM can be expressed as followed:

$$J_r = \sqrt{a^2 + b^2 + c^2} \tag{4.1-5}$$

$$I_r = \arctan\sqrt{\frac{c^2}{a^2 + b^2}} \tag{4.1-6}$$

$$D_r = \arctan\left(\frac{b}{a}\right)$$

(4.1-7)

$$Q = \sqrt{a^2 + b^2 + c^2} \,/\, J_i$$

(4.1-8)

where,

$$a = J_{tot} \cdot \cos(I_{tot}) \cdot \cos(D_{tot}) - J_i \cdot \cos(I_i) \cdot \cos(D_i).$$

$$b = J_{tot} \cdot \cos(I_{tot}) \cdot \sin(D_{tot}) - J_i \cdot \cos(I_i) \cdot \sin(D_i).$$

$$c = J_{tot} \cdot \sin(I_{tot}) - J_i \cdot \sin(I_i).$$

4.2 Estimating susceptibility by frequency EM

The intensity of IM is computed from the magnetic susceptibility and the intensity of geomagnetic field. The expression (1.2.3-1) is recalled:

$$J_i = \kappa T_0$$

(4.2-1)

where, κ is the susceptibility, T_0 is the intensity of geomagnetic field.

It is difficult using magnetic data interpretation to obtain the susceptibility in presence of RM, because TM generates the magnetic field response. Electromagnetic surveys are affected by the magnetic permeability of the structures under investigation (Zhang and Oldenburg, 1996) and interpretation of their responses can lead to estimation of the magnetic permeability. Fortunately RM does not affect them and therefore the careful interpretation of EM surveys can provide independent estimation of the magnetic susceptibility. Airborne magnetic and EM surveys are often carried out to map kimberlite pipes (Macnae, 1995). The relationship between the magnetic permeability and susceptibility is:

$$\mu = \mu_0 (1 + \kappa)$$

(4.2-1)

where, μ is the magnetic permeability, μ_0 is the permeability in vacuum and κ is the magnetic susceptibility.

In this section, I introduce the 1D inversion of frequency-domain EM data for magnetic susceptibility and electric conductivity as proposed by Zhang and Oldenburg (1996). The solutions are computed using the program "EM1DFM" published by UBC (University of British Columbia).

4.2.1 Introduction

Zhang and Oldenburg (1996) introduced an algorithm of one-dimensional inversion from a multi-frequency EM data set for obtaining the electric conductivity and magnetic susceptibility. Beard and Nyquist (1998) presented the best-fitting conductivity and susceptibility of a homogeneous half-space from frequency domain. Huang and Fraser (1998, 2002) presented the resistivity-depth algorithm and the apparent permeability algorithm, both of which are multi-frequency transforms from a half-space model. Zhdanov and Pavlov (2001) calculated one-dimension sections of conductivity and susceptibility from time domain.

Farquharson and Oldenburg (2003) describe the inversion algorithm used to extract conductivity and magnetic permeability. The details of forward and inverse solutions are not discussed here. The inverse problem is formulated as an optimization problem to find the model that minimizes the objective function:

$$\Phi = \phi_d + \beta\phi_m - \gamma\phi_{LB}$$

(4.2.1-1)

where, ϕ_d is the traditional sum of squares measure of misfit between the observation data and the model data. ϕ_m is sum of squares measure of misfit between the reference model and the model computed which includes both the conductivity model and susceptibility model. β is the trade-off parameter to balance the usually opposing influences of minimizing the misfit and simplifying the model. $\gamma\phi_{LB}$ is the logarithmic barrier term that is used to enforce positivity of the magnetic susceptibility.

4.2.2 Program "EM1DFM"

The acronym "EM1DFM" stand for electromagnetics (EM), one-dimensional models (1D), frequency domain observations (F), and magnetic sources and receivers (M). The program was published by the University of British Columbia. An example of the Menu from the user interface is displayed in Figure 4.2.
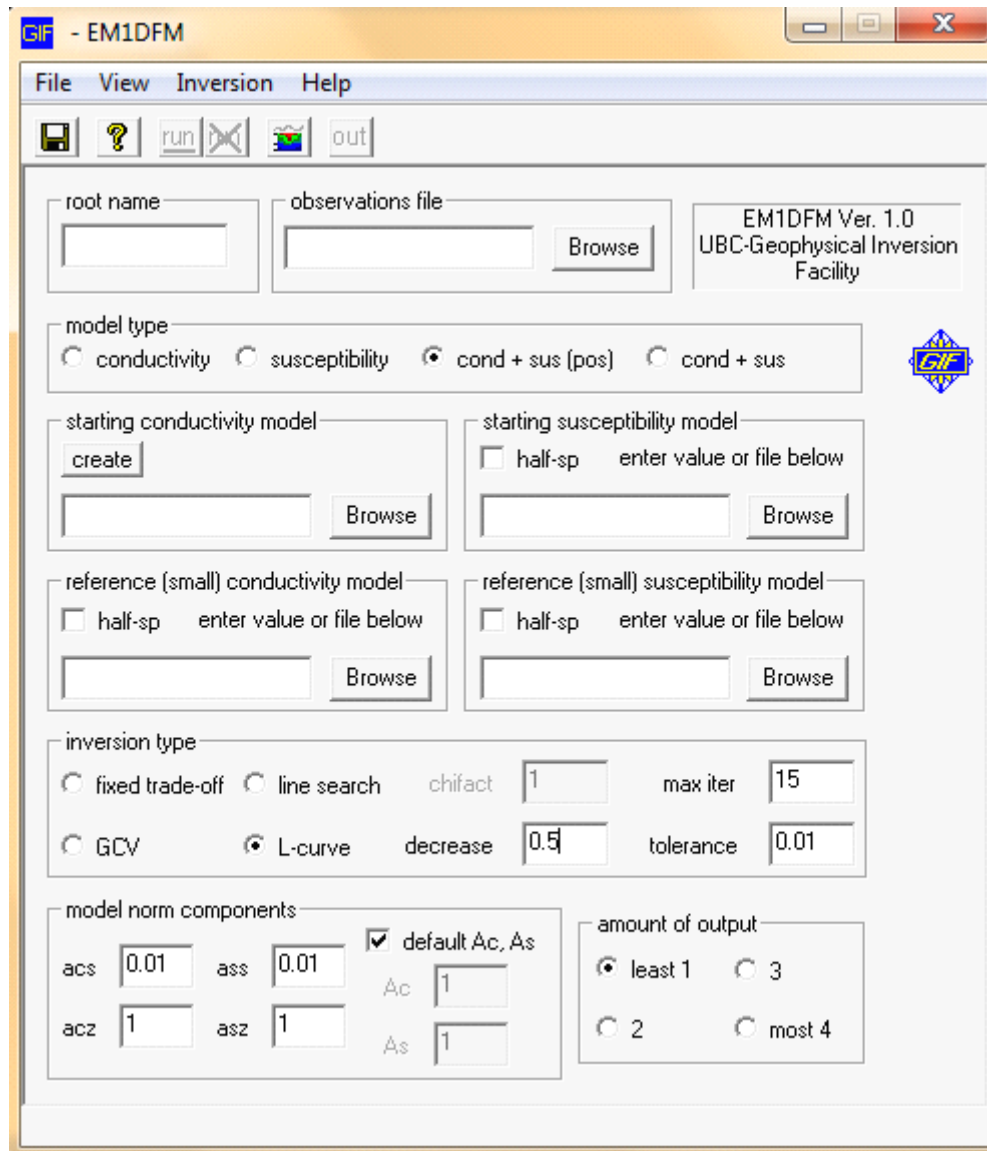
Figure 4.2: Screen shot of the interface for EM1DFM.

This inversion program is designed to construct one of four types of 1D models (an electrical conductivity model, or a strictly-positive magnetic susceptibility model, or both conductivity and strictly-positive susceptibility models, or both conductivity and susceptibility

models), using any type of geophysical frequency domain loop-loop data using one of four variations of the inversion algorithm ('fixed trade-off' specifies that constant trade-off parameter in the objective function being minimized, or 'line search' specifies that the trade-off parameter is automatically chosen to achieve a user-supplied target misfit, or 'GCV' specifies that the trade-off parameter is automatically chosen using the GCV criterion, or 'L-curve' specifies that the trade-off parameter is automatically chosen using the L-curve criterion).

In order to control the inversion, the different parameters are selected. The parameter 'chifact' is target misfit. The parameter 'decrease' is the change factor of weighting for model misfit and data misfit. The parameter 'max iter' is the maximum number of iterations to be carried out in an inversion. The parameter 'tolerance' is used in the tests of convergence for an inversion.

There are six coefficients on the model norm. The 'acs' and 'acz' are the balance between the conductivity and thickness of conductivity model. The 'ass' and 'asz' are the balance between the susceptibility and thickness of susceptibility model. The 'Ac' and 'As' are the weights for conductivity versus susceptibility models.

There are four options indicating the amount of output from the program. '1' provides for output of a brief convergence/termination report for each sounding plus the final two-dimensional composite model for all the soundings and the corresponding forward-modeled data. '2' provides output as for '1' plus the final one-dimensional model and corresponding forward-modeled data for each sounding. '3' provides output as for '2' plus the values of the various components of the objective function at each iteration in the inversion for each sounding. '4' provides output as for choice '3' plus an additional diagnostics file for each sounding which records the progress of the inversion for that sounding, a record of misfit, GCV function or L-curve curvature versus trade-off parameter, and a diagnostics file for the LSQR solution routine if it is used.

4.2.3 Synthetic examples

In this section, I present the responses two synthetic examples of 1D inversion from a single frequency EM data set for obtaining the electric conductivity and magnetic susceptibility. The 1D conductivity and susceptibility models at each location are stitched into a 2D section under the survey line. The synthetic data is modeled as a 1D response for each site considering the magnetic susceptibility and electrical conductivity existing under the site.

The synthetic examples mimic DIGHEM-style data. DIGHEM is a multiple-frequency multiple-configuration helicopter frequency system operated by Fugro Airborne Surveys (Toronto, ON). The in-phase and quadrature parts of the component of the secondary H-field orthogonal to the plane of the receiver coil are calculated for three horizontal coplanar coil pairs at nominal frequencies of 900, 7200 and 56000 Hz, and two vertical coaxial coil pairs at 1000 and 5500 Hz. The transmitter-receiver pairs are located at a height of 40m above the ground surface, and the coil separation is 8 meters for all frequencies except 56000 Hz, which has a coil separation of 6.3 meters due to its high signal strength. The number of samples along profile (sites) is 20 and the distance between each is 25m. The inversion used the GCV-based method for choosing the trade-off parameter with each iteration. The parameter 'iter' is 99, the parameter 'decrease' is 0.5, and the parameter 'tolerance' is 0.01. For the model norm components, the 'acs' and 'acz' are 0.01 and 1 respectively, the 'ass' and 'asz' are 0.01 and 1, the 'Ac' and 'As' are 1 and 100.

Two synthetic examples are used to test this code. The first model is a semi-infinite prism extending at the surface in a homogeneous host rock. The second model is a semi-infinite prism at depth embedded in a homogeneous host rock. Because of the code limitation, the inversion model must include at least three layers (including the basement).

The same initial model for each synthetic data was used and consisted in a homogeneous halfspace of conductivity 0.0001 S/m and susceptibility 0 SI units respectively. The depth to basement halfspace is 150m. There are two different reference models for each synthetic dataset: the first is such that the conductivity and susceptibility of reference models are equal to the anomalous, and the second is such that the conductivity and susceptibility of reference models are equal to the host rock.
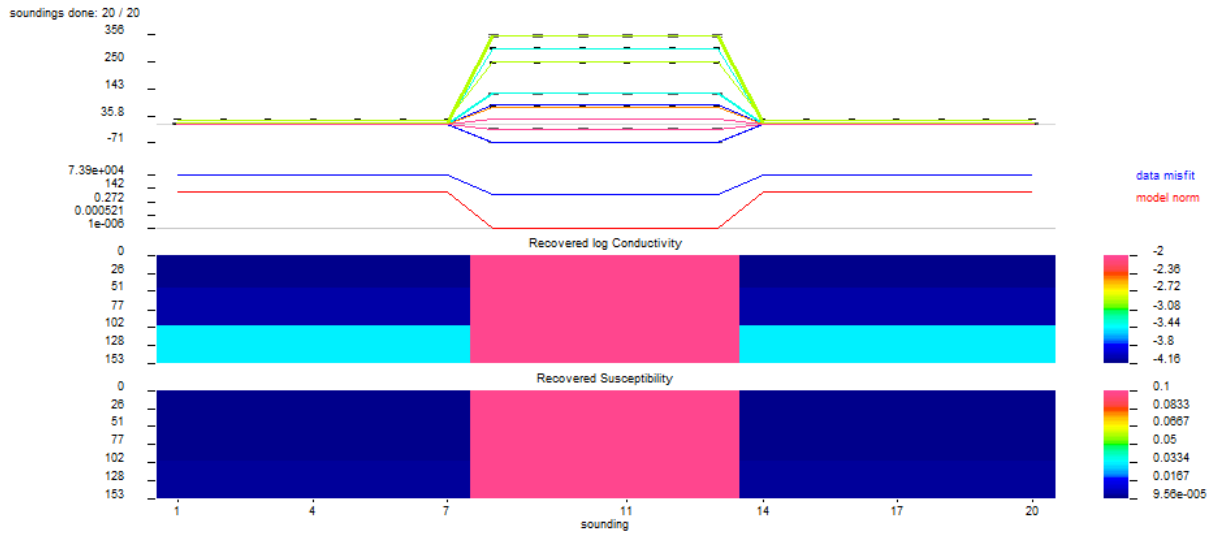
(a)
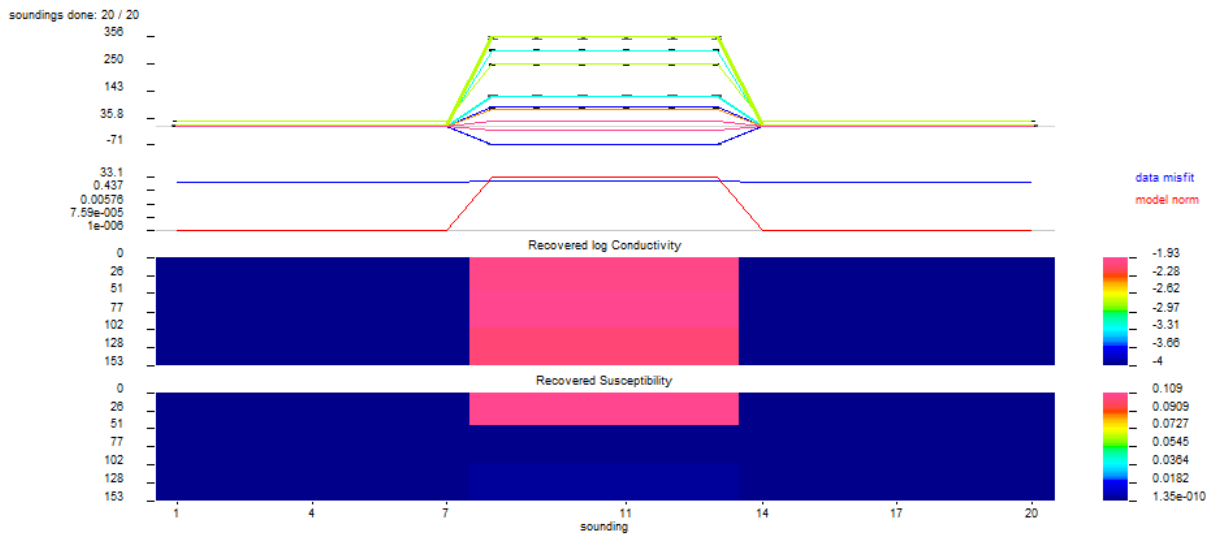
(b)

Figure 4.3: Inversion result of the semi-infinite prim model using EM1DFM software and synthetic data (top) and 20 recovered 1D models of conductivity and susceptibility concatenated into a 2D cross section under the survey line. True model: an outcropping vertical semi-infinite prism embedded in a homogeneous medium. Conductivity and susceptibility of the prism are 0.01 S/m and 0.1 SI units respectively, and conductivity and susceptibility of the background are 0.0001 S/m and 0 SI units. The reference models are a homogeneous half space of conductivity and susceptibility (a) 0.01 S/m and 0.1 SI units and (b) 0.0001 S/m and 0.0 SI units respectively.

(a)

(b)
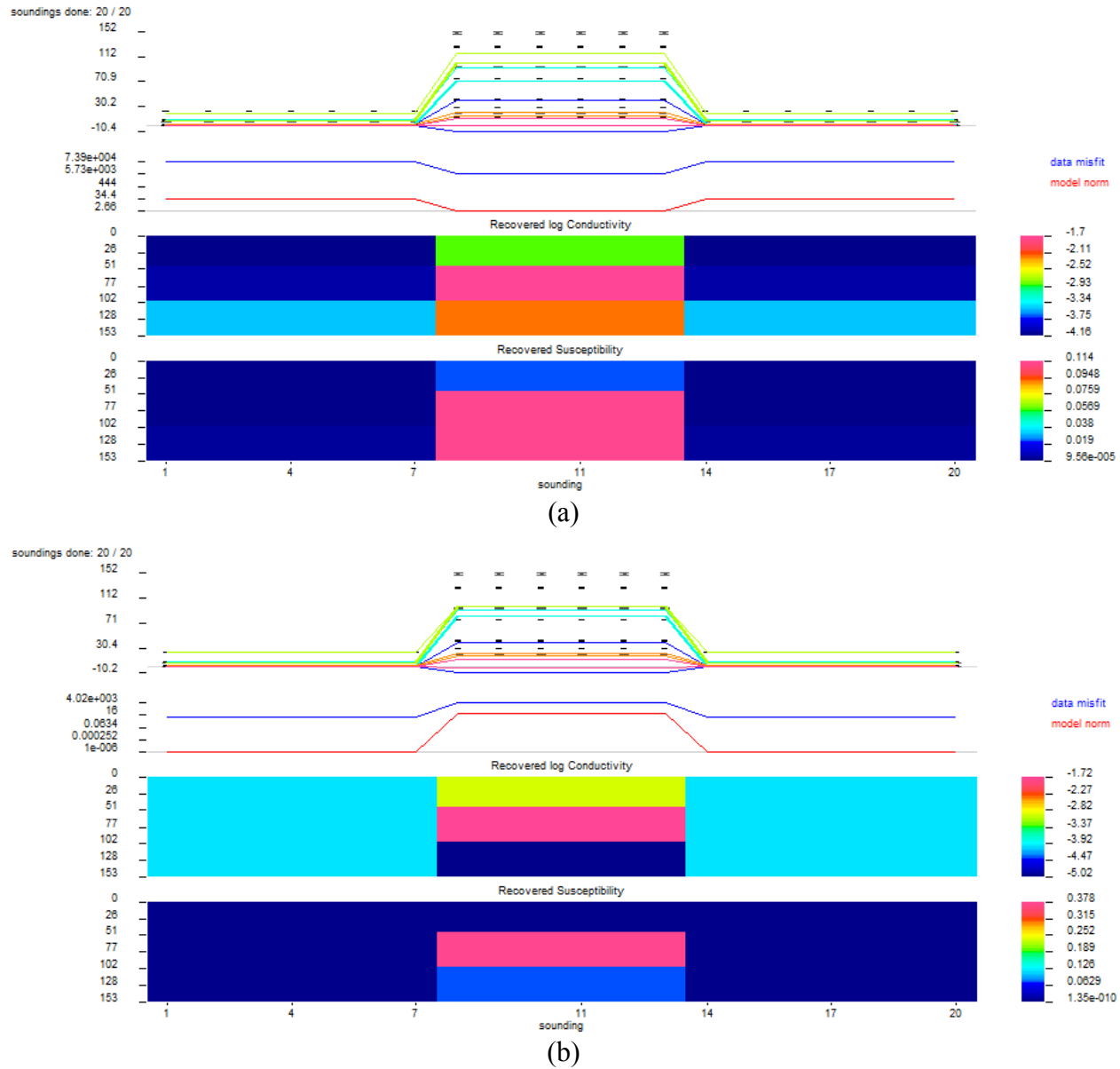
Figure 4.4: Inversion result of the semi-infinite prim model using EM1DFM software and synthetic data (top) and 20 recovered 1D models of conductivity and susceptibility concatenated into a 2D cross section under the survey line. True model: a vertical semi-infinite prism at 20m depth, embedded in a homogeneous medium. Conductivity and susceptibility of the prism are 0.01 S/m and 0.1 SI units respectively, and conductivity and susceptibility of the background are 0.0001 S/m and 0 SI units. The reference models are a homogeneous half space of conductivity and susceptibility (a) 0.01 S/m and 0.1 SI units and (b) 0.0001 S/m and 0.0 SI units respectively.

Figure 4.3a shows that the values of estimated conductivity and susceptibility are near the true model values. Figure 4.3b shows that the values of estimated conductivity are near the true model values; the values of estimated susceptibility of second layer and basement are reduced. Figure 4.4a shows that the values of conductivity and susceptibility of the first layer are overestimated; the values of basement conductivity are underestimated. Figure 4.4b shows that the values of conductivity and susceptibility of the first layer are overestimated; the values of basement conductivity and susceptibility are underestimated.

From the above results we see that the EM inversion of conductivity and susceptibility is unstable. The estimated models of susceptibility using inversion are dependent on reference models and the resulting model parameters are underestimated as the depth increases, so depth and thickness are incorrectly estimated.

The main purpose of "EM1DFM" is to recover a good conductivity model unaffected by susceptibility effects in the EM data, so it is rather hard to get a good susceptibility model. Basically, the EM data are mostly sensitive to the conductivity and are only slightly sensitive to susceptibility, because the susceptibility in EM data is a second-order effect that can be detected only at low induction number (e.g. low frequency).

Although there are some problems with this code and the depth and thickness are incorrectly estimated, the magnetic anomaly appears. Therefore, the susceptibility value can be estimated using EM inversion.

4.3 Conclusion

In this chapter, I present the relationship between the total and remanent magnetizations. According to the equation, the RM cannot be estimated from TM directly. The RM is non-unique when the magnitude of IM or Königsberger ratio is unknown. The magnetic susceptibility is the parameter needed to determine the magnitude of IM.

EM inversion is one of the most useful techniques to obtain the susceptibility due to its relatively low cost and high sensitivity. The susceptibility models of the synthetic examples are obtained using the "EM1DFM" software to prove the feasibility of this method. Even if, it is hard to get a good susceptibility model in EM data, because susceptibility is such as a second-order effect.

The susceptibility models recovered by inversion depend on reference conductivity and susceptibility models and are weakly sensitive to the thickness and depth, because the responses of high frequency are not sensitive to the deep conductivities and susceptibilities. Fortunately, most of kimberlite pipes are consider as a semi-finite vertical pipe so that the thickness is unnecessary, and the purpose of EM inversion is to determine the susceptibility that can be recovered. Therefore, EM method is a viable method to obtain the susceptibility. Certainly, the inversion code used has some problems and improvements could be done.

For instance, the purpose of the algorithm can be changed that to recover a good susceptibility model, because the purpose of "EM1DFM" is to recover a good conductivity model unaffected by susceptibility effects in the EM data. Thus, The algorithm of EM inversion can use a reference model and weightings, and the susceptibility to be only in certain depth ranges in the model.

CHAPTER 5   TESTS AND APPLICATIONS

The purpose of this chapter is to test the inversion algorithm and illustrate the advantages and utility of joint inversion of magnetic field and analytic signal. In the first case, all model responses of total-field magnetic data and its analytic signal are contaminated with Gaussian noise. In the second case, the model responses are contaminated with Gaussian noise and a residual regional noise. The third case consists of model responses generated by two pipes with anomalies interfering with each other and contaminated with Gaussian noise. The final case is a field example used to illustrate the utility of joint inversion of magnetic field and analytic signal for exploration.

5.1   Tests

In this section, I will test the sensitivity of joint inversion of magnetic field and analytic signal in presence of typical noises. In order to highlight the futures of joint inversion of magnetic field and analytic signal, the magnetic field inversion and analytic signal inversion are shown in each model respectively. These inversion techniques are similar to the joint inversion (based on Gauss-Newton method using the singular value decomposition and Marquardt's factor).

I present semi-infinite vertical cylinder models to simulate the kimberlite pipes. The geomagnetic field is identical for each model: amplitude 57,000nT, inclination and declination are 74˚ and -12˚. The survey region is 1,000m by 1,000m and is sampled with 41 by 41 receiver points (1681 receivers); the distance between two receivers is 25m. The number of iterations is 30, the initial damping factor is 1 and the initial trade off parameter is 0.5. When the data misfit of magnetic field and analytic signal is less than 10^{-6}, the inversion is stopped.

5.1.1 Gaussian noise

In this section, the magnetic data for each model are contaminated with Gaussian noise whose standard deviation is 50nT. The analytic signal is calculated from the resulting magnetic data and filtered by low-pass filters. When the Gaussian noise is present, the total-field magnetic data are not smooth. The analytic signal is very sensitive to the irregular data that cause some large anomaly. So I use the low-pass filters to filter the analytic signal that can reduce the noise in the high-frequency spectrum.

For each model, there are two figures to present the inversion results. The first figure displays the 2D color image of the model data and results of joint inversion of magnetic field and analytic signal, X-axes is directed to the east and Y-axes is directed to the north: (a) modeled total-field magnetic anomaly without noise, (b) modeled total field magnetic anomaly with noise, (c) total magnetic field response to the inverted model computed using joint inversion, (d) total magnetic field response of the inverted model computed using magnetic field inversion only, (e) modeled analytic signal without noise, (f) modeled analytic signal with noise, (g) analytic signal response to the inverted model computed using joint inversion, (h) analytic signal response to the inverted model computed using analytic signal inversion only.

The second companion figure displays convergence plots: (a) data misfits, (b) parameter changes, (c) trade-off parameter, and (d) damping factor. The green circle solid lines represent joint inversion, the blue fork solid lines represent magnetic field inversion only, the red point solid lines represent analytic signal inversion only.

The first model is a semi-infinite vertical cylinder with a diameter of 248m, centered in the survey area and located at a depth of 69m. The TM amplitude is $J_{tot} = 768nT$, and inclination and declination of TM are $I_{tot} = 69^o$ and $D_{tot} = -19^o$. Table 5.1 shows that for the joint inversion of total magnetic field and analytic signal (JIMA), the results clearly recover the model parameters for the model; for the magnetic field inversion (MFI) only, the results clearly recover the model parameters for the model; for the only analytic signal inversion (ASI), the recovered parameters are biased from their true value.

Table 5.1: Model 1 (a vertical cylinder at an intermediate depth with an inclination and a declination close to the geomagnetic inclination and declination contaminated with 50nT Gaussian noise): joint inversion of magnetic field and analytic signal (JIMA), magnetic field inversion (MFI) and analytic signal inversion (ASI).

	Mag.(nT)	In.(°)	De.(°)	X.(m)	Y.(m)	Dia.(m)	Dep.(m)
Model	768	69	-19	500	500	248	69
Initial	100	45	-45	300	300	140	150
JIMA	766.63	69.68	-20.46	499.20	498.84	248.64	69.61
MFI	761.19	69.86	-20.58	499.22	498.60	248.79	69.15
ASI	996.36	68.16	2.37	504.57	502.96	248.43	87.60

(a)

(e)

Figure 5.1: Model 1 (a vertical cylinder at an intermediate depth with an inclination and a declination close to the geomagnetic inclination and declination contaminated with 50nT Gaussian noise): 2D contours of the models and inversion results.

Figure 5.1: Model 1 (a vertical cylinder at an intermediate depth with an inclination and a declination close to the geomagnetic inclination and declination contaminated with 50nT Gaussian noise): 2D contours of the models and inversion results (continue).

(a)

(b)

(c)

(d)

Figure 5.2: Model 1 (a vertical cylinder at an intermediate depth with an inclination and a declination close to the geomagnetic inclination and declination contaminated with 50nT Gaussian noise): convergence plots.

The second model is a semi-infinite vertical cylinder with a diameter of 248m, centered in the survey area and located at a depth of 69m. The TM amplitude is $J_{tot} = 768nT$, and TM inclination and declination are $I_{tot} = -22^o$ and $D_{tot} = 47^o$. Table 5.2 shows that for the joint inversion of total magnetic field and analytic signal (JIMA), the results clearly recover the model parameters; for the magnetic field inversion (MFI) only, the results clearly recover the model parameters; for the analytic signal inversion (ASI) only, the recover parameters are biased from their true value.

Table 5.2: Model 2 (a vertical cylinder at an intermediate depth with an inclination and a declination differing from the geomagnetic inclination and declination contaminated with 50nT Gaussian noise): joint inversion of magnetic field and analytic signal (JIMA), magnetic field inversion (MFI) and analytic signal inversion (ASI).

	Mag.(nT)	In.(°)	De.(°)	X.(m)	Y.(m)	Dia.(m)	Dep.(m)
Model	768	-22	47	500	500	248	69
Initial	100	-45	15	300	300	140	150
JIMA	776.13	-21.75	47.48	499.56	500.47	248.75	69.27
MFI	764.04	-21.94	47.50	499.67	500.89	248.36	68.21
ASI	1195.07	-17.03	47.33	499.81	500.78	248.01	94.61
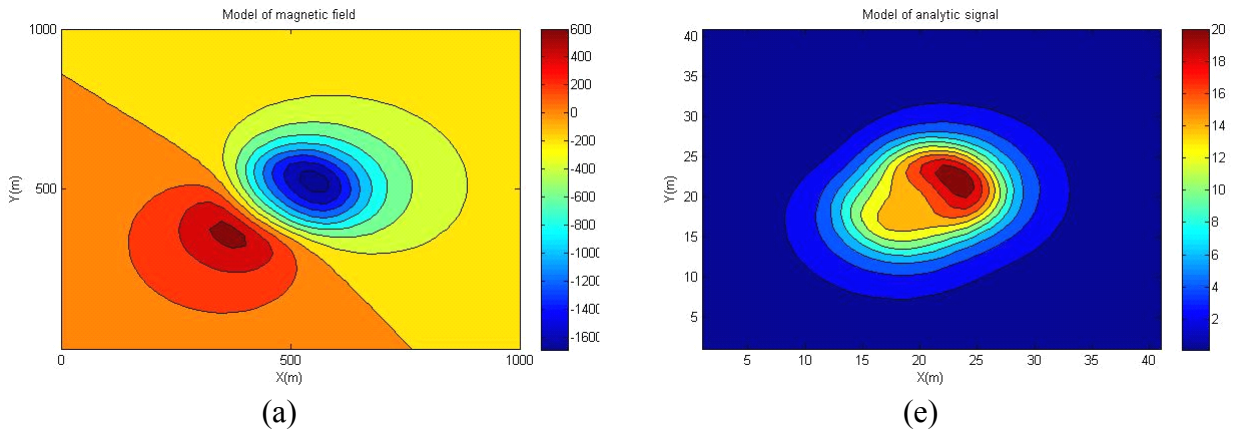
(a)   (e)

Figure 5.3: Model 2 (a vertical cylinder at an intermediate depth with an inclination and a declination differing from the geomagnetic inclination and declination contaminated with 50nT Gaussian noise): 2D contours of the models and inversion results.

(b)

(f)

(c)

(g)

(d)

(h)
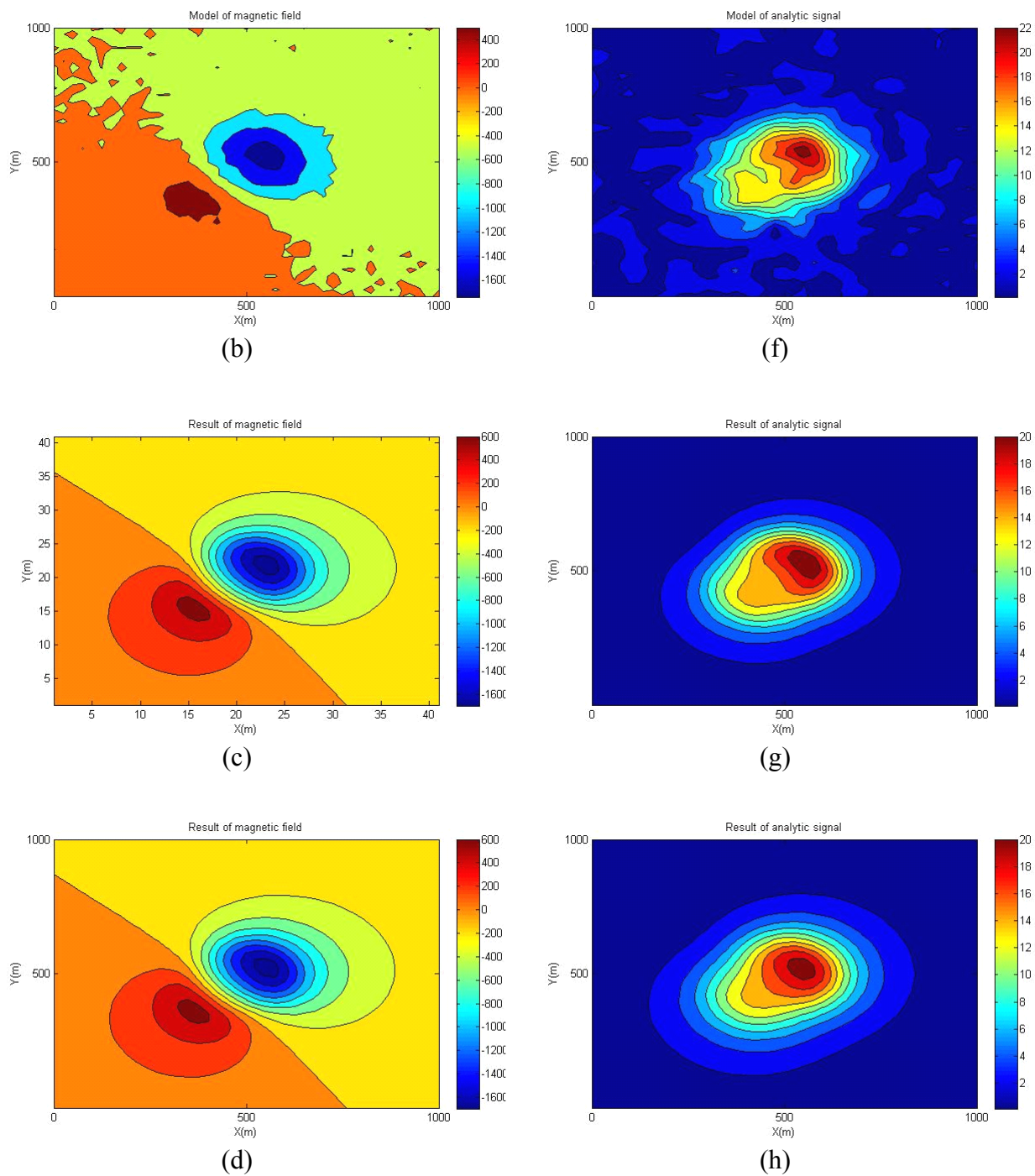
Figure 5.3: Model 2 (a vertical cylinder at an intermediate depth with an inclination and a declination differing from the geomagnetic inclination and declination contaminated with 50nT Gaussian noise): 2D contours of the models and inversion results (continue).
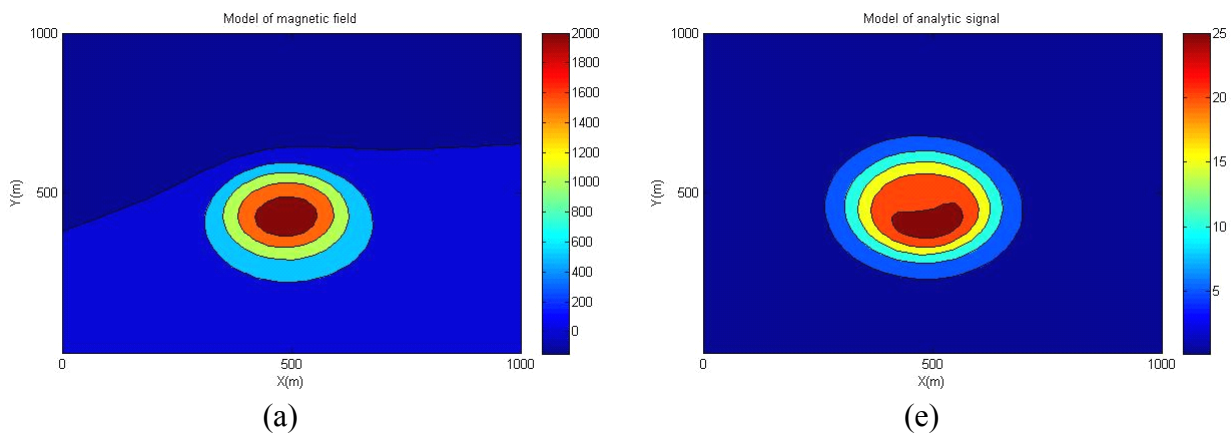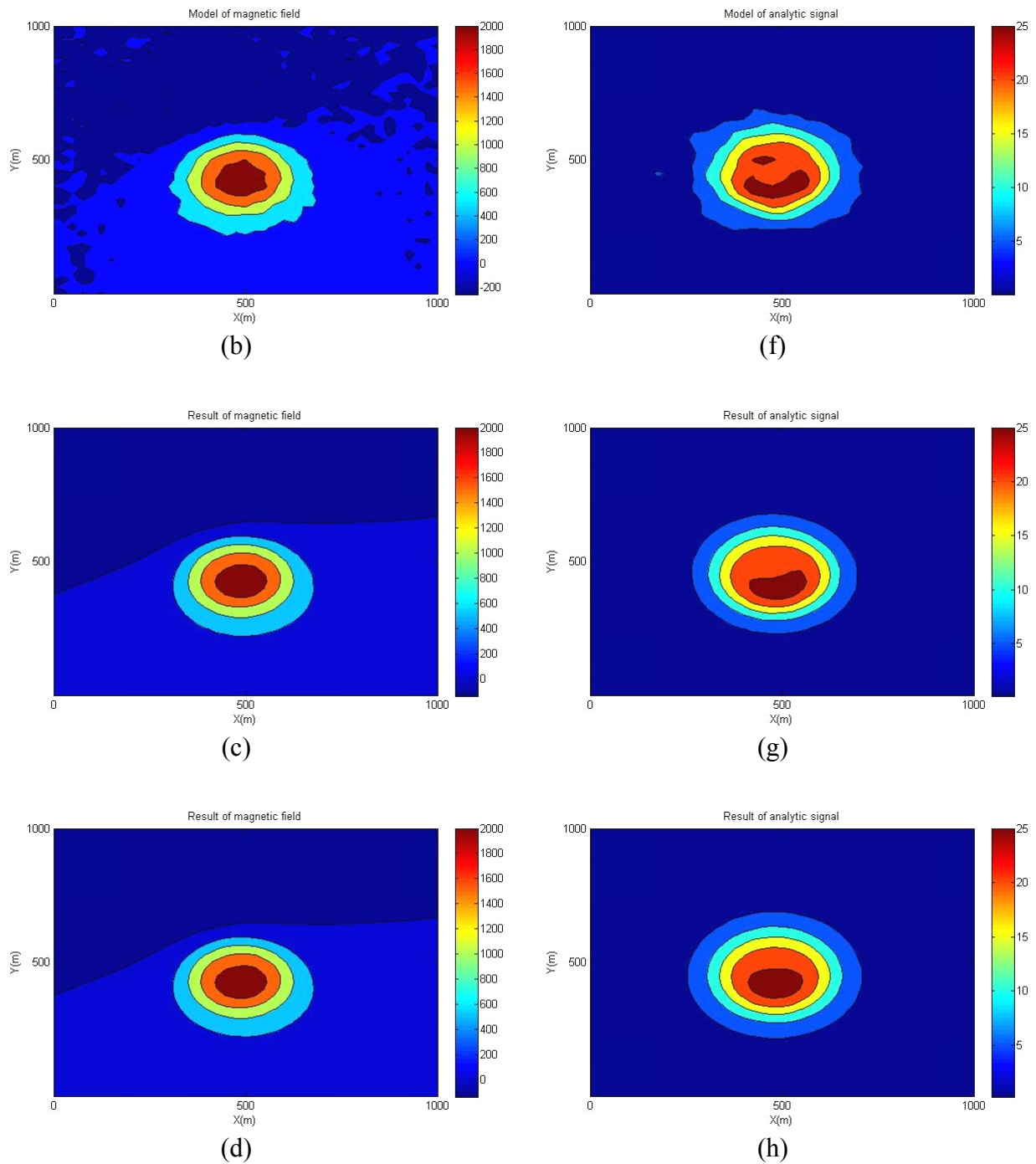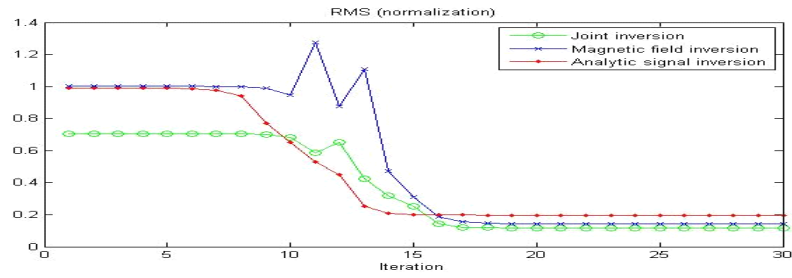
(a)
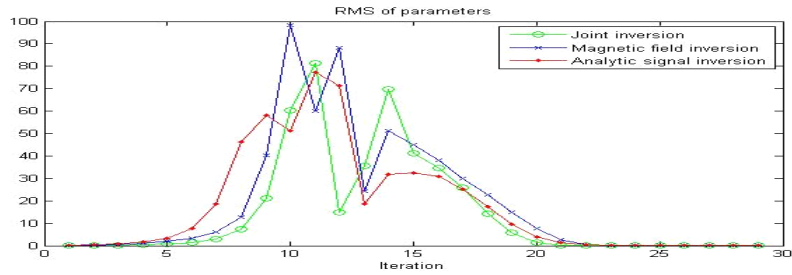
(b)
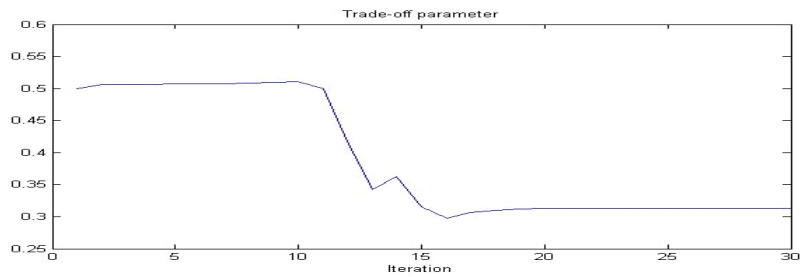
(c)
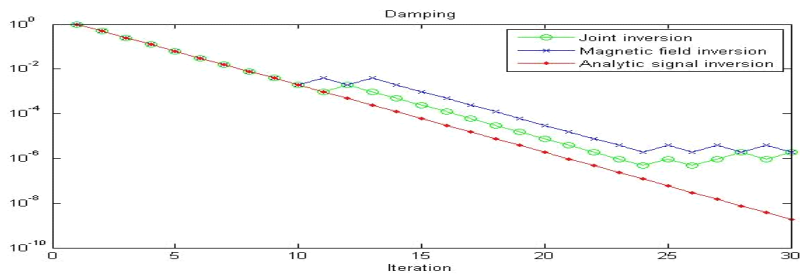
(d)

Figure 5.4: Model 2 (a vertical cylinder at an intermediate depth with an inclination and a declination differing from the geomagnetic inclination and declination contaminated with 50nT Gaussian noise): convergence plots.

The third model is a semi-infinite vertical cylinder with a diameter of 334m, centered in the survey area and located at a depth of 26m. The TM amplitude is $J_{tot} = 289nT$, and TM inclination and declination are $I_{tot} = 143^o$ and $D_{tot} = -31^o$. Table 5.3 shows that for the joint inversion of total magnetic field and analytic signal (JIMA), the results clearly recover the model parameters; for the magnetic field inversion (MFI) only, the results clearly recover the model parameters; for the analytic signal inversion (ASI) only, the recover parameters are biased from their true value.

Table 5.3: Model 3 (a shallow large diameter vertical cylinder with an inclination and a declination differing from the geomagnetic inclination and declination contaminated with 50nT Gaussian noise): joint inversion of magnetic field and analytic signal (JIMA), magnetic field inversion (MFI) and analytic signal inversion (ASI).

	Mag.(nT)	In.(°)	De.(°)	X.(m)	Y.(m)	Dia.(m)	Dep.(m)
Model	289	143	-31	500	500	334	26
Initial	1000	90	0	300	300	140	100
JIMA	292.76	143.68	-31.20	500.20	499.13	332.01	26.46
MFI	291.34	143.34	-31.20	500.11	499.33	331.15	26.19
ASI	340.25	147.81	-31.50	500.73	498.86	334.95	32.36
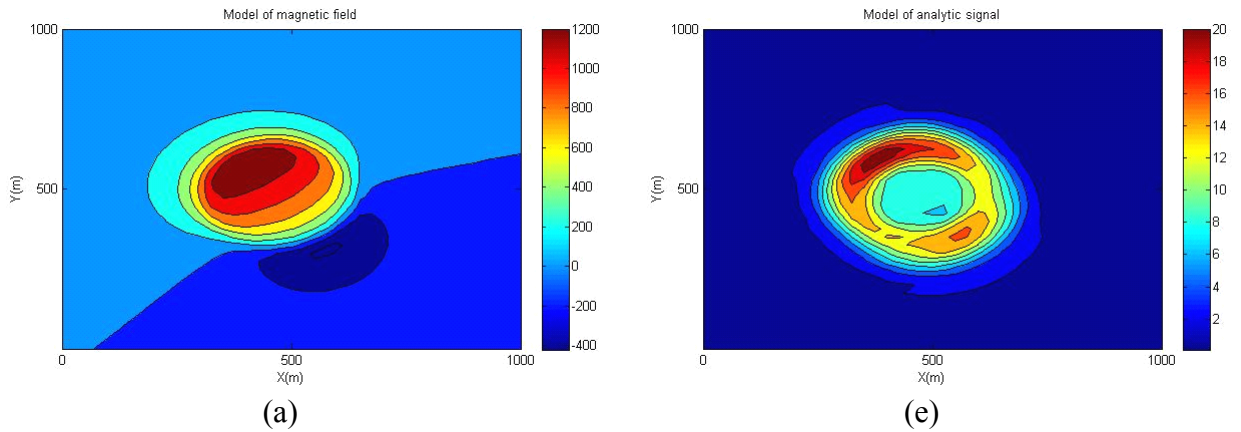
(a)   (e)

Figure 5.5: Model 3 (a shallow large diameter vertical cylinder with an inclination and a declination differing from the geomagnetic inclination and declination contaminated with 50nT Gaussian noise): 2D contours of the models and inversion results.
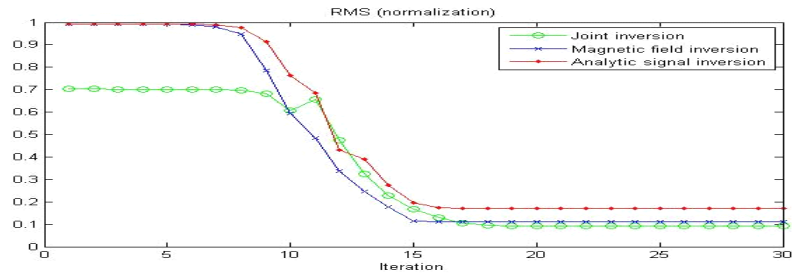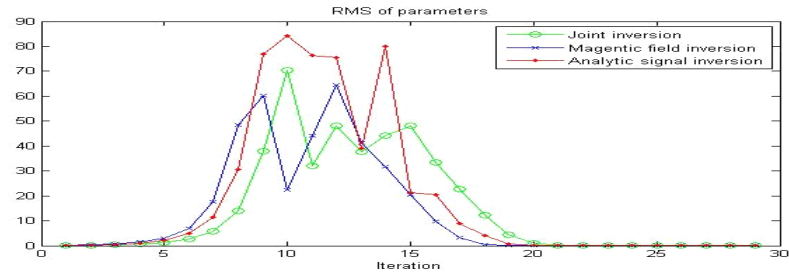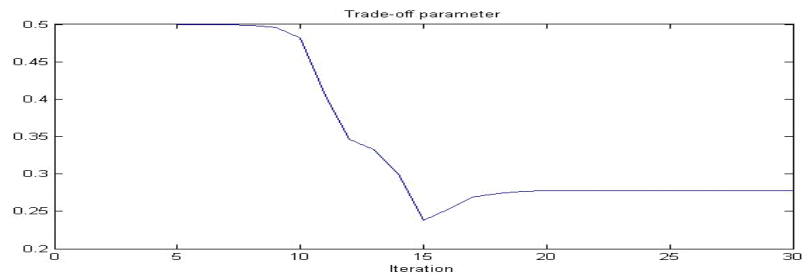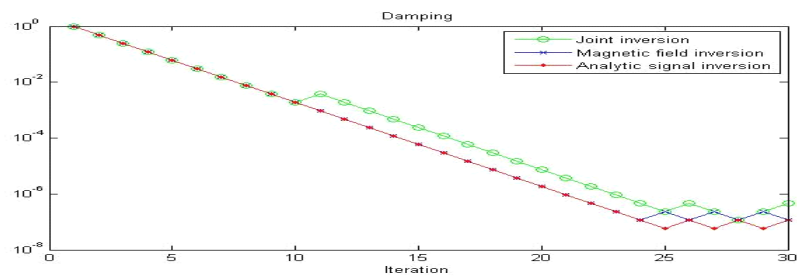
(b)

(f)

(c)

(g)

(d)

(h)

Figure 5.5: Model 3 (a shallow large diameter vertical cylinder with an inclination and a declination differing from the geomagnetic inclination and declination contaminated with 50nT Gaussian noise): 2D contours of the models and inversion results (continue).

(a)

(b)

(c)

(d)

Figure 5.6: Model 3 (a shallow large diameter vertical cylinder with an inclination and a declination differing from the geomagnetic inclination and declination contaminated with 50nT Gaussian noise): convergence plots.

The fourth model is a semi-infinite vertical cylinder with a diameter of 154m, centered in the survey area and located at a depth of 163m. The TM amplitude, inclination and declination are $J_{tot} = 2488nT$, $I_{tot} = 83^o$ and $D_{tot} = -8^o$. Table 5.4 shows that for the joint inversion of total magnetic field and analytic signal (JIMA), the results clearly recover the model parameters; for the magnetic field inversion (MFI) only, the results clearly recover the model parameters; for the only analytic signal inversion (ASI), the recovered parameters are far from their true value.

Table 5.4: Model 4 (a deep small diameter vertical cylinder similar to a vertical monopole with an inclination and a declination close to the geomagnetic inclination and declination contaminated with 50nT Gaussian noise): joint inversion of magnetic field and analytic signal (JIMA), magnetic field inversion (MFI) and analytic signal inversion (ASI).

	Mag.(nT)	In.(°)	De.(°)	X.(m)	Y.(m)	Dia.(m)	Dep.(m)
Model	2488	83	-8	500	500	154	163
Initial	200	45	-45	300	300	320	60
JIMA	2214.19	82.27	-12.06	498.09	500.81	163.11	160.74
MFI	2301.87	82.62	-12.92	497.95	500.03	159.64	160.94
ASI	5925.32	28.28	11.56	509.25	544.93	126.34	182.4798
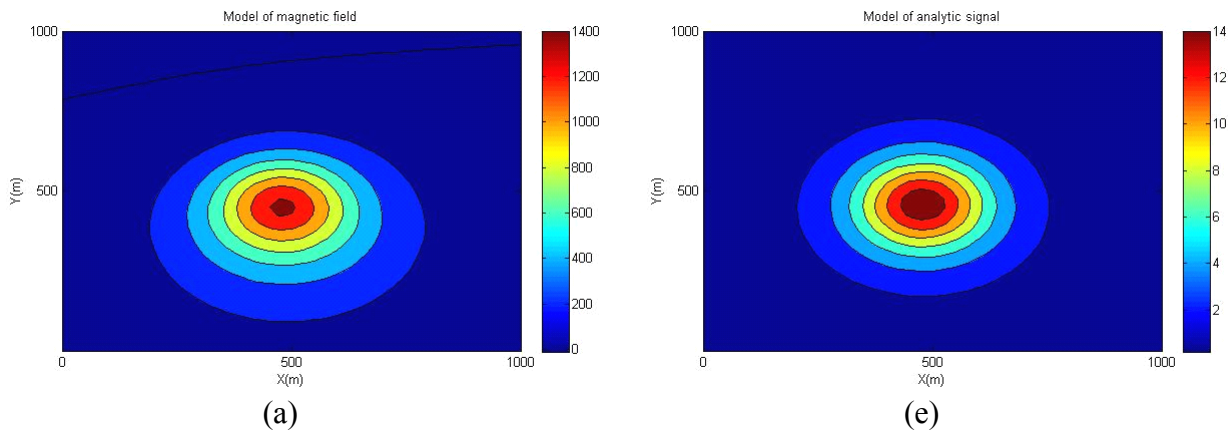
(a)   (e)

Figure 5.7: Model 4 (a deep small diameter vertical cylinder similar to a vertical monopole with an inclination and a declination close to the geomagnetic inclination and declination contaminated with 50nT Gaussian noise): 2D contours of the models and inversion results.

(b)

(f)

(c)

(g)

(d)

(h)
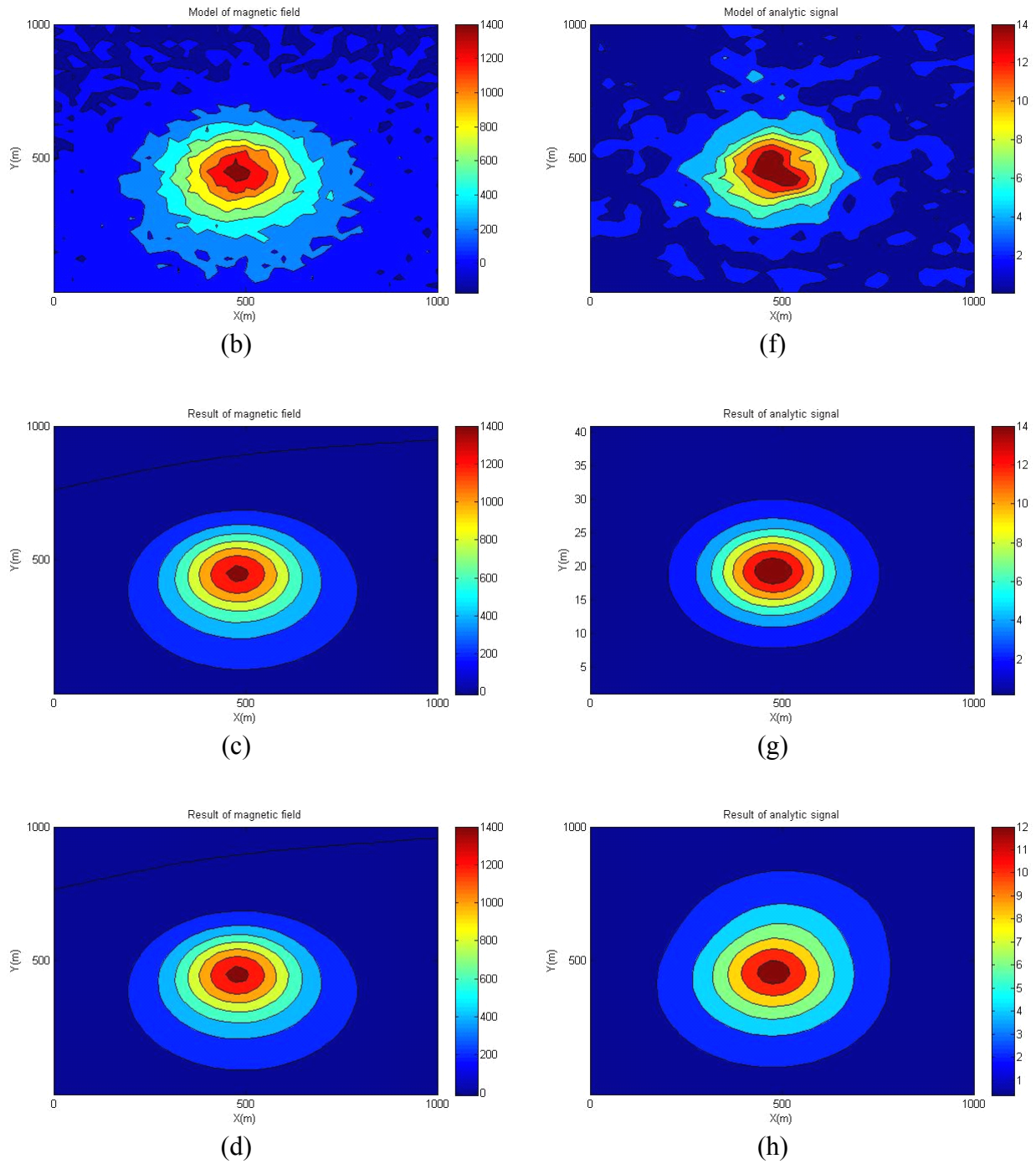
Figure 5.7: Model 4 (a deep small diameter vertical cylinder similar to a vertical monopole with an inclination and a declination close to the geomagnetic inclination and declination contaminated with 50nT Gaussian noise): 2D contours of the models and inversion results (continue).
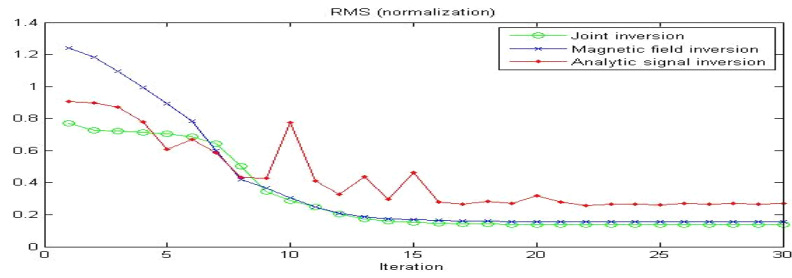
(a)
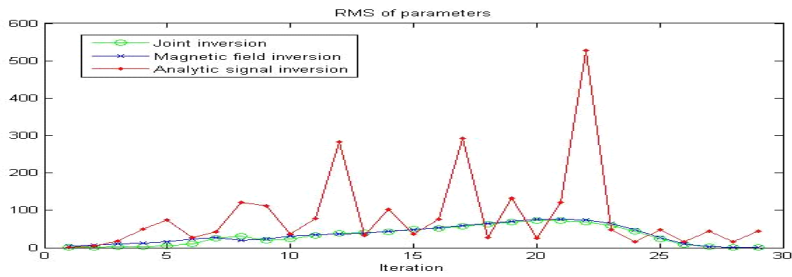
(b)
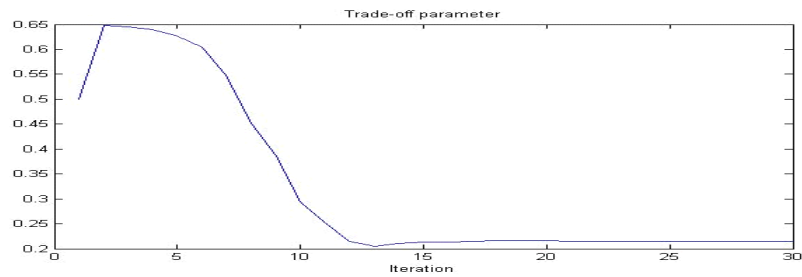
(c)

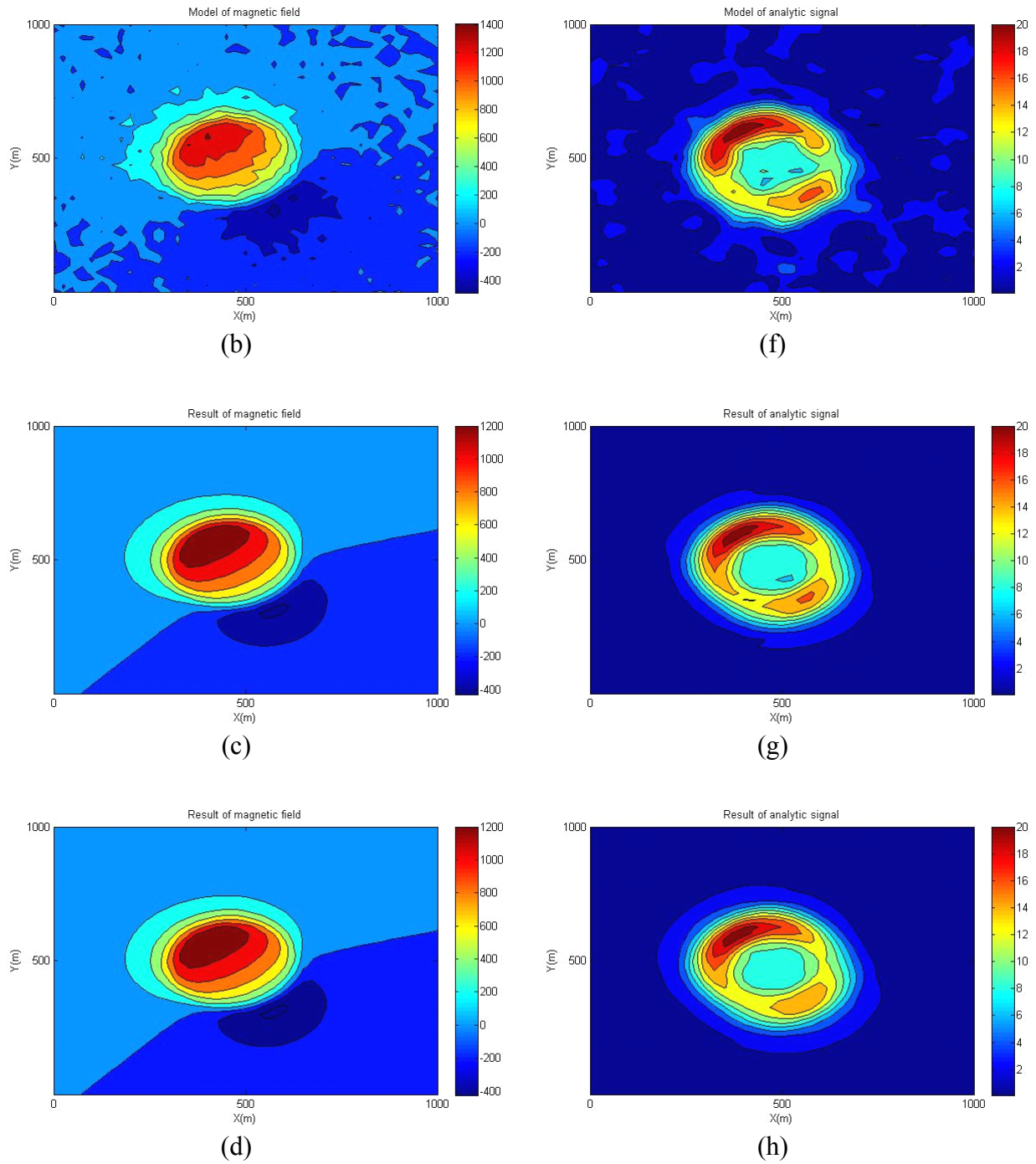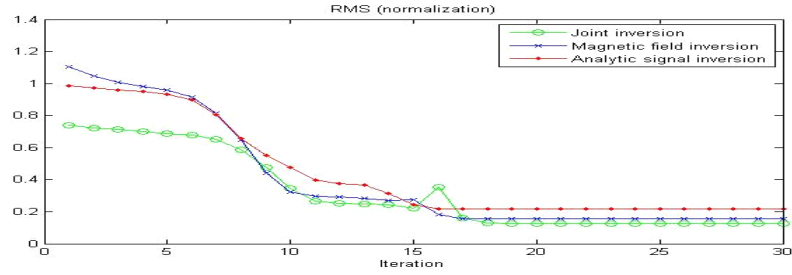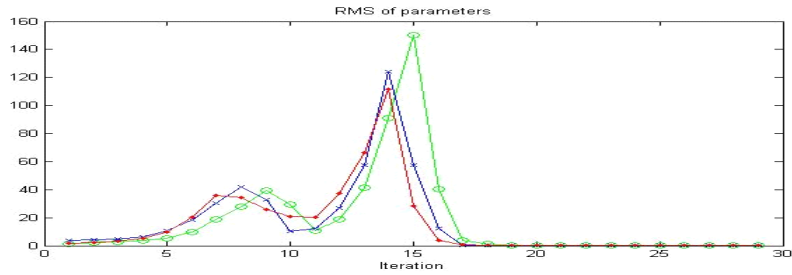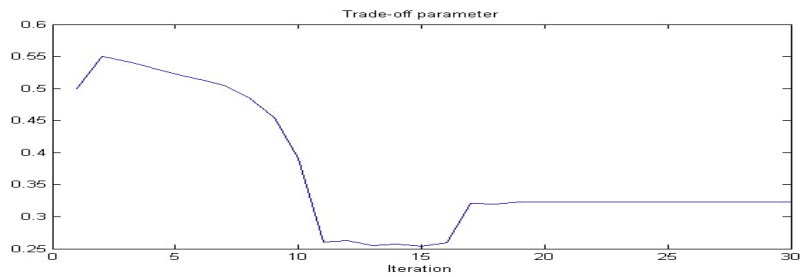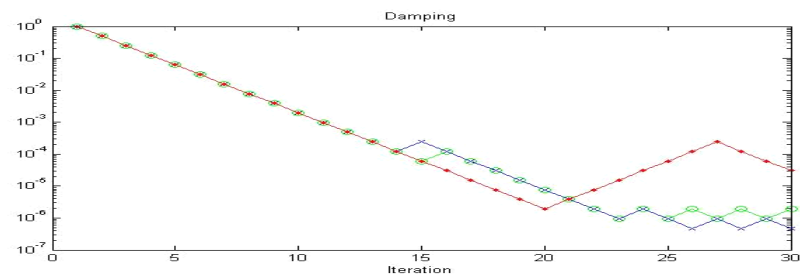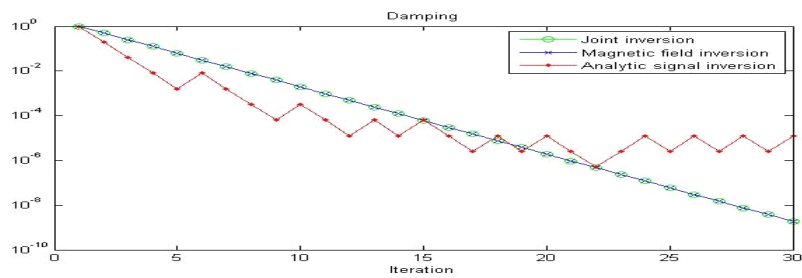
(d)

Figure 5.8: Model 4 (a deep small diameter vertical cylinder similar to a vertical monopole with an inclination and a declination close to the geomagnetic inclination and declination contaminated with 50nT Gaussian noise): convergence plots.

From the tables and figures above, joint inversion of magnetic field and analytic signal clearly recovers the model parameters for each model, for arbitrary initial parameters. The convergence curves for the inversion for each model are asymptotic to zero. Therefore, the algorithm of joint inversion of magnetic field and analytic signal is stable and the results accurate.

Comparing the individual magnetic field inversion and analytic signal inversion, the magnetic field inversion is more stable and accurate than analytic signal inversion especially for model 4. Comparing the results of four models with Gaussian noise, individual parameters are sensitive to Gaussian noise in different models. For the model with large TM inclination, the amplitude and declination of TM and depth of cylinder are sensitive to Gaussian noise; for the model with small TM inclination, the TM inclination is sensitive to Gaussian noise; for the shallow model, the TM amplitude and diameter are sensitive to Gaussian noise; for the deep model, the TM amplitude, diameter and depth of cylinder are sensitive to Gaussian noise.

Model 4 is a deep and small diameter cylinder similar to a monopole. Figure 5.8 shows that the data misfit and parameter changes computed using analytic signal only are not asymptotic to a minimum, so the analytic signal inversion is unstable and convergence is not reached. The analytic signal enhances the responses caused by shallow sources and reduces the responses caused by deep sources; in addition to the reduction of long wavelength anomalies, the analytic signal is a high-pass filter and therefore there is an increase of the short-wavelength Gaussian noise. When the cylinder is deep it can be modeled as a magnetic monopole and in that case neither the TM nor the diameter of the cylindrical pipe can be resolved but only the product of the TM by the section area ($\sim a^2$). Therefore, the results of analytic signal inversion is non-unique causing the algorithm to be unstable and inaccurate,the data misfit still being very small.

5.1.2 Regional noise

In this section, the responses of magnetic data of each model are contaminated with 20nT Gaussian noise plus a plane regional showing a gradient of 0-500nT from east to west. The plane regional may represent the result of an incomplete regional-residual separation of the total magnetic field anomaly. In a first step, the mean of the total anomaly is subtracted from the data. The analytic signal is calculated from the resulting magnetic data and filtered using low pass filters.

For each model, there are two figures to present the result of inversion. The first figure displays 2D color map of model responses and results of joint inversion of magnetic field and analytic signal, X-axes is directed to the east and Y-axes is directed to the north: (a) modeled total-field magnetic anomaly without noise, (b) modeled total field magnetic anomaly with noise, (c) total magnetic field response to the inverted model computed using joint inversion, (d) total magnetic field response of the inverted model computed using magnetic field inversion, (e) modeled analytic signal without noise, (f) modeled analytic signal with noise, (g) analytic signal response of the inverted model computed using joint inversion, (h) analytic signal response of the inverted model computed using analytic signal inversion.

The second companion figure displays the convergence plots: (a) data misfits, (b) parameter changes, (c) trade-off parameter, and (d) damping factor. The green circle solid lines represent joint inversion, the blue fork solid lines represent magnetic field inversion, the red point solid lines represent analytic signal inversion.

The fifth model is a semi-infinite vertical cylinder with a diameter of 248m, centered in the survey area and located at a depth of 69m. The TM amplitude, inclination and declination are $J_{tot} = 768nT$, $I_{tot} = 69^o$ and $D_{tot} = -19^o$. Table 5.5 shows that for the joint inversion of total magnetic field and analytic signal (JIMA), the results clearly recover the model parameters; for the magnetic field inversion (MFI) only, the recovered parameters are biased from their true value; for the analytic signal inversion (ASI) only, the results clearly recover the model parameters for the model.

Table 5.5: Model 5 (a vertical cylinder at an intermediate depth with an inclination and a declination close to the geomagnetic inclination and declination contaminated with 20nT Gaussian noise plus a plane regional): joint inversion of magnetic field and analytic signal (JIMA), magnetic field inversion (MFI) and analytic signal inversion (ASI).

	Mag.(nT)	In.(°)	De.(°)	X.(m)	Y.(m)	Dia.(m)	Dep.(m)
Model	768	69	-19	500	500	248	69
Initial	100	45	-45	300	300	140	150
JIMA	921.94	61.46	-32.64	501.11	503.49	244.65	78.54
MFI	2173.88	25.59	-69.69	423.15	510.35	202.69	117.01
ASI	921.72	61.86	-31.05	501.66	503.58	244.86	78.68

(a)   (e)

Figure 5.9: Model 5 (a vertical cylinder at an intermediate depth with an inclination and a declination close to the geomagnetic inclination and declination contaminated with 20nT Gaussian noise plus a plane regional): 2D contours of the models and inversion results.

(b)

(f)

(c)

(g)

(d)

(h)

Figure 5.9: Model 5 (a vertical cylinder at an intermediate depth with an inclination and a declination close to the geomagnetic inclination and declination contaminated with 20nT Gaussian noise plus a plane regional): 2D contours of the models and inversion results (continue).

(a)

(b)

(c)

(d)

Figure 5.10: Model 5 (a vertical cylinder at an intermediate depth with an inclination and a declination close to the geomagnetic inclination and declination contaminated with 20nT Gaussian noise plus a plane regional): convergence plots.

The sixth model is a semi-infinite vertical cylinder with a diameter of 248m, centered in the survey area and located at a depth of 69m. The TM amplitude, inclination and declination are $J_{tot} = 768nT$, $I_{tot} = -22^o$ and $D_{tot} = 47^o$. Table 5.6 shows that for the joint inversion of total magnetic field and analytic signal (JIMA), the results clearly recover the model parameters; for the magnetic field inversion (MFI) only, the recovered parameters are biased from their true value; for the analytic signal inversion (ASI) only, the results clearly recover the model parameters.

Table 5.6: Model 6 (a vertical cylinder at an intermediate depth with an inclination and a declination differing from the geomagnetic inclination and declination contaminated with 20nT Gaussian noise plus a plane regional): joint inversion of magnetic field and analytic signal (JIMA), magnetic field inversion (MFI) and analytic signal inversion (ASI).

	Mag.(nT)	In.(°)	De.(°)	X.(m)	Y.(m)	Dia.(m)	Dep.(m)
Model	768	-22	47	500	500	248	69
Initial	300	-45	30	300	300	200	100
JIMA	823.29	-26.03	36.97	496.01	493.01	256.55	76.64
MFI	398.34	-37.81	-5.89	566.50	500.93	259.12	40.79
ASI	824.43	-26.17	38.12	495.88	502.96	256.79	76.85
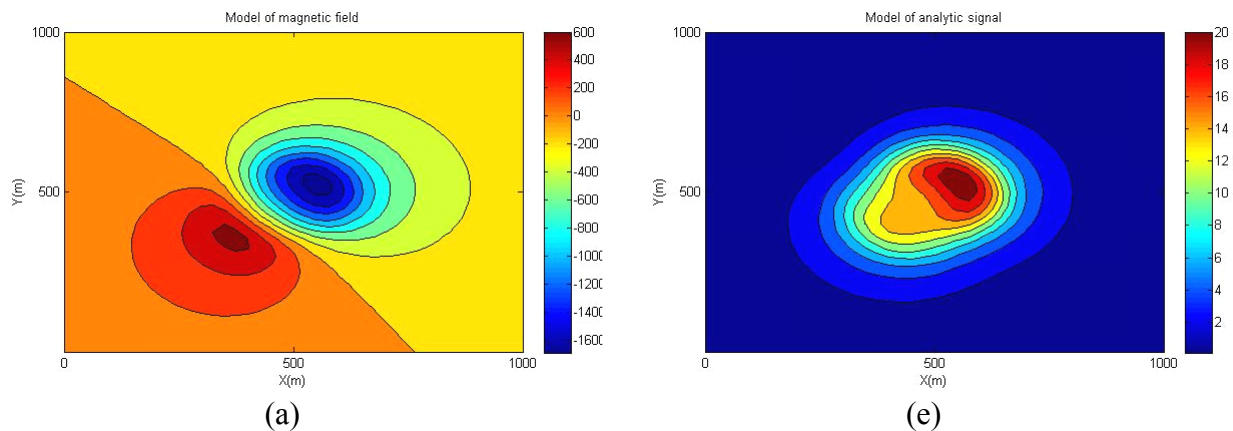
(a)   (e)

Figure 5.11: Model 6 (a vertical cylinder at an intermediate depth with an inclination and a declination differing from the geomagnetic inclination and declination contaminated with 20nT Gaussian noise plus a plane regional): 2D contours of the models and inversion results.

Figure 5.11: Model 6 (a vertical cylinder at an intermediate depth with an inclination and a declination differing from the geomagnetic inclination and declination contaminated with 20nT Gaussian noise plus a plane regional): 2D contours of the models and inversion results (continue).
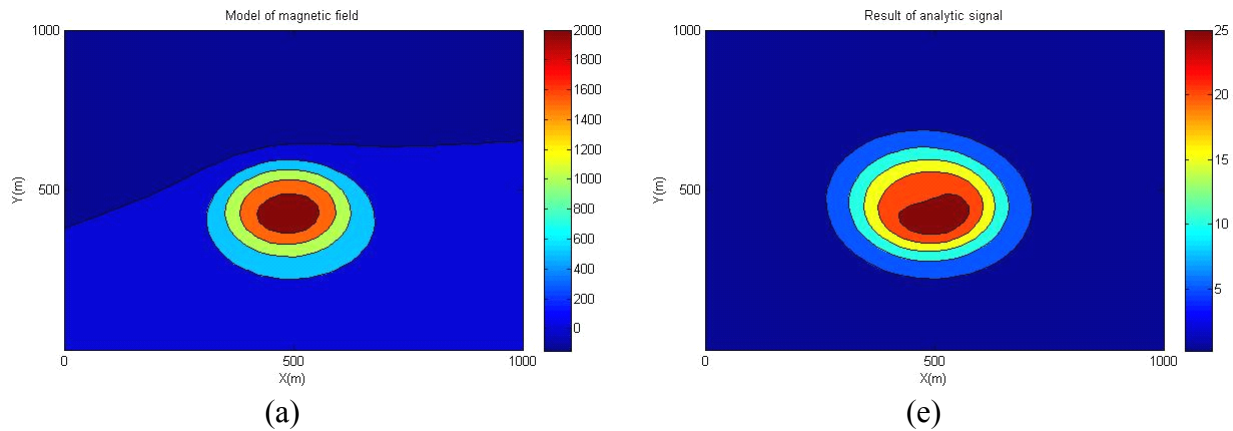
(a)

(b)
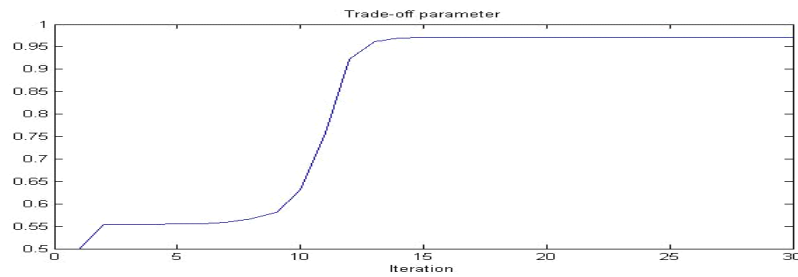
(c)
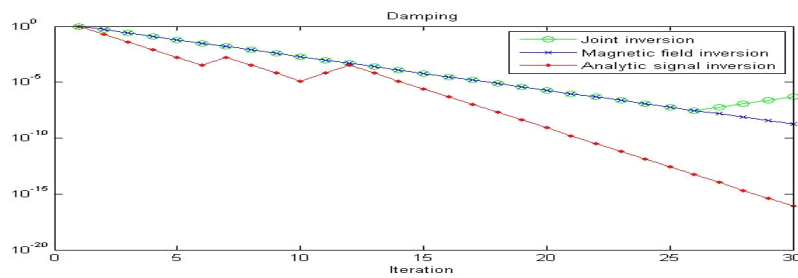
(d)

Figure 5.12: Model 6 (a vertical cylinder at an intermediate depth with an inclination and a declination differing from the geomagnetic inclination and declination contaminated with 20nT Gaussian noise plus a plane regional): convergence plots.

The seventh model is a semi-infinite vertical cylinder with a diameter of 334m, centered in the survey area and located at a depth of 26m. The TM amplitude, inclination and declination are $J_{tot} = 289nT$, $I_{tot} = 143^o$ and $D_{tot} = -31^o$. Table 5.7 shows that: for the joint inversion of total magnetic field and analytic signal (JIMA), the results clearly recover the model parameters for the model; for the magnetic field inversion (MFI) only, the recovered parameters are far from their true value; for the analytic signal inversion (ASI) only, the results clearly recover the model parameters for the model.

Table 5.7: Model 7 (a shallow large diameter vertical cylinder with an inclination and a declination differing from the geomagnetic inclination and declination contaminated with 20nT Gaussian noise plus a plane regional): joint inversion of magnetic field and analytic signal (JIMA), magnetic field inversion (MFI) and analytic signal inversion (ASI).

	Mag.(nT)	In.(˚)	De.(˚)	X.(m)	Y.(m)	Dia.(m)	Dep.(m)
Model	289	143	-31	500	500	334	26
Initial	500	120	-15	300	300	200	50
JIMA	309.86	141.63	-23.22	501.53	499.67	337.01	29.22
MFI	528.08	156.22	71.53	367.08	545.53	302.31	77.18
ASI	310.36	141.67	-23.57	501.57	499.69	336.05	29.28
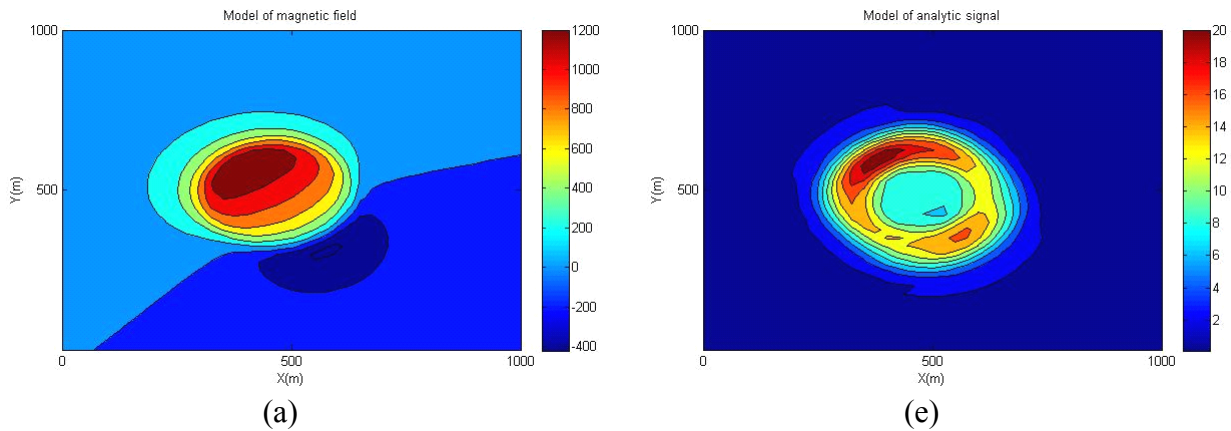
(a)   (e)

Figure 5.13: Model 7 (a shallow large diameter vertical cylinder with an inclination and a declination differing from the geomagnetic inclination and declination contaminated with 20nT Gaussian noise plus a plane regional): 2D contours of the models and inversion results.
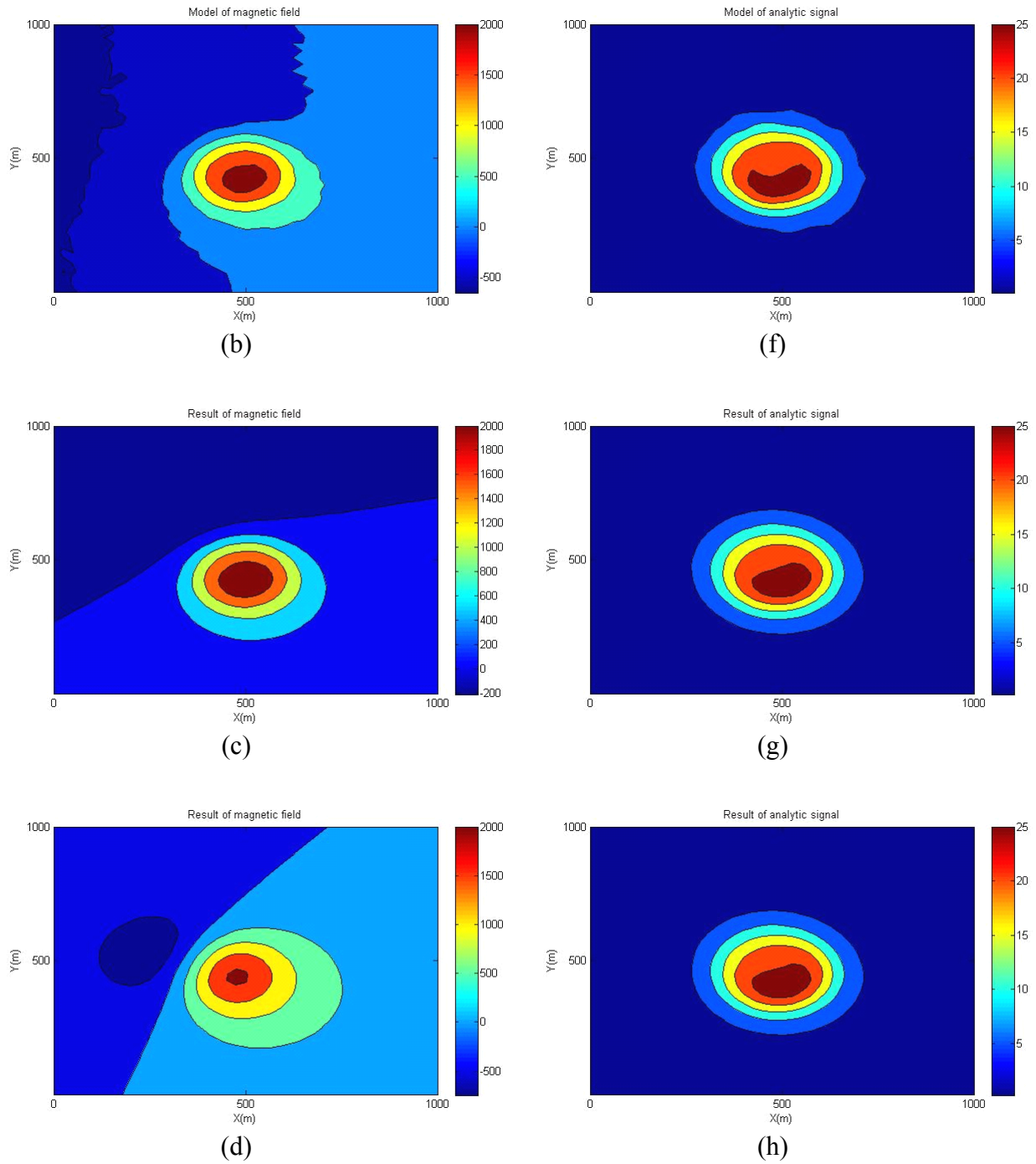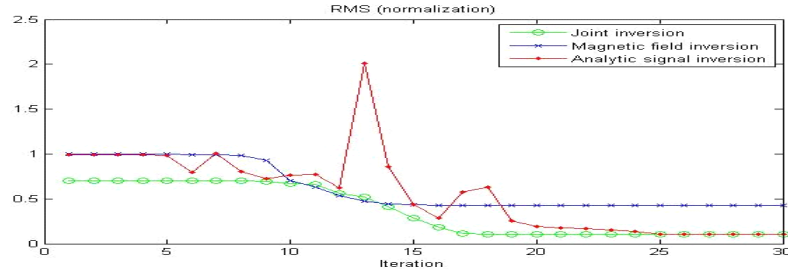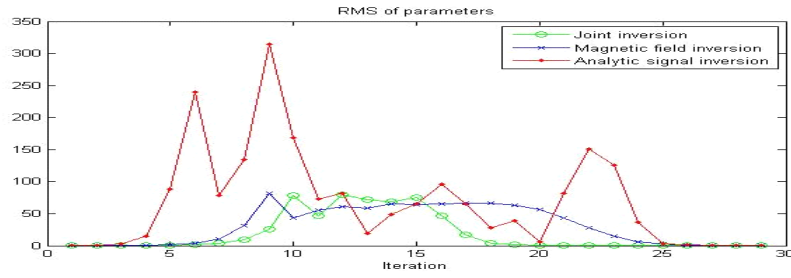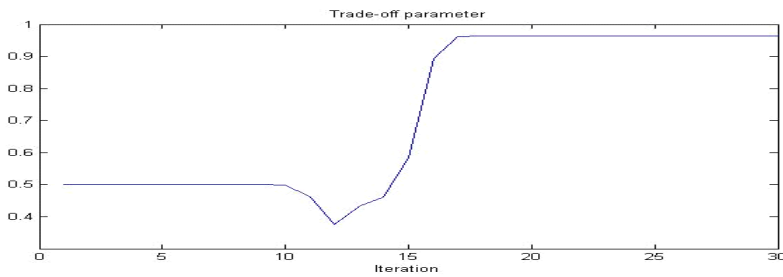
(b)

(f)

(c)

(g)

(d)

(h)
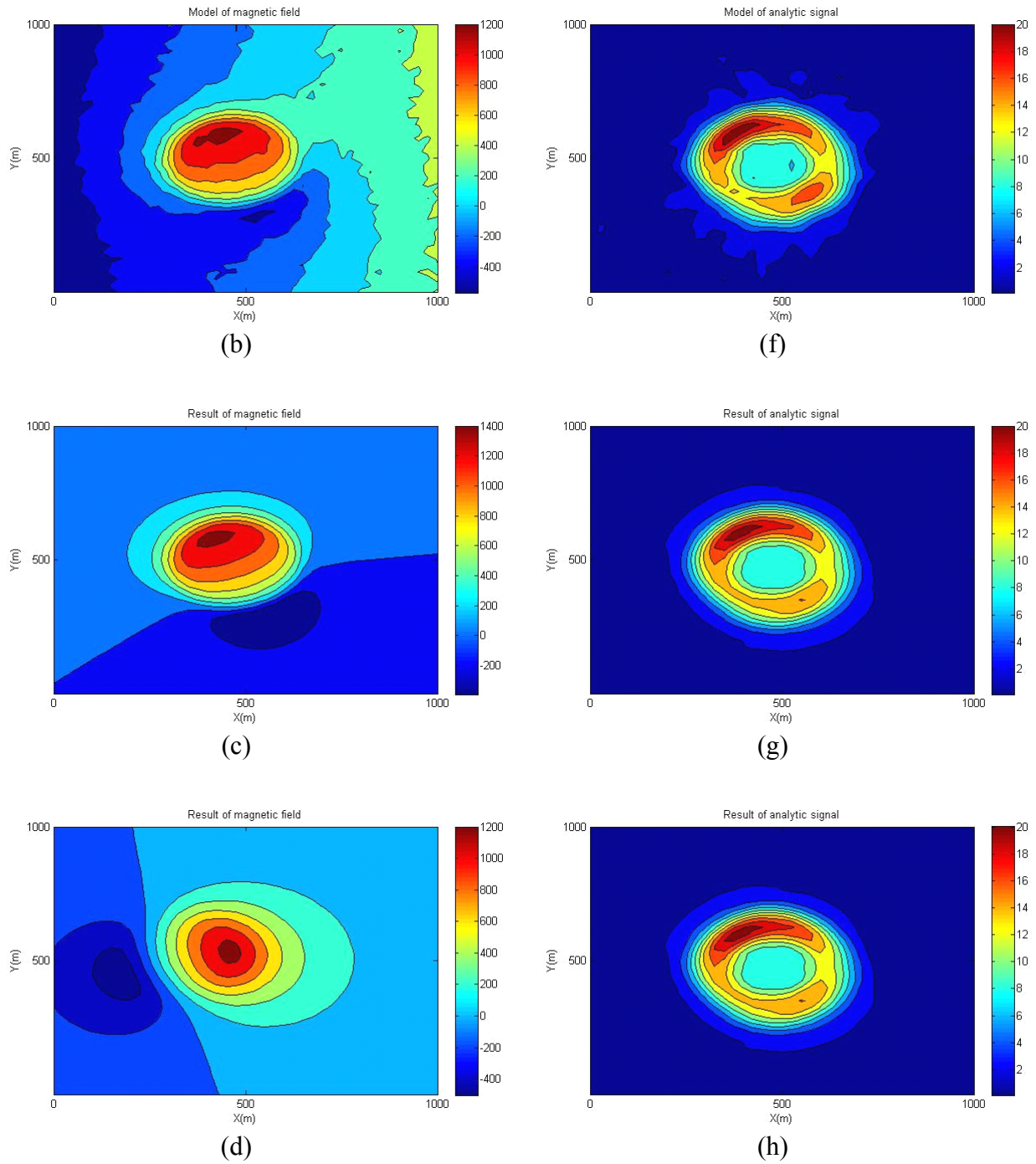
Figure 5.13: Model 7 (a shallow large diameter vertical cylinder with an inclination and a declination differing from the geomagnetic inclination and declination contaminated with 20nT Gaussian noise plus a plane regional): 2D contours of the models and inversion results (continue).
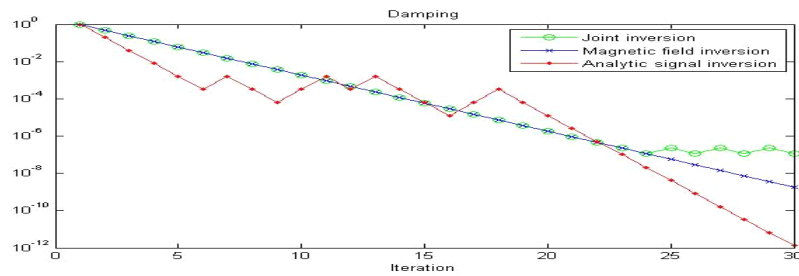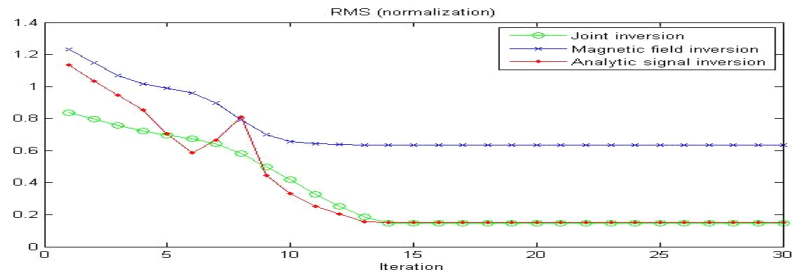
(a)
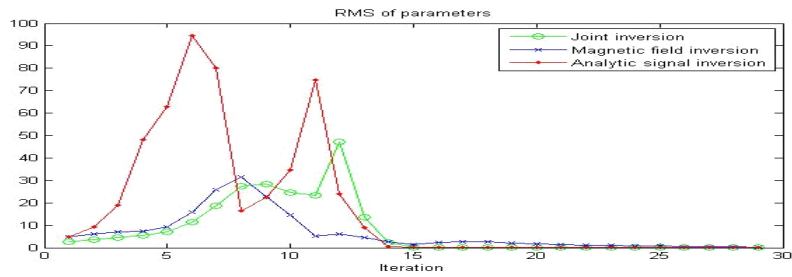
(b)
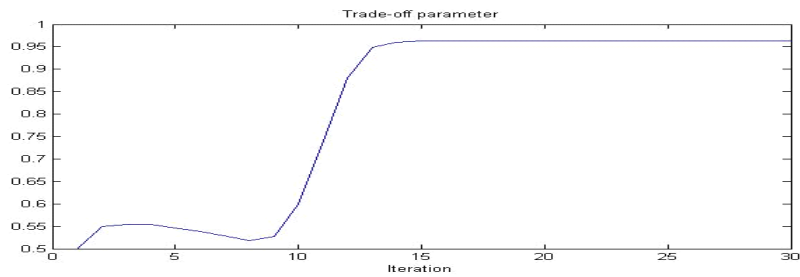
(c)
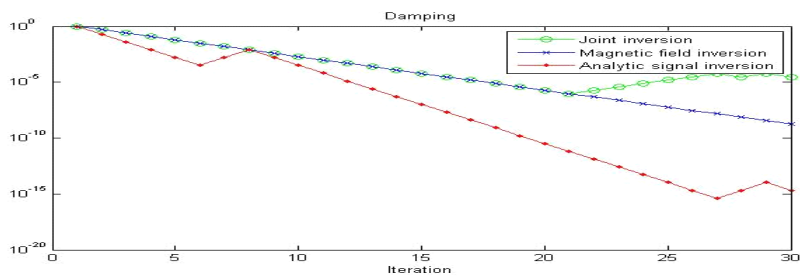
(d)

Figure 5.14: Model 7 (a shallow large diameter vertical cylinder with an inclination and a declination differing from the geomagnetic inclination and declination contaminated with 20nT Gaussian noise plus a plane regional): convergence plots.

The eighth model is a semi-infinite vertical cylinder with a diameter of 154m, centered in the survey area and located at a depth of 163m. The TM amplitude, inclination and declination are $J_{tot} = 2488nT$, $I_{tot} = 83^o$ and $D_{tot} = -8^o$. Table 5.8 shows that for the joint inversion of total magnetic field and analytic signal (JIMA), for the magnetic field inversion (MFI) and for the analytic signal inversion (ASI) respectively, the recovered parameters are far from their true value.

Table 5.8: Model 8 (a deep small diameter vertical cylinder similar to a vertical dipole with an inclination and a declination close to the geomagnetic inclination and declination contaminated with 20nT Gaussian noise plus a plane regional): joint inversion of magnetic field and analytic signal (JIMA), magnetic field inversion (MFI) and analytic signal inversion (ASI).

	Mag.(nT)	In.(°)	De.(°)	X.(m)	Y.(m)	Dia.(m)	Dep.(m)
Model	2488	83	-8	500	500	154	163
Initial	200	-45	-45	300	300	320	60
JIMA	8992.07	58.77	-51.40	487.94	511.54	89.33	180.02
MFI	654.40	33.05	-71.73	412.03	524.85	292.35	110.99
ASI	15927.11	55.69	-49.55	486.49	513.28	64.79	182.68
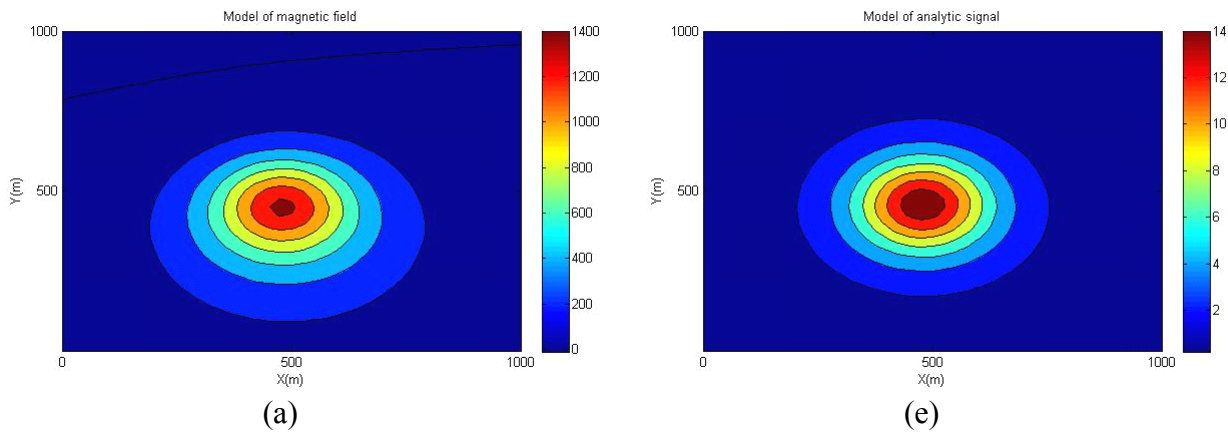
(a)   (e)

Figure 5.15: Model 8 (a deep small diameter vertical cylinder similar to a vertical dipole with an inclination and a declination close to the geomagnetic inclination and declination contaminated with 20nT Gaussian noise plus a plane regional): 2D contours of the models and inversion results.
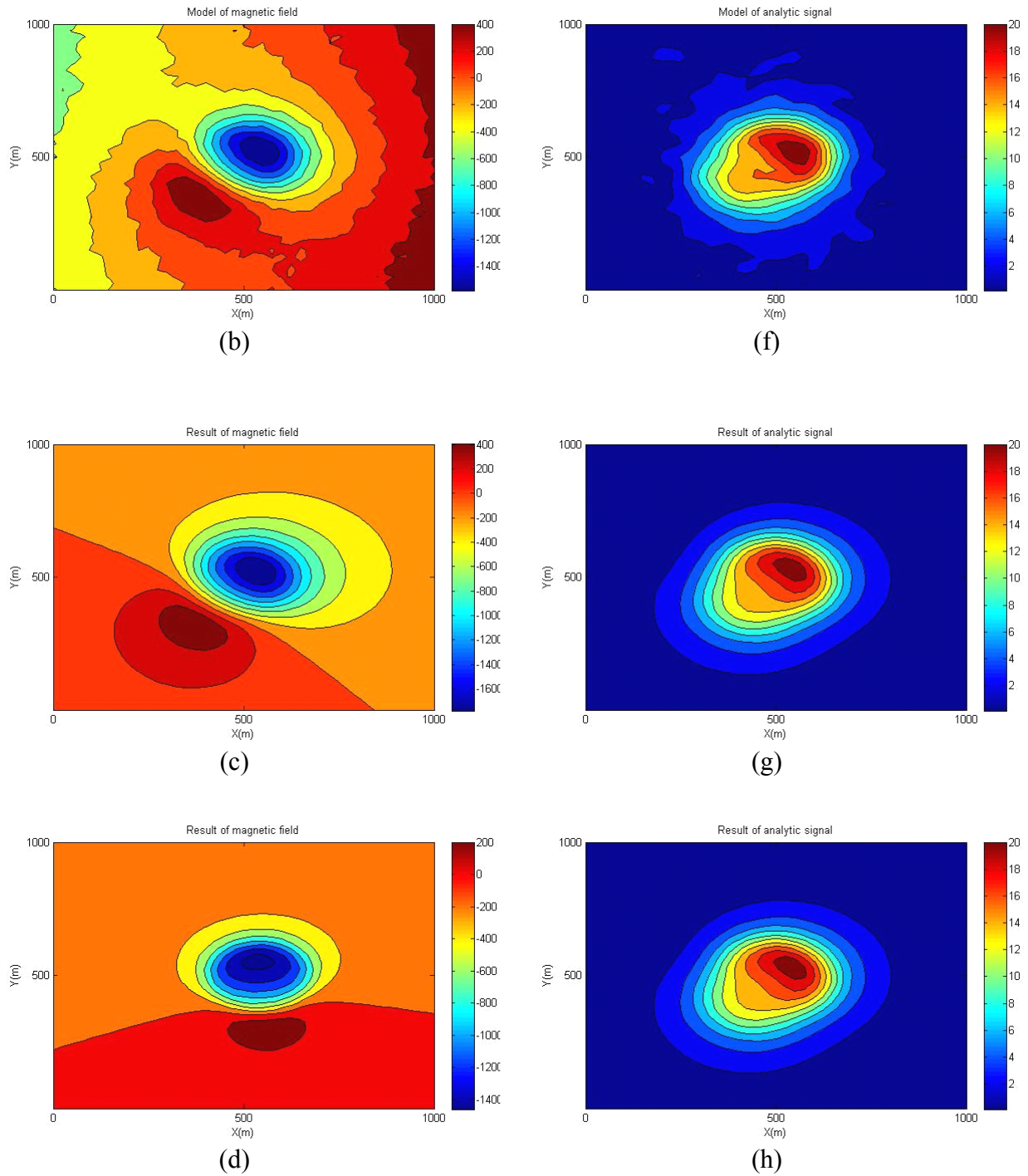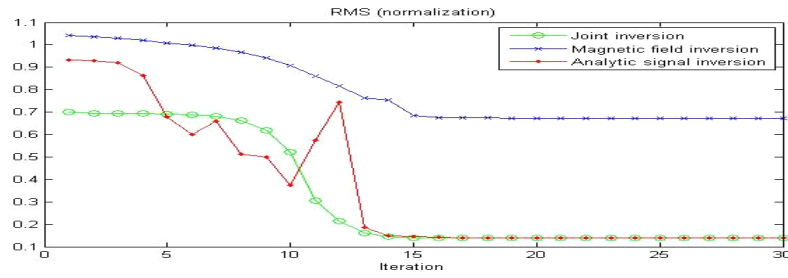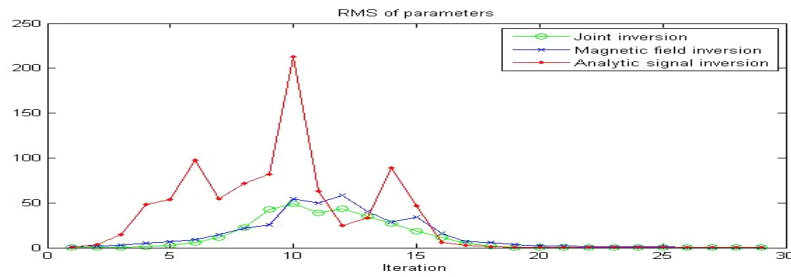
Figure 5.15: Model 8 (a deep small diameter vertical cylinder similar to a vertical dipole with an inclination and a declination close to the geomagnetic inclination and declination contaminated with 20nT Gaussian noise plus a plane regional): 2D contours of the models and inversion results (continue).

(a)

(b)

(c)

(d)

Figure 5.16: Model 8 (a deep small diameter vertical cylinder similar to a vertical dipole with an inclination and a declination close to the geomagnetic inclination and declination contaminated with 20nT Gaussian noise plus a plane regional): convergence plots.

From the tables and figures above, joint inversion of magnetic field and analytic signal clearly recovers the model parameters for each model, for arbitrary initial parameters. The convergence curves for the inversion for each model are asymptotic. Therefore, the algorithm of joint inversion of magnetic field and analytic signal is stable and accurate except for model 8.

Comparing the individual magnetic field inversion and analytic signal inversion, the analytic signal inversion is more stable and accurate than the magnetic field inversion except for model 8. The total-field magnetic data is more sensitive for a plane regional noise that can be considered as the deep or far from survey regional anomaly data. Comparing the results of four models, the results of the models with large TM inclination and deep depth are more affected by a plane regional plus Gaussian noise.

Model 8 is a deep and small diameter cylinder similar to a monopole. Figure 5.8 shows that the data misfit and parameter changes computed using analytic signal only or joint inversion do not converge to a minimum. The analytic signal inversion and joint inversion are unstable and convergence is not attained for this model.

As discussed above, the analytic signal inversion only is unstable and inaccurate for this model. Although the analytic signal inversion is unstable and inaccurate, the data misfit is still less than the single magnetic field inversion because the total-field magnetic data is more affected by the plane regional plus Gaussian noise. Therefore, the trade-off parameter is close to 1 and cannot constrain the inversion algorithm, causing instability and inaccuracy for this model.

5.1.3 Two pipes anomaly

In this section, the magnetic data are computed for two pipes contaminated with 20nT Gaussian noise. The first pipe is large cylinder considered as main anomaly, the second pipe is small cylinder considered as noise. The two pipes are adjacent with same magnetic properties and depth, and the size of pipe 2 is half of pipe. The analytic signal is calculated from these responses and low-pass filtered.

For each model, there are two figures to present the result of inversion. The first figure displays 2D contour about models and results of joint inversion of magnetic field and analytic signal, X-axes is directed to the east and Y-axes is directed to the north: (a) modeled total-field magnetic anomaly of pipe 1 without noise, (b) modeled total-field magnetic anomaly of pipe 2 without noise, (c) modeled total field magnetic anomaly of both pipes with noise, (d) total magnetic field response to the inverted model computed by joint inversion, (e) total magnetic field response to the inverted model computed by magnetic field inversion, (f) modeled analytic signal of pipe 1 without noise, (g) modeled analytic signal of pipe 2 without noise, (h) modeled analytic signal with noise, (i) analytic signal response to the inverted model computed by joint inversion, (j) analytic signal response to the inverted model computed by analytic signal inversion.

The second companion figure displays the convergence plots: (a) data misfits, (b) parameter changes, (c) trade-off parameter, and (d) damping factor. The green circle solid lines represent joint inversion, the blue fork solid lines represent magnetic field inversion, the red point solid lines represent analytic signal inversion.

The ninth model consists of two semi-infinite vertical cylinders with diameters of 248m and 124m respectively, located (400m, 500m) and (600m, 500m), at a depth of 69m. The TM is $J_{tot} = 768nT$, and directions of TM are-both $I_{tot} = 69^{o}$ and $D_{tot} = -19^{o}$. Table 5.9 shows that: for the joint inversion of total magnetic field and analytic signal (JIMA), the recovered parameters are biased from their true values (first pipe); for the only magnetic field inversion (MFI), the recover parameters are biased from their true values (first pipe); for the only analytic signal inversion (ASI), the recover parameters are far from their true values (first pipe).

Table 5.9: Model 9 (two vertical cylinders at an intermediate depth with an inclination and a declination close to the geomagnetic inclination and declination contaminated with 20nT Gaussian noise): joint inversion of magnetic field and analytic signal (JIMA), magnetic field inversion (MFI) and analytic signal inversion (ASI): joint inversion of magnetic field and analytic signal (JIMA), magnetic field inversion (MFI) and analytic signal inversion (ASI).

	Mag.(nT)	In.(˚)	De.(˚)	X.(m)	Y.(m)	Dia.(m)	Dep.(m)
Pipe 1	768	69	-19	400	500	248	69
Pipe 2	768	69	-19	600	500	124	69
Initial	1000	45	-45	300	300	140	150
JIMA	941.45	63.97	-27.14	418.98	507.06	265.33	84.53
MFI	968.61	64.38	-27.75	423.15	505.75	260.79	86.73
ASI	1197.79	27.30	76.30	461.79	500.26	254.31	80.54

(a)

(f)

(b)

(g)

(c)

(h)

Figure 5.17: Model 9 (two vertical cylinders at an intermediate depth with an inclination and a declination close to the geomagnetic inclination and declination contaminated with 20nT Gaussian noise): 2D contours of the models and inversion results.
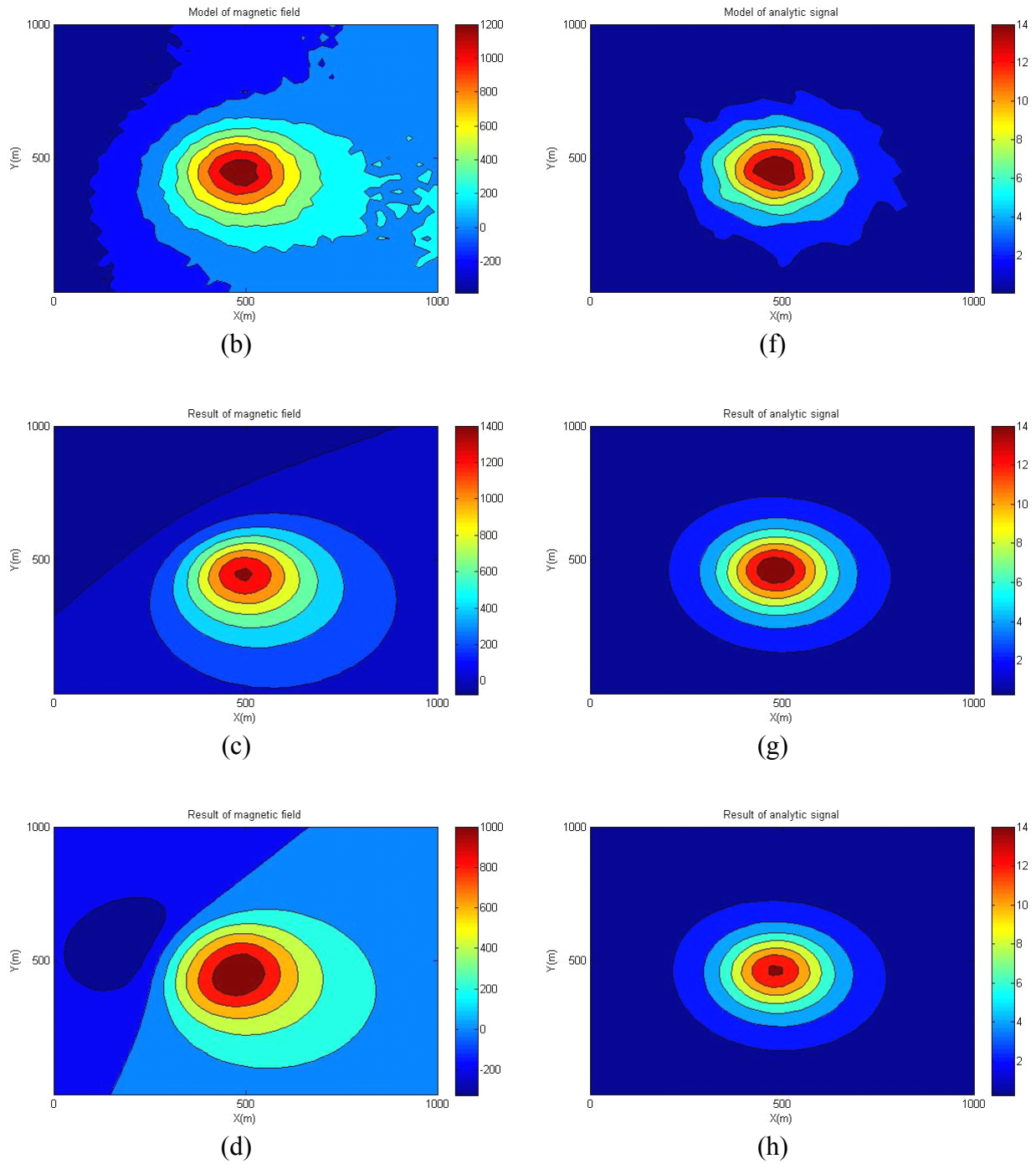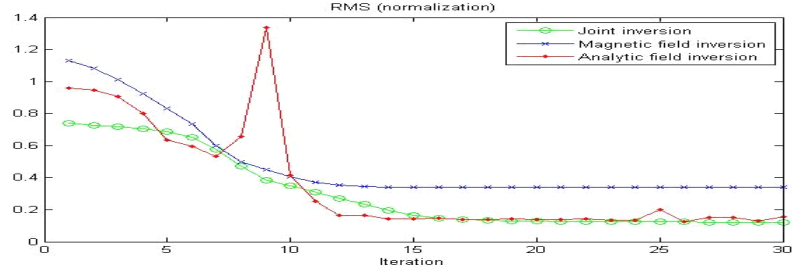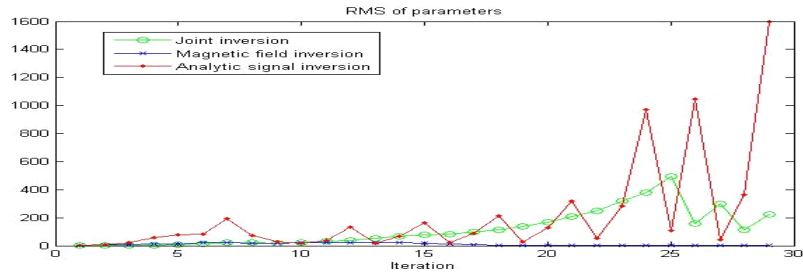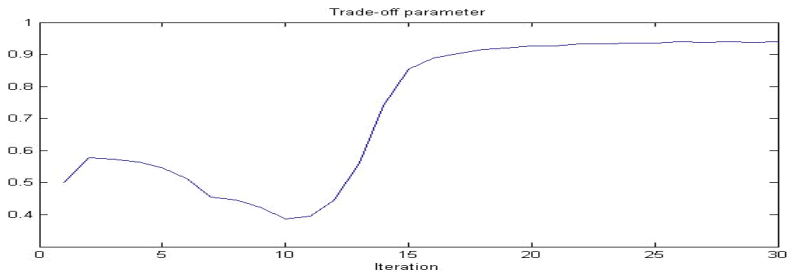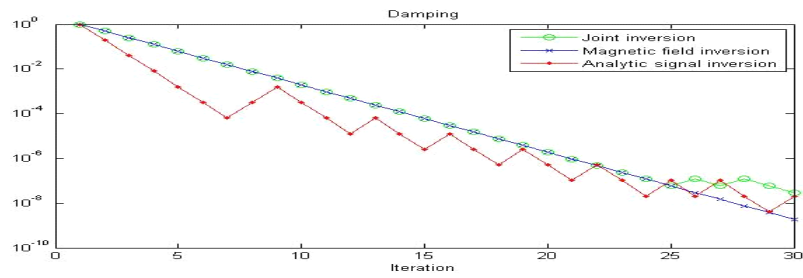
Figure 5.17: Model 9 (two vertical cylinders at an intermediate depth with an inclination and a declination close to the geomagnetic inclination and declination contaminated with 20nT Gaussian noise): 2D contours of the models and inversion results (continue).

(a)

(b)

(c)

(d)

Figure 5.18: Model 9 (two vertical cylinders at an intermediate depth with an inclination and a declination close to the geomagnetic inclination and declination contaminated with 20nT Gaussian noise): convergence plots.

The tenth model consists of two semi-infinite vertical cylinders with diameters of 248m and 124m respectively, located (400m, 500m) and (600m, 500m), at a depth of 69m. The amplitudes of TM is $J_{tot} = 768nT$, and directions of TM are-both $I_{tot} = -22^o$ and $D_{tot} = 47^o$. Table 5.10 shows that: for the joint inversion of total magnetic field and analytic signal (JIMA), the recover parameters are biased from their true values (first pipe); for the only magnetic field inversion (MFI), the recover parameters are biased from their true values (first pipe); for the only analytic signal inversion (ASI), the recover parameters are far from their true values (first pipe).

Table 5.10: Model 10 (two vertical cylinders at an intermediate depth with an inclination and a declination differing from the geomagnetic inclination and declination contaminated with 20nT Gaussian noise): joint inversion of magnetic field and analytic signal (JIMA), magnetic field inversion (MFI) and analytic signal inversion (ASI).

	Mag.(nT)	In.(˚)	De.(˚)	X.(m)	Y.(m)	Dia.(m)	Dep.(m)
Pipe 1	768	-22	47	400	500	248	69
Pipe 2	768	-22	47	600	500	124	69
Initial	1000	-45	30	300	300	200	100
JIMA	1218.52	-25.40	47.68	494.96	434.10	245.28	89.55
MFI	1170.99	-25.75	47.08	436.12	494.32	248.05	87.59
ASI	1697.15	-21.28	60.51	429.04	504.22	228.55	105.83
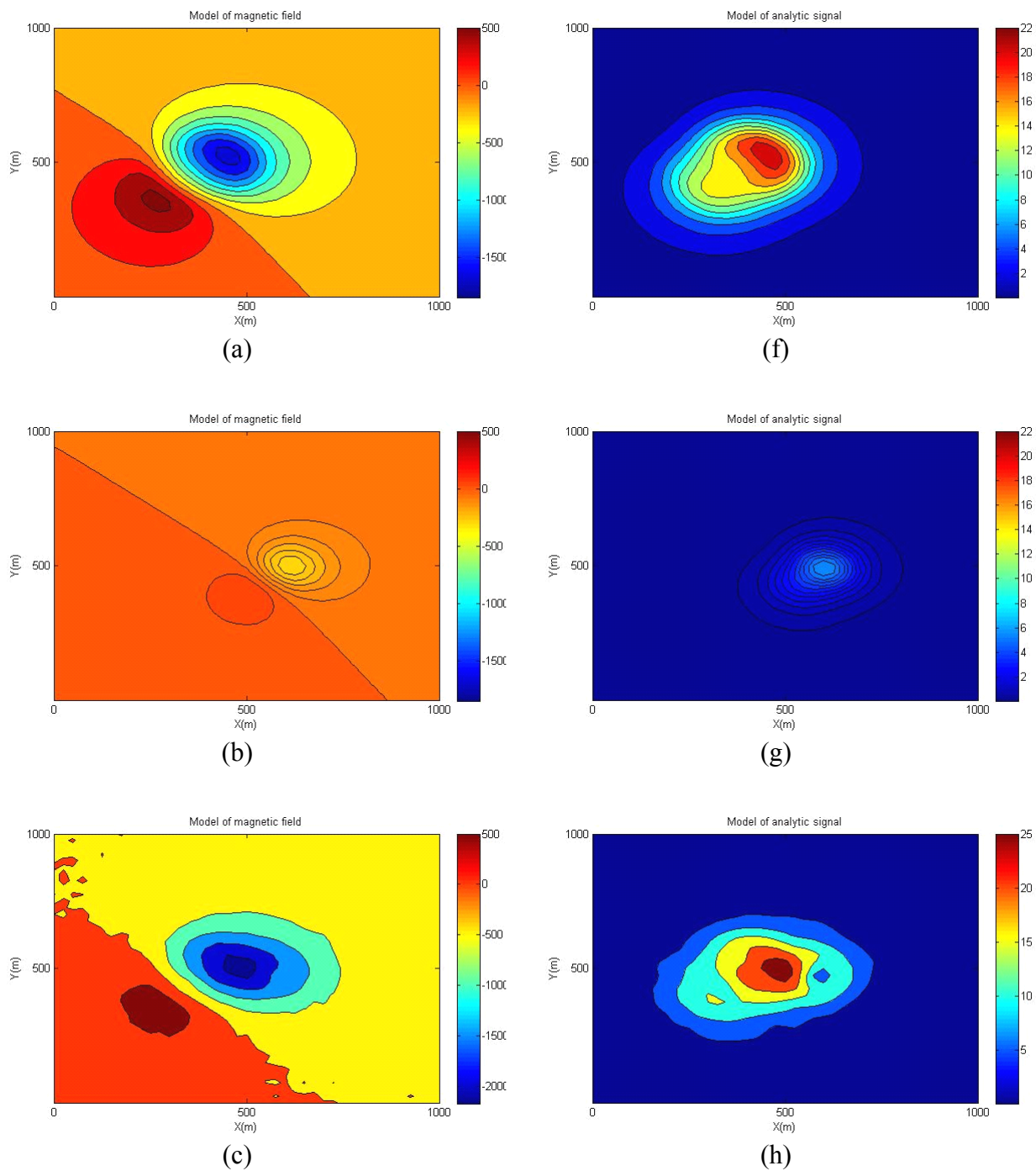
(a)

(f)

(b)

(g)

(c)

(h)

Figure 5.19: Model 10 (two vertical cylinders at an intermediate depth with an inclination and a declination differing from the geomagnetic inclination and declination contaminated with 20nT Gaussian noise): 2D contours of the models and inversion results.

(d)

(i)

(e)

(j)

Figure 5.19: Model 10 (two vertical cylinders at an intermediate depth with an inclination and a declination differing from the geomagnetic inclination and declination contaminated with 20nT Gaussian noise): 2D contours of the models and inversion results (continue).
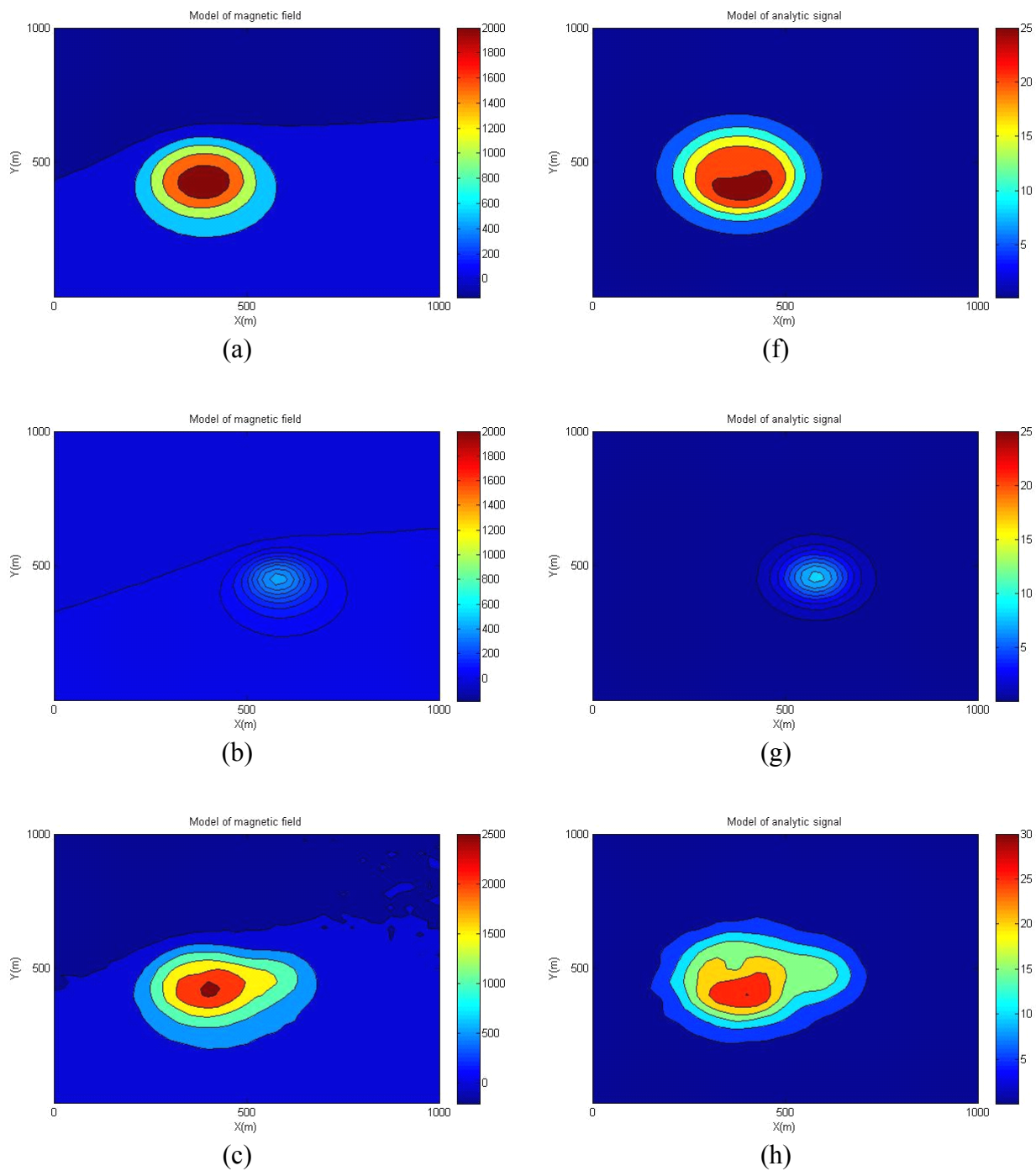
(a)

(b)

(c)

(d)

Figure 5.20: Model 10 (two vertical cylinders at an intermediate depth with an inclination and a declination differing from the geomagnetic inclination and declination contaminated with 20nT Gaussian noise): convergence plots.

The eleventh model consists of two semi-infinite vertical cylinders with diameters of 334m and 167m respectively, located (375m, 500m) and (625m, 500m), at a depth of 26m. The amplitudes of TM is $J_{tot} = 289nT$, and directions of TM are-both $I_{tot} = 143^o$ and $D_{tot} = -31^o$.

Table 5.11 shows that: for the joint inversion of total magnetic field and analytic signal (JIMA), the recover parameters are biased from their true values (first pipe); for the only magnetic field inversion (MFI), the recover parameters are biased from their true values (first pipe); for the only analytic signal inversion (ASI), the recover parameters are far from their true values (first pipe).

Table 5.11: Model 11 (two shallow large diameter vertical cylinders with an inclination and a declination differing from the geomagnetic inclination and declination contaminated with 20nT Gaussian noise): joint inversion of magnetic field and analytic signal (JIMA), magnetic field inversion (MFI) and analytic signal inversion (ASI).

	Mag.(nT)	In.(°)	De.(°)	X.(m)	Y.(m)	Dia.(m)	Dep.(m)
Pipe 1	289	143	-31	375	500	334	26
Pipe 1	289	143	-31	625	500	167	26
Initial	500	120	-15	300	300	200	50
JIMA	328.31	148.45	-25.24	377.13	491.38	335.05	31.91
MFI	340.63	148.67	-23.75	373.94	488.86	331.14	35.22
ASI	408.19	154.21	-65.67	416.36	506.58	366.52	40.80

(a)

(f)

(b)

(g)

(c)

(h)

Figure 5.23: Model 12 (two deep small diameter vertical cylinders similar to a vertical dipole with an inclination and a declination close to the geomagnetic inclination and declination contaminated with 20nT Gaussian noise): 2D contours of the models and inversion results.
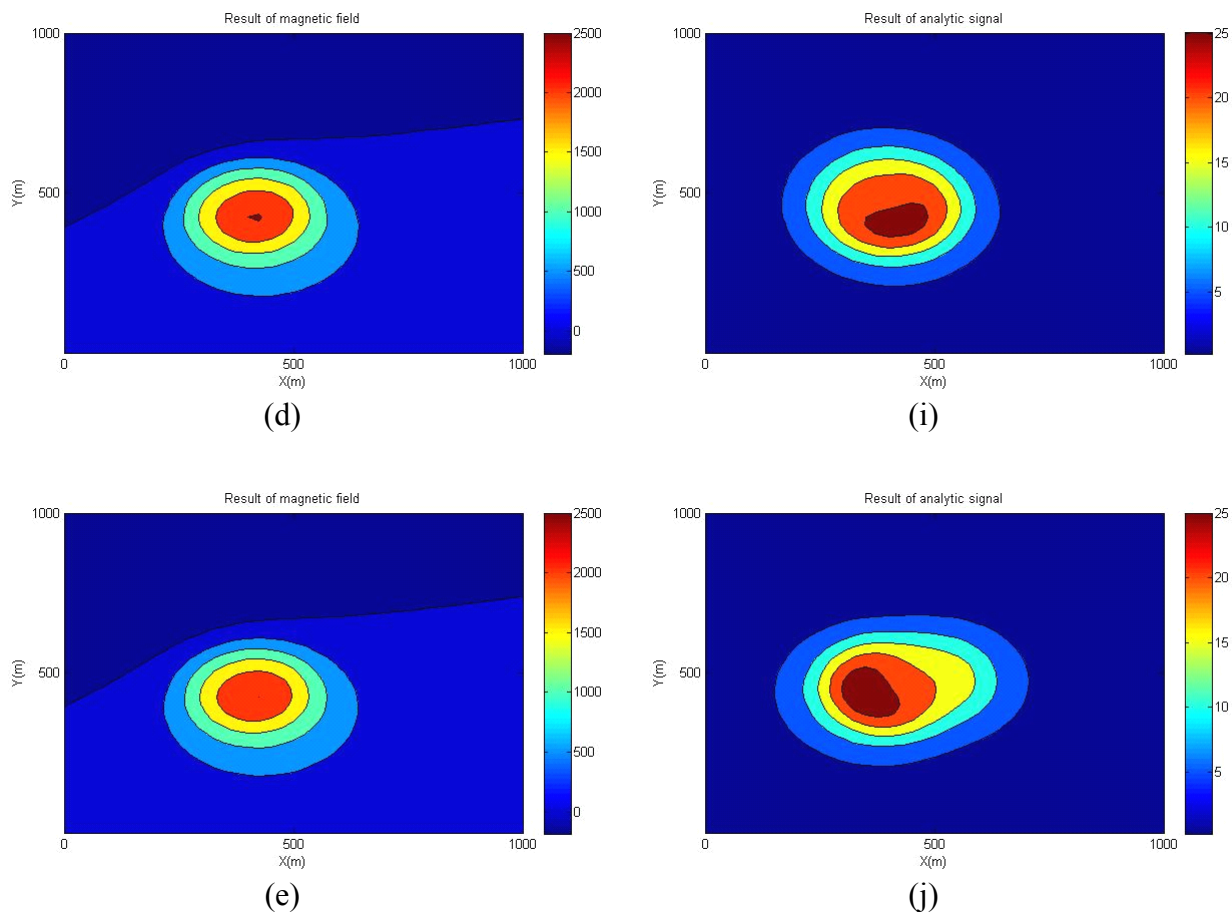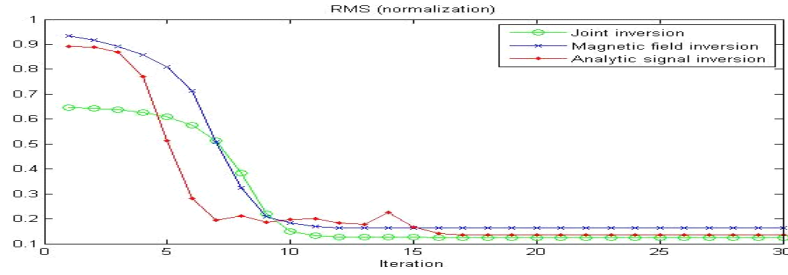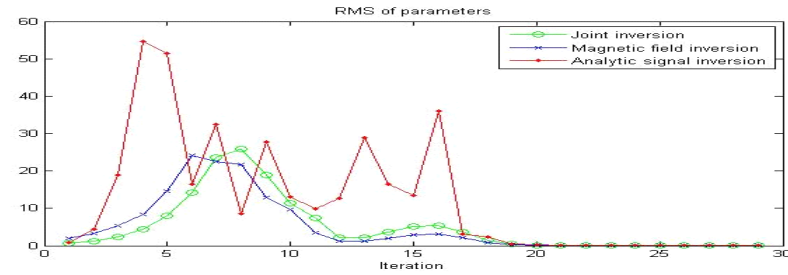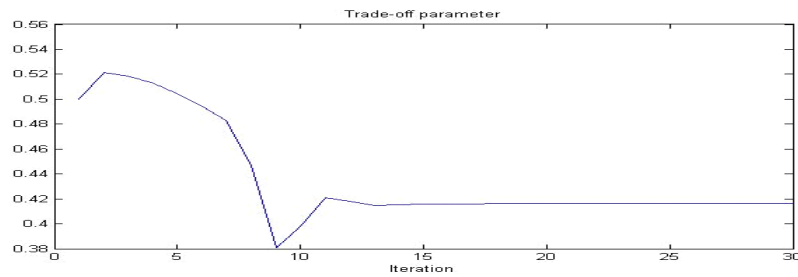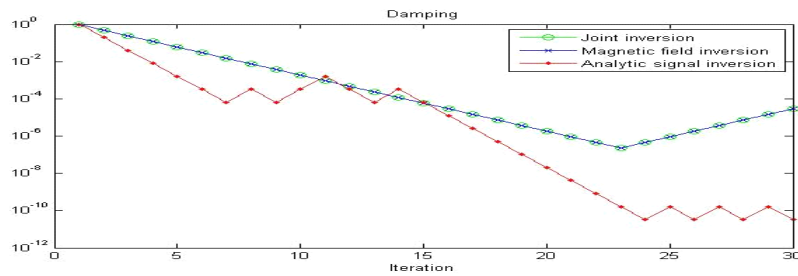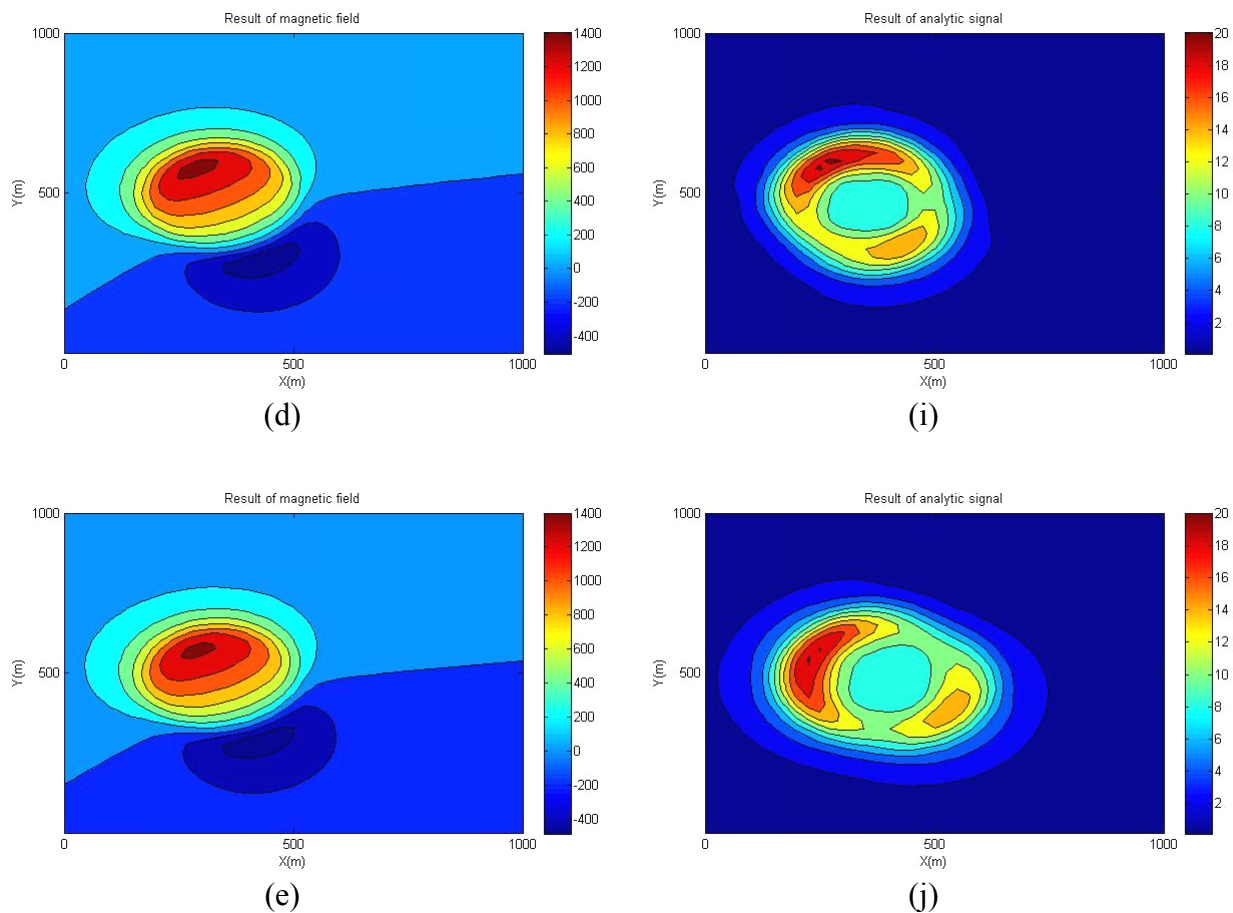
Figure 5.21: Model 11 (two shallow large diameter vertical cylinders with an inclination and a declination differing from the geomagnetic inclination and declination contaminated with 20nT Gaussian noise): 2D contours of the models and inversion results (continue).
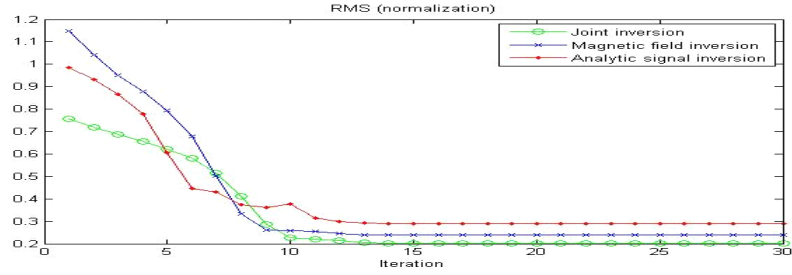
(a)
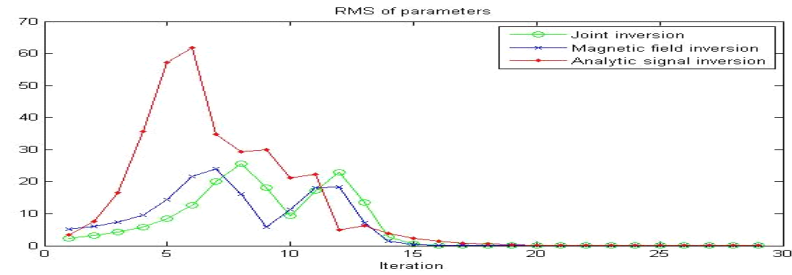
(b)
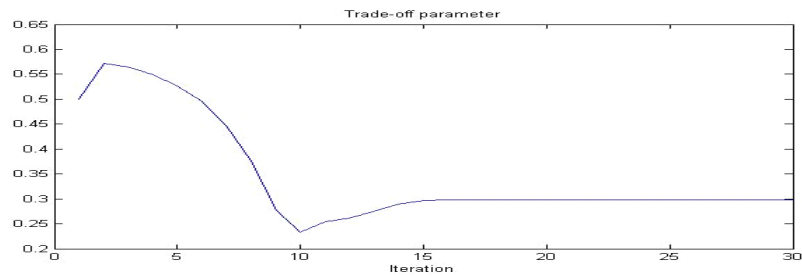
(c)
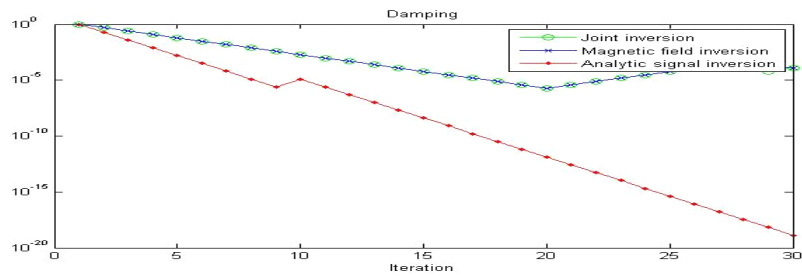
(d)

Figure 5.22: Model 11 (two shallow large diameter vertical cylinders with an inclination and a declination differing from the geomagnetic inclination and declination contaminated with 20nT Gaussian noise): convergence plots.

The twelfth model consists of two semi-infinite vertical cylinders with diameters of 154m and 77m respectively, located (440m, 500m) and (560m, 500m), at a depth of 163m. The amplitudes of TM are $J_{tot} = 2488nT$, and directions of are-both TM $I_{tot} = 83^o$ and $D_{tot} = -8^o$. Table 5.12 shows that: for the joint inversion of total magnetic field and analytic signal (JIMA), the recover parameters are biased from their true values (first pipe); for the only magnetic field inversion (MFI), the recover parameters are biased from their true values (first pipe); for the only analytic signal inversion (ASI), the recover parameters are far from their true values (first pipe).

Table 5.12: Model 12 (two deep small diameter vertical cylinders similar to a vertical dipole with an inclination and a declination close to the geomagnetic inclination and declination contaminated with 20nT Gaussian noise): joint inversion of magnetic field and analytic signal (JIMA), magnetic field inversion (MFI) and analytic signal inversion (ASI).

	Mag.(nT)	In.(°)	De.(°)	X.(m)	Y.(m)	Dia.(m)	Dep.(m)
Pipe 1	2488	83	-8	440	500	154	163
Pipe 2	2488	83	-8	560	500	77	163
Initial	200	-45	-45	300	300	320	60
JIMA	2426.81	82.84	-17.18	459.81	499.37	175.79	166.33
MFI	2327.03	82.96	-16.42	460.18	499.28	179.15	165.29
ASI	3143.06	47.08	60.31	492.38	511.10	162.05	164.11
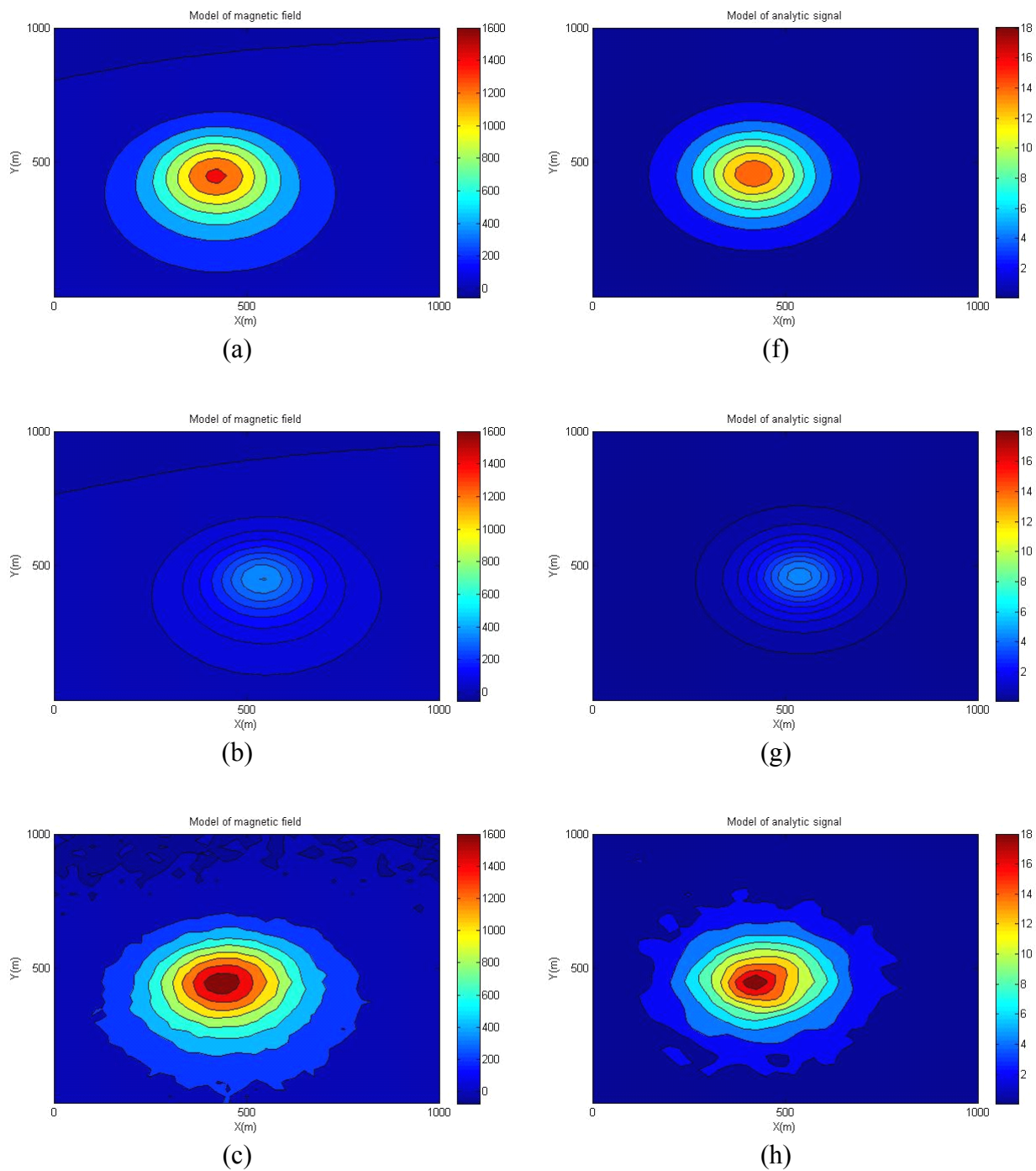
Figure 5.23: Model 12 (two deep small diameter vertical cylinders similar to a vertical dipole with an inclination and a declination close to the geomagnetic inclination and declination contaminated with 20nT Gaussian noise): 2D contours of the models and inversion results.
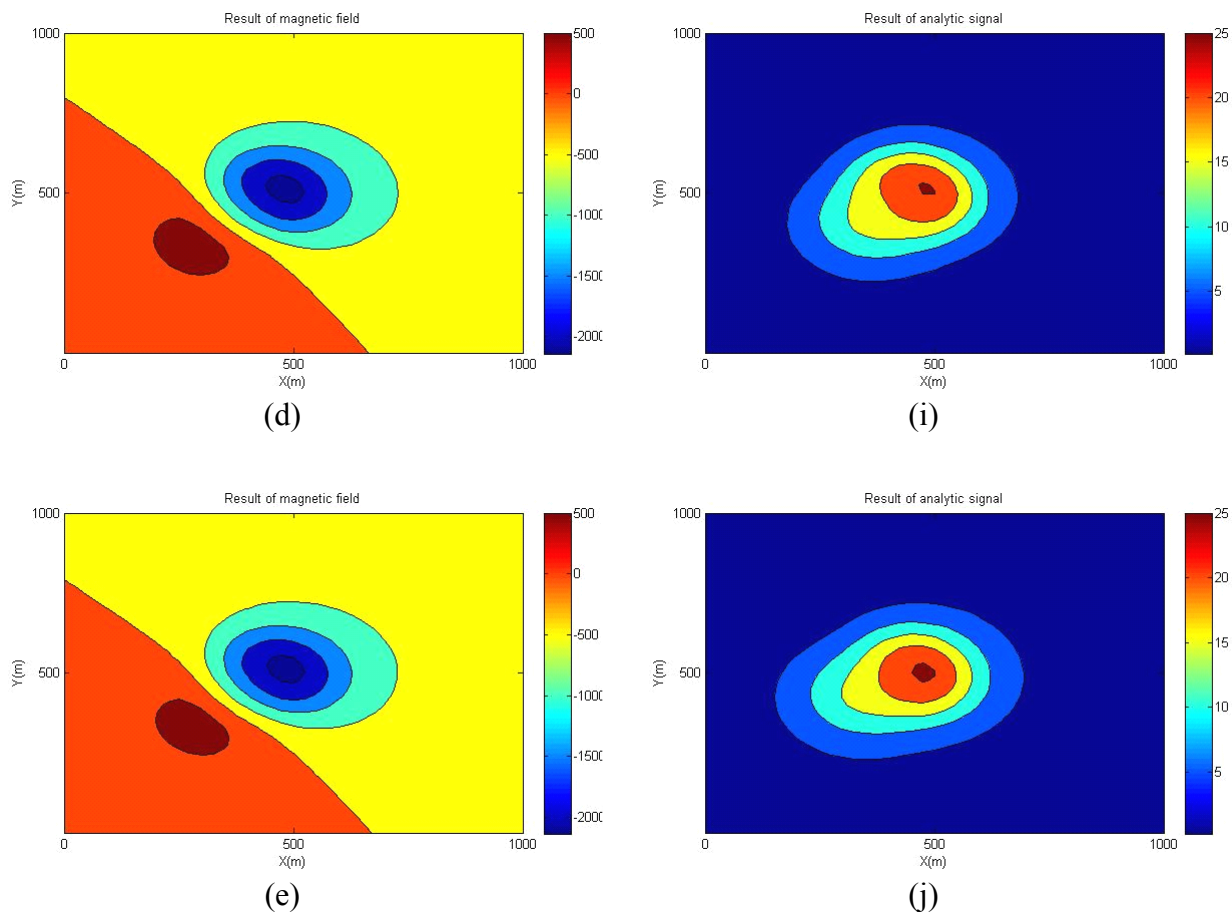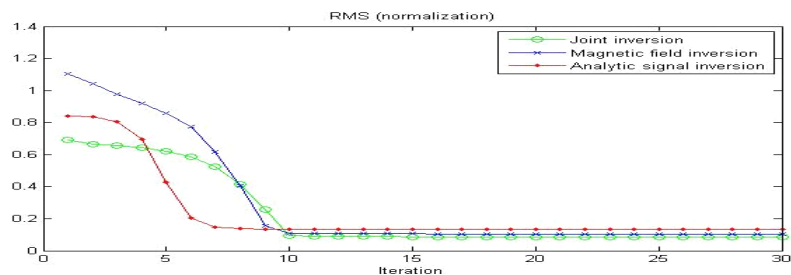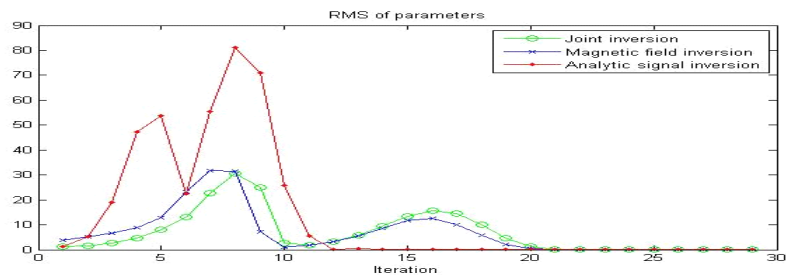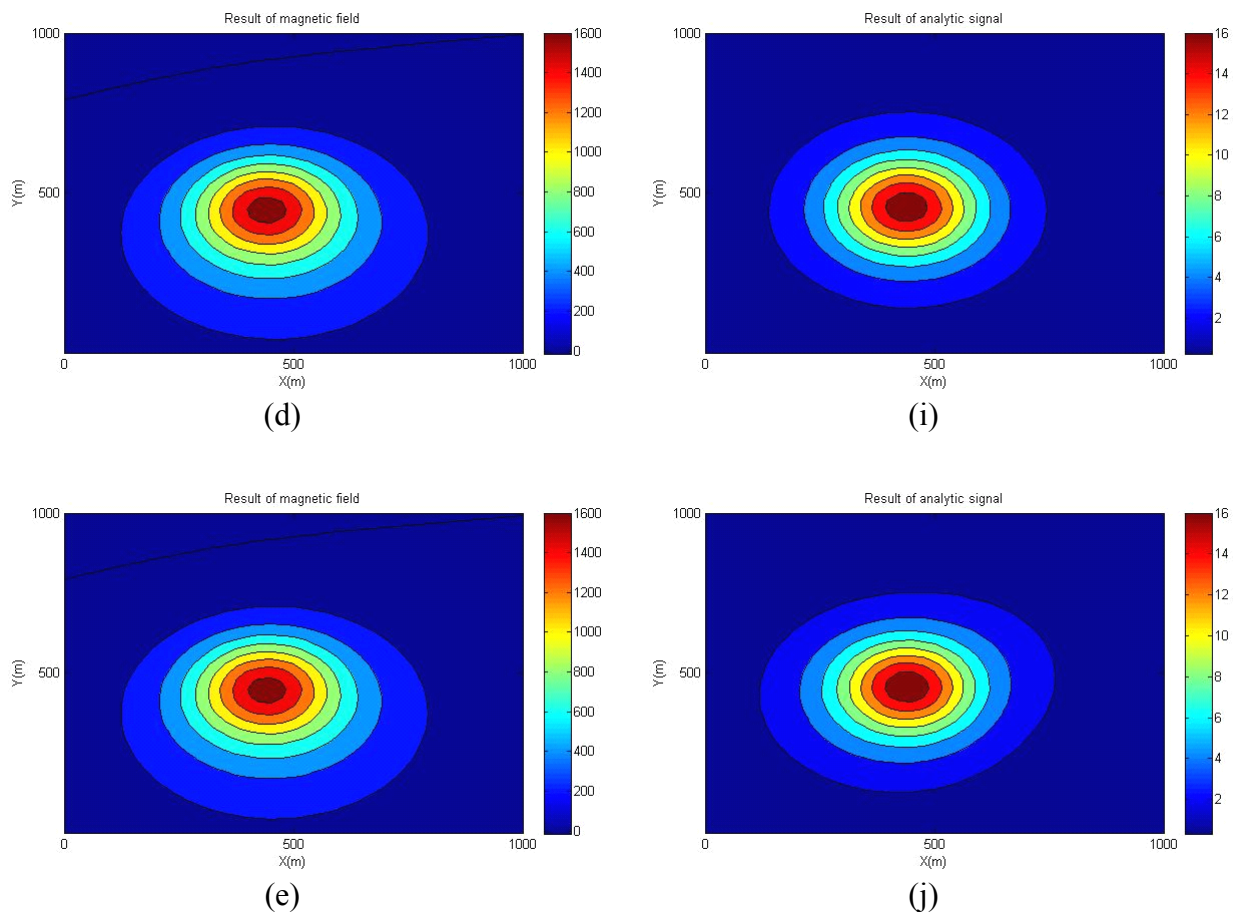
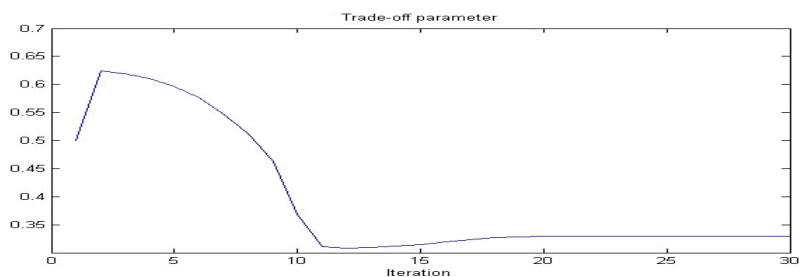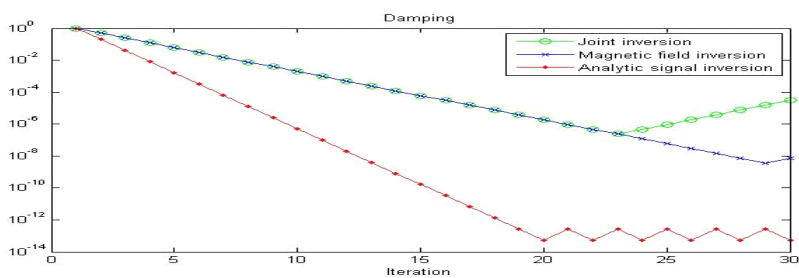Figure 5.23: Model 12 (two deep small diameter vertical cylinders similar to a vertical dipole with an inclination and a declination close to the geomagnetic inclination and declination contaminated with 20nT Gaussian noise): 2D contours of the models and inversion results (continue).
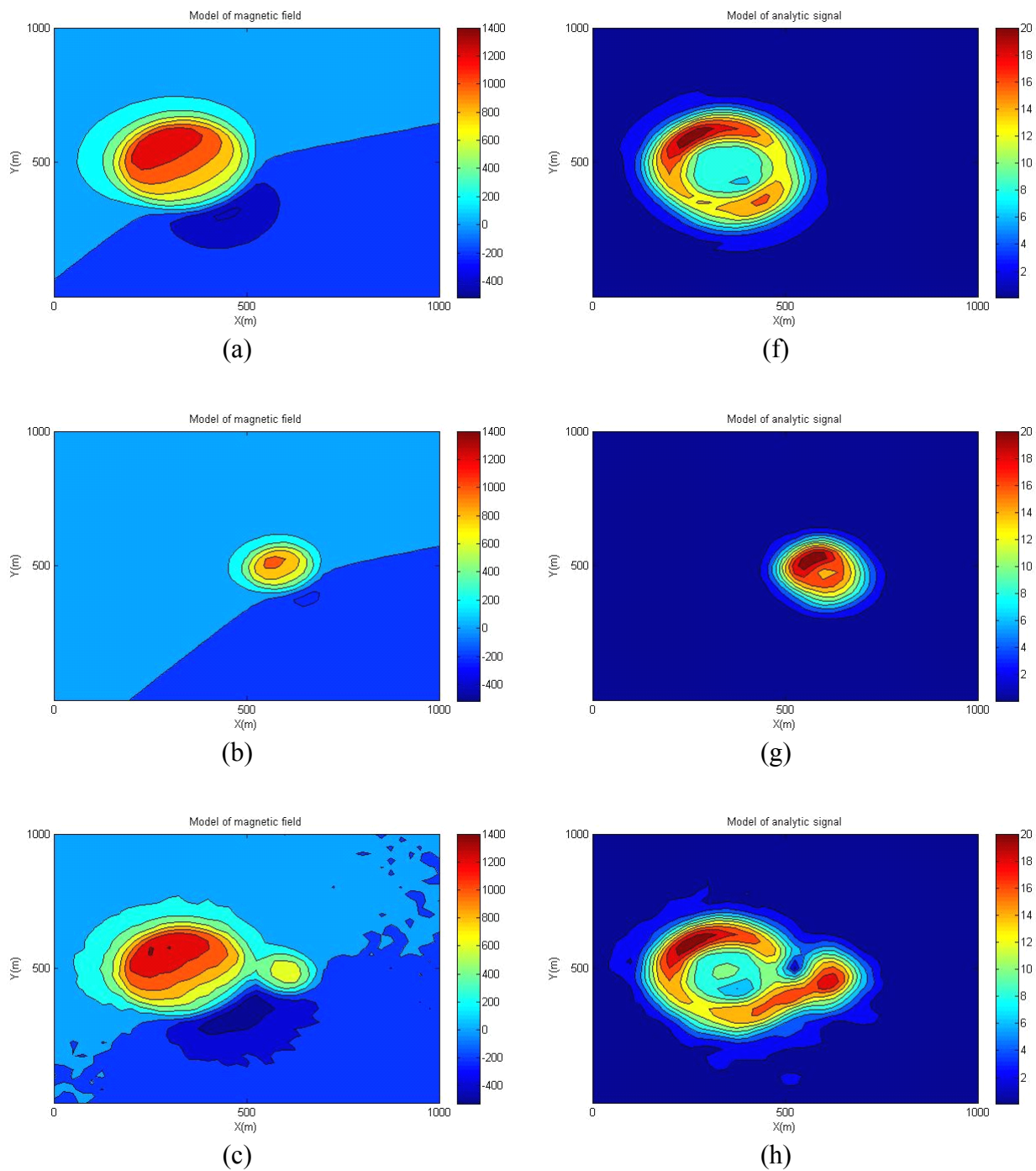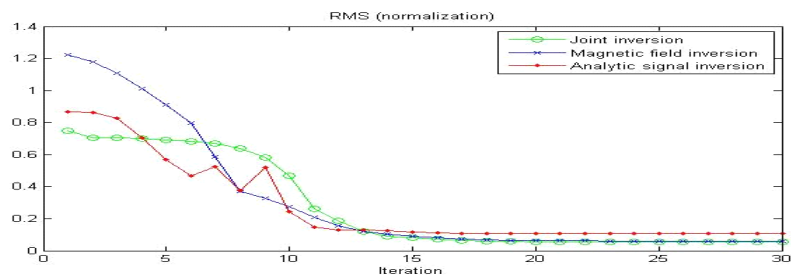
(a)
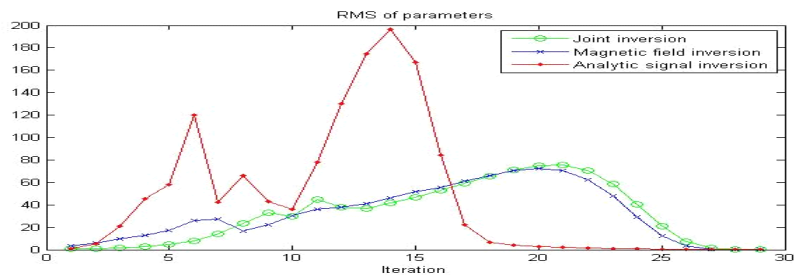
(b)
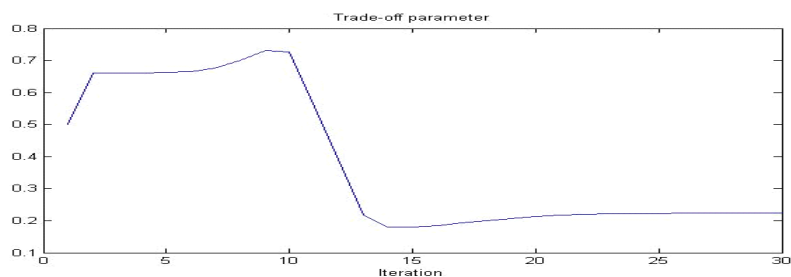
(c)
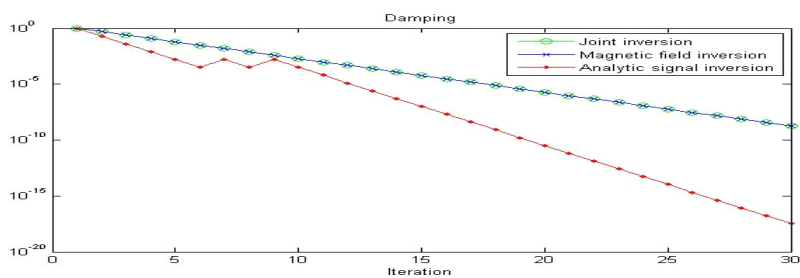
(d)

Figure 5.24: Model 12 (two deep small diameter vertical cylinders similar to a vertical dipole with an inclination and a declination close to the geomagnetic inclination and declination contaminated with 20nT Gaussian noise): convergence plots.

From the tables and figures above, the results computed using joint inversion of magnetic field and analytic signal clearly recovers the model parameters of first pipe for each model, for arbitrary initial parameters. The convergence curves for the inversion for each model are asymptotic. Therefore, the algorithm of joint inversion of magnetic field and analytic signal is stable and accurate.

Comparing the only magnetic field inversion and only analytic signal inversion, the magnetic field inversion is more stable and accurate than the analytic signal inversion. The analytic signal is more sensitive for a small pipe noise. Comparing the results of four models with a small pipe noise, individual parameters are sensitive to a small pipe noise in different models. For the model with large TM inclination, the amplitude and declination of TM and depth of cylinder are sensitive to a small pipe noise; for the model with small TM inclination, the amplitude of TM, location and depth are sensitive to a small pipe noise; for the shallow model, the TM amplitude and depth are sensitive to a small pipe noise; for the deep model, the TM inclination and diameter are sensitive to a small pipe noise.

5.2   Applications

In the region of Lac de Gras, the kimberlite pipes intrude the Archean Slave craton, 300 km northeast of Yellowknife and 200 km south of the Arctic Polar Circle. As yet, over 300 kimberlites have been discovered in this region. The major part of kimberlites is found in the Ekati property where 152 hypabyssal and volcaniclastic kimberlite pipes are reported. Kimberlites are generally located along major lineaments and fault zones. The geology of the region consists of granites, granodiorites, greenstones and metasediments. (Cheman, 2006)

Figure 5.25 shows the aeromagnetic data (public domain) covering the region of Ekati where 15 kimberlites have been identified. The map of total-field magnetic data includes linear anomalies generated by diabase dikes and circular signatures probably generated by kimberlite pipes. The data was collected at an height 120 m above ground along flight lines oriented east - west sampled every 60m, and spaced approximately every 250 meters. Parameters of IGRF-1993 used in the inversion are: $T_0 = 60275$; $I_0 = 84^o$ and $D_0 = 27^o$.
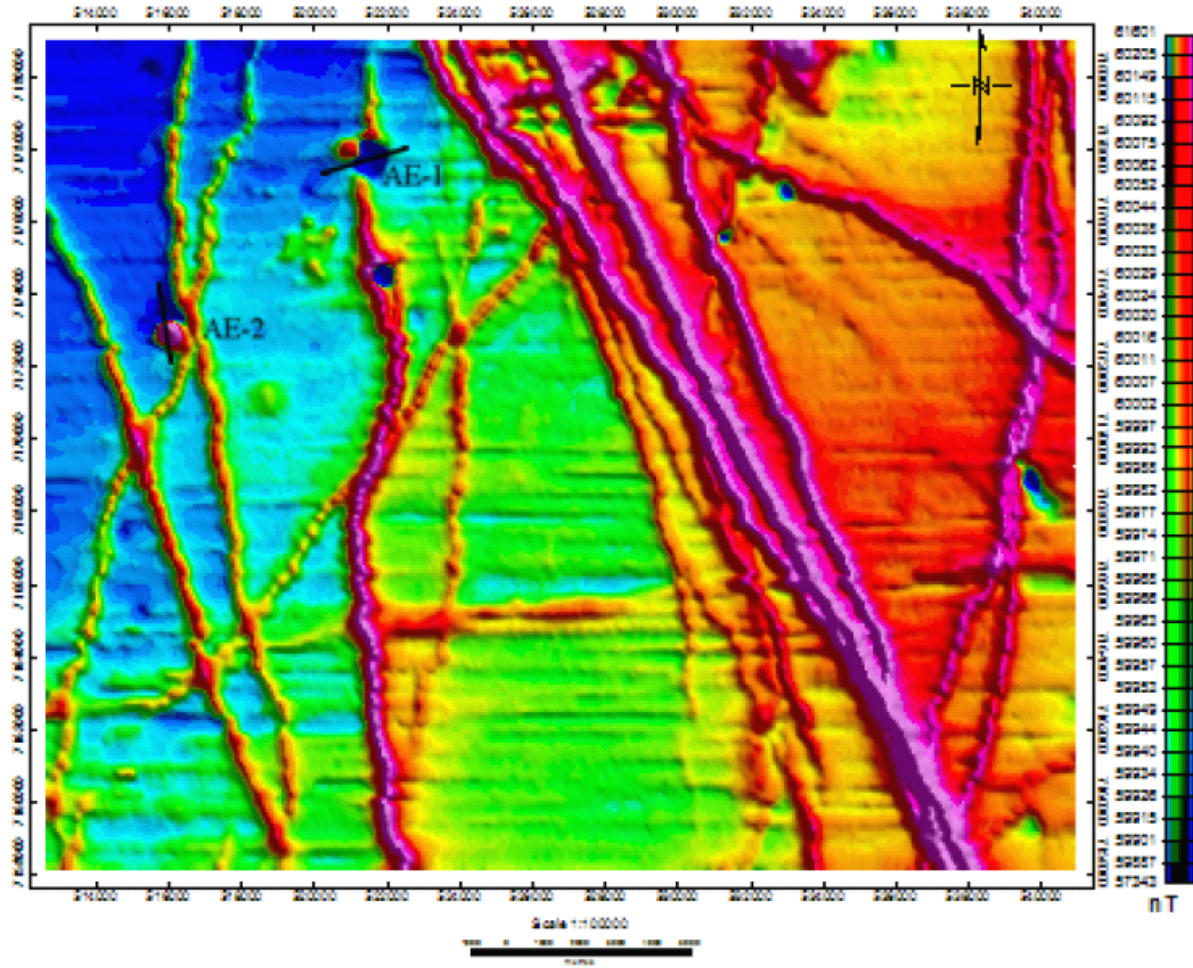
Figure 5.25: Aeromagnetic map (public domain) from a region of Ekati, Lac de Gras. The locations of AE-1 and AE-2 are marked on the map.

Lockhart et al. (2004) published some physical properties of kimberlite in the Ekati area. The magnetic susceptibility of the AE-1 pipe is 0.0095 SI and the AE-2 pipe is 0.011 SI. These measures have been taken in the laboratory on core samples. Other information about the AE-2 is also available that the Königsberger ratio (Q=18.43) and the intensity of RM $\left(J_{rem} = 8.3 \text{A/M}\right)$. However, according to the susceptibility and Königsberger ratio of AE-2 pipe, the value of RM intensity of AE-2 is wrong. I computed the correct value is $\left(J_{rem} = 0.83 \text{A/M} = 1044.03 \text{nT}\right)$. Meanwhile, Cheman (2006) estimated parameters of these two pipes computed by 2D inversion. Cheman's results also proved that Lockhart et al. (2004) published a wrong value.

AE-1, named Grizzly, is located on a north-south dike. The magnetic anomaly of dike is strong intensity that the observation of magnetic anomaly polarity of kimberlite pipe is reverse. Because the total-field magnetic data consist of magnetic responses of both dike and kimberlite pipe, the TM is not just a magnetic property of Grizzly. Therefore, I cannot estimate the RM and Königsberger ratio from the TM.

The area was extracted from aeromagnetic data for interpretation. Each are is 1,500m by 1,500m sampled with 25m spacing (61 x 61). The inversion parameters are: number of iterations 30, initial damping factor 1 and initial trade-off parameter 0.5. Inversion stops when the data misfit of magnetic field and analytic signal is less than 10^{-6}.

Table 5.13 shows the results of joint inversion of magnetic field and analytic signal: the pipe is estimated a diameter of 463.42m, and located at a depth of 21.82m, amplitude of TM is $J_{tot} = 283.35\text{nT}$, inclination of TM is $I_{tot} = -57.60^{\circ}$.

Comparing to the results estimated by Cheman (2006), some results are the same: the pipe is estimated a diameter of 473m, and located at a depth of 21m; the other results are not the same: amplitude of TM is $J_{tot} = 149nT$, inclination of TM is $I_{tot} = -73^{\circ}$. Because the results estimated by Cheman were computed by 2D inversion, they are dependent on the selected profile. Figure 5.25 shows that the profile of Grizzly chose by Cheman is from east to west and avoid the anomaly at the north east of pipe, which is caused by the kimberlite pipe or dike that impact the results of 2D inversion.

Figure 5.26 shows that the total-field magnetic data and its analytic signal data computed by final parameters of joint inversion approximately recover the observed data. Figure 5.27 shows that the data misfits for magnetic field and analytic signal tend to minimum respectively, and parameter changes tend to zero. The trade-off parameter is asymptotic to 0.55. The damping factor decreases with increasing iteration number. The joint inversion is stable and recovers observed data within some errors.

Table 5.13: AE-1: Initial and final parameters of joint inversion of magnetic field and analytic signal.

	Mag.(nT)	In.(°)	De.(°)	X.(m)	Y.(m)	Dia.(m)	Dep.(m)
Initial	500	-45	-30	500	500	400	80
Final	283.35	-57.60	-43.79	829.28	626.48	463.42	21.82

(a) (c)

(b) (d)
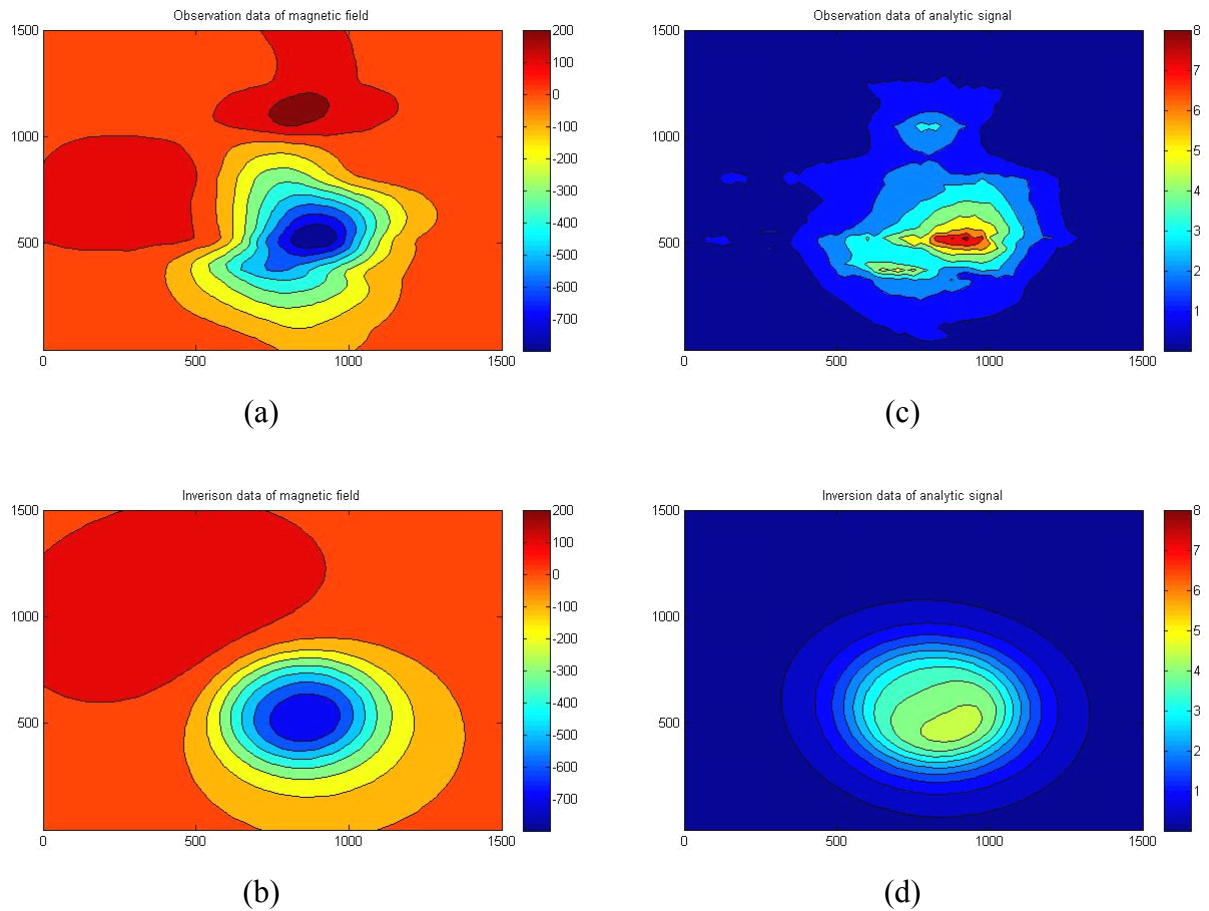
Figure 5.26: AE-1: joint inversion of magnetic field and analytic signal, X-axis is directed to the east and Y-axis is directed to the north: (a) observed total-field magnetic data, (b) total-field magnetic response to the modeled pipe, (c) computed analytic signal data from total-field data, (b) analytic signal response to the modeled pipe.
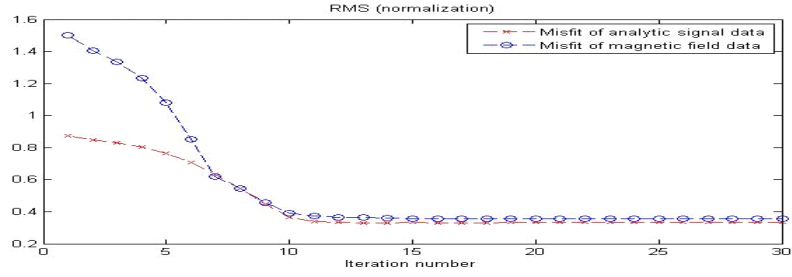
(a)
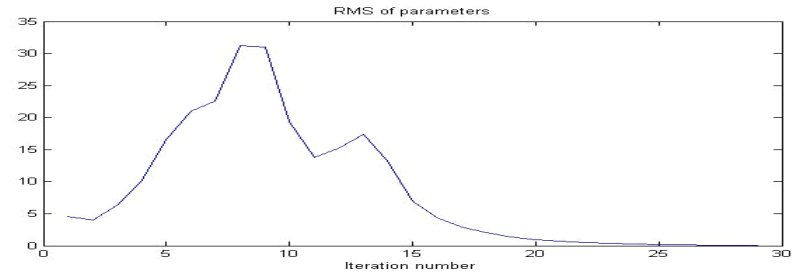
(b)
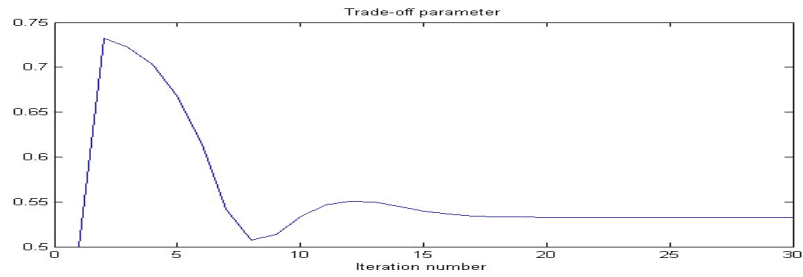
(c)
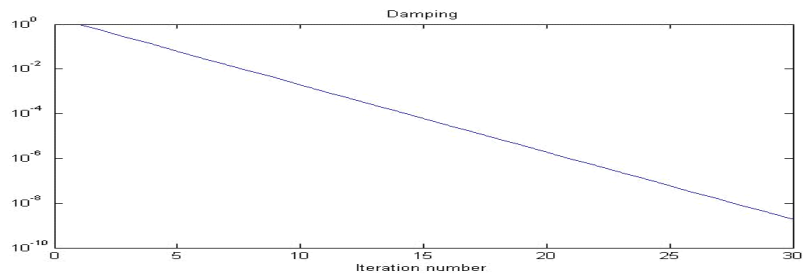
(d)

Figure 5.27: AE-1: (a) data misfits of magnetic field and analytic signal respectively, (b) parameter changes, (c) trade-off parameter, and (d) damping factor.

AE-2, named Leslie, is located near a crossing of two dikes. Fortunately, the observed magnetic anomaly is not affected by both dikes and the polarity is normal, the TM reflects the only magnetic property of Leslie. Therefore, the RM and Königsberger ratio can be estimated from the TM.

The survey area were extracted from aeromagnetic data for interpretation. It is 1,000m by 1,000m sampled with 25m spacing (41 x 41). The inversion parameters are: number of iterations 30, initial damping factor 1 and initial trade-off parameter 0.5. Inversion stops when the data misfit of magnetic field and analytic signal is less than 10^{-6}.

Table 5.14 shows the results of joint inversion of magnetic field and analytic signal: the pipe is estimated a diameter of 301.82m, and located at a depth of 15.01m, amplitude of TM is $J_{tot} = 917.04\text{nT}$, inclination of TM is $I_{tot} = 59.24^\circ$.

Comparing to the results estimated by Cheman (2006), the results are not the same: the pipe is estimated a diameter of 208m, and located at a depth of 24m, amplitude of TM is $J_{tot} = 1071nT$, inclination of TM is $I_{tot} = 82^\circ$. Because the results estimated by Cheman were computed by 2D inversion, they are dependent on the selected profile. Figure 5.25 shows that the profile selected by Cheman for Leslie is north-south and does not cross the magnetic anomaly at its maximum.

Figure 5.28 shows that the total-field magnetic and analytic signal responses computed from the interpreted model by joint inversion approximately recover the observed data. Figure 5.29 shows that the data misfits of magnetic field and analytic signal tend to minimum respectively, and parameters change tend to zero. The trade-off parameters are asymptotic to 0.55. The damping factor decreases with increasing iteration number. The joint inversion is stable and the computed data fit observed data within some small errors.

Table 5.14: AE-2: Initial and final parameters of joint inversion of magnetic field and analytic signal.

	Mag.(nT)	In.(°)	De.(°)	X.(m)	Y.(m)	Dia.(m)	Dep.(m)
Initial	1000	75	-10	500	500	400	80
Final	917.04	59.24	-25.68	505.51	473.65	301.82	15.01

(a)　　　　　　　　　　　　　　　　(c)

(b)　　　　　　　　　　　　　　　　(d)
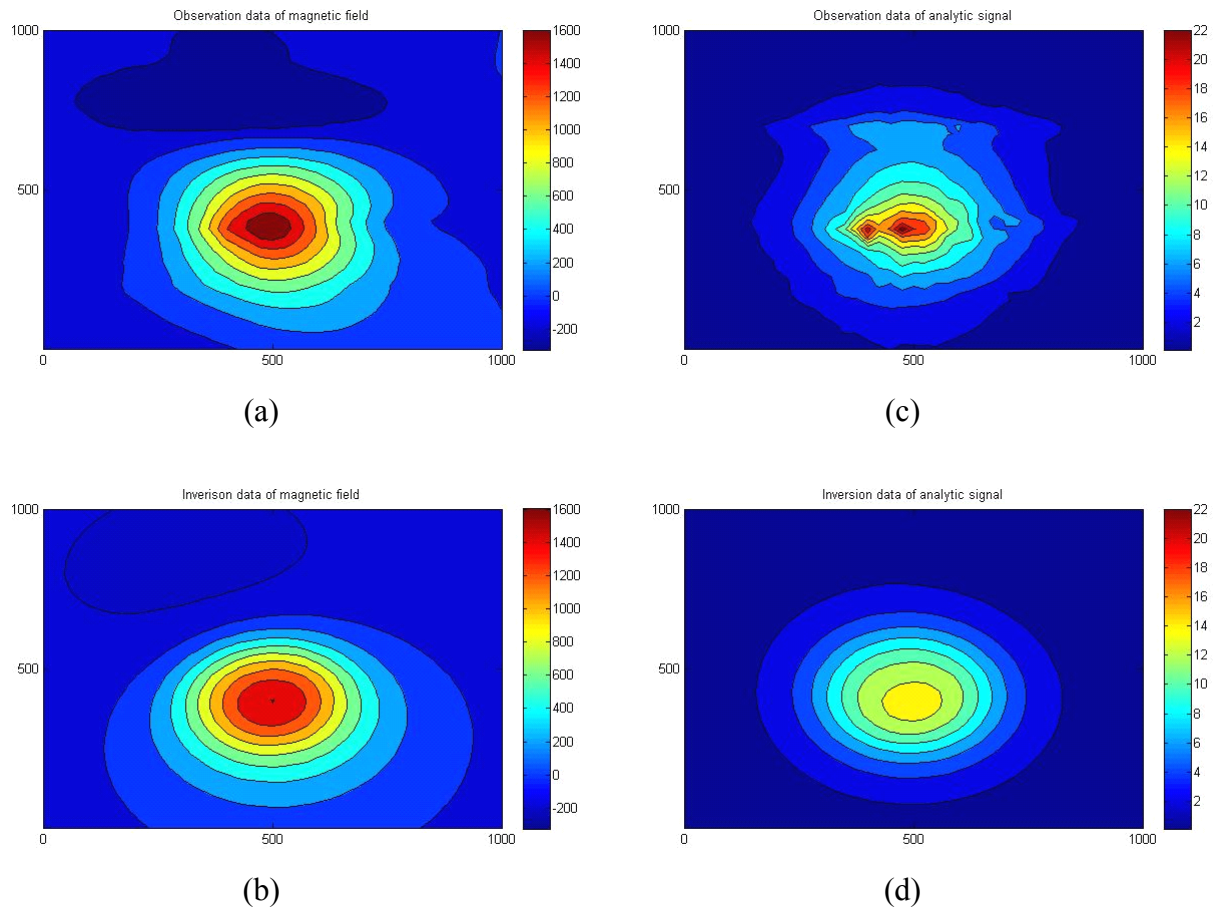
Figure 5.28: AE-2: joint inversion of magnetic field and analytic signal, X-axis is directed to the east and Y-axis is directed to the north: (a) observed total-field magnetic data, (b) total-field magnetic response to the interpreted model, (c) computed analytic signal data from the total-field data, (d) analytic signal response to the interpreted model.
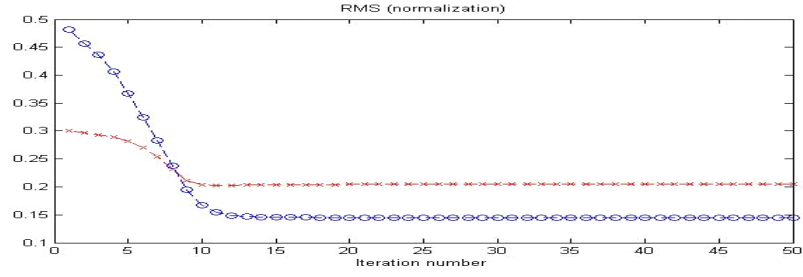
(a)
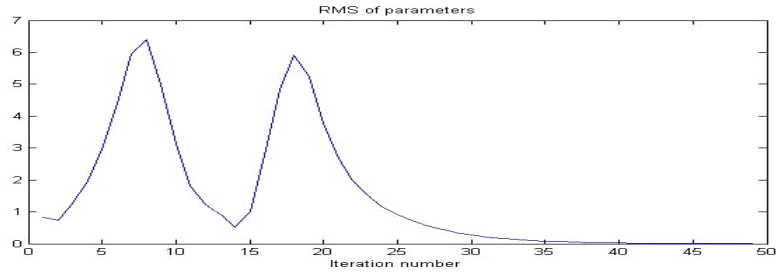
(b)
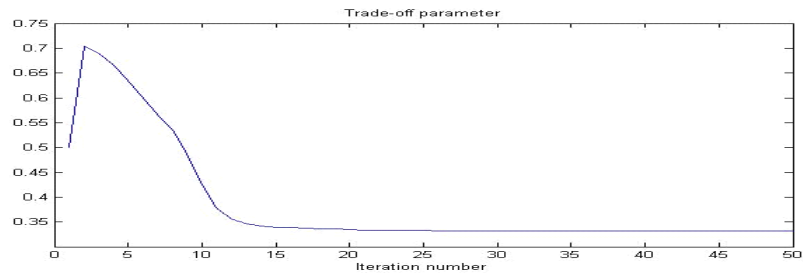
(c)
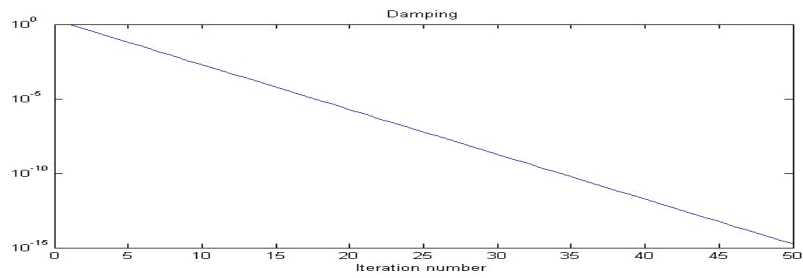
(d)

Figure 5.29: AE-2: (a) data misfits of magnetic field and analytic signal respectively, (b) parameter changes, (c) trade-off parameter, and (d) damping factor.

As mentions before, RM and the Königsberger ratio of Leslie pipe were given in Lockhart et al. (2004) to be $J_{rem} = 1044.03 nT$ and Q=18.43, and they are also estimated by Cheman (2006) to be $J_{rem} = 1021.37 nT$ and Q=23.4. Thus, Cheman's results underestimate RM by 2.17% and overestimate the Königsberger ratio by 26.97%.

According to the relationship between the RM and TM, RM and the Königsberger ratio can be computed as $J_{rem} = 870.58 nT$ and Q=16.50. Because the survey frequency-domain EM data is not available, the susceptibility is assumed to be 0.011SI, as given by Lockhart et al. (2004). Thus, the joint inversion underestimates RM by 16.61% and the Königsberger ratio by 10.47%.

For the application, the results of joint inversion (3D inversion) are not comparable to the ones obtained by Chemam (2D inversion). In some cases, the results from 2D inversion are more accurate than 3D inversion, but they are dependent on the profile selected. Therefore the 3D inversion is more stable than 2D inversion. In terms of 3D inversion, the algorithm of inversion is stability and feasibility, because the results approximately fit the observed data and the convergence curves for the inversion for each model are asymptotic to some limits.

There is an problem with the analytic signal data.The magnetic survey was flown in the E-W direction (x-axis) and therefore sampling in the x direction is much denser than in the y-direction (orthogonal to the flight lines); in addition, incomplete leveling of the survey data generates corrugation (Figure 5.25). This causes large elongated anomalies in the x-direction in the analytic signal data computed by Fourier transform (Figure 5.27c and 5.28c).

5.3   Conclusion

From the synthetic examples test, the three methods of inversion are precise and stable. All the results of the proposed methods approximate the observation data of total-field magnetic and its analytic signal. From the application examined, the results of joint inversion approximately fit the observed data, and the convergence curves for the inversion for each model are asymptotic to some limits, the RM and Königsberger ratio are close to the real value published by Lockhart et al. (2004). Therefore, the algorithm of joint inversion is stable and feasible.

The bias in the inversion results are caused by different types of noise due to the different signal to noise ratio. The Gaussian noise or anomaly generated by shallow magnetic anomalous body is enhanced by analytic signal that reduces the signal to noise ratio. A plane regional or anomaly generated by deep magnetic anomalous body is weakened by analytic signal that increases the signal to noise ratio. Therefore, the magnetic field inversion is affected by noise generated by deep magnetic anomaly, and the analytic signal inversion is disturbed by noise generated by shallow magnetic anomaly. The joint inversion of magnetic field and analytic signal balances the advantages of magnetic field inversion and analytic signal inversion separately controlled by trade-off parameters.

Comparing the three method of inversion, the joint inversion of magnetic field and analytic signal is less sensitive to noise than magnetic field inversion and analytic signal inversion separately. The joint inversion of magnetic field and the analytic signal is superior in terms of precision and stability compared to magnetic field inversion and analytic signal inversion separately.

There is a problem occurring in case of large depth and small size models (model 4 and model 8) in presence of noise. For these models, the analytic signal inversion is unstable. The parameter changes do not converge to low values but data misfits do. The reason is that the analytic signal enhances the responses caused by shallow sources and reduces the responses caused by deep sources; in addition to the reduction of long wavelength anomalies, the analytic signal is a high-pass filter and therefore there is an increase of the short-wavelength Gaussian noise. When the cylinder is deep it can be modeled as a magnetic monopole and in that case neither the TM nor the diameter of the cylindrical pipe can be resolved but only the product of the TM by the section area ($\sim a^2$). Therefore, the results of analytic signal inversion is non-unique causing the algorithm to be unstable and inaccurate,the data misfit still being very small.

CONCLUSION

The RM is a major contributor to the magnetic anomalies for detecting kimberlite, but it complicates the magnetic data interpretation. In Canada, many kimberlites from the Northwest Territories show strong RM. Therefore, overcoming the influences of RM and separating the RM from the TM are very necessary. To interpret the magnetic data over kimberlite pipe with strong RM, Chemam (2006) and Chen (2009) did the parametric inversion of magnetic field and analytic signal due to the vertical right cylinder with arbitrary polarization. However, when the susceptibility is unknown, the RM cannot be estimated from magnetic responses and separated from the TM directly. Most of methods use the mathematical relationships or direction bias to estimation the RM, such as minimizing the amplitude of RM. These methods cannot obtain the certain RM, because the RM not only biases the direction of TM but also change the amplitude of TM.

In this thesis, I developed a method to interpret the magnetic survey data over kimberlite pipe in presence of RM and to separate the RM from the TM. The joint inversion of the total-field magnetic data and its analytic signal is performed to obtain the TM and geometry properties. Then, the one dimension frequency-domain electromagnetic inversion is applied to obtain the magnetic susceptibility. Finally, the RM is separated from the TM.

The analytic signal is derived using Fourier transform method and it can obtain the vertical derivative from the two horizontal derivatives. The concept is based that the gradient divergence is zero in passive field. Four synthetic models have been used to test the effectiveness of this algorithm.

A 3D parametrical inversion of total-field magnetic data and its analytic signal data has been implemented. The algorithm based on Gauss-Newton method is applied by singular value decomposition and Marquardt's factor. The joint inversion of total-field magnetic data and its analytic signal provides more precision and stable solution than separate inversions of the data. Four synthetic models have been applied to validate the effectiveness of this algorithm.

I combine the magnetic technique with the EM technique to separate the RM from the TM. The concept is based on the relationship between the RM and the TM of kimberlite pipe. The susceptibility is a kernel parameter that can be determined by EM technique. The 1D inversion of

frequency-domain EM data for magnetic susceptibility and electric conductivity proposed by Zhang and Oldenburg (1996) is used. The solutions are computed using the program "EM1DFM" published by UBC (University of British Columbia). Two synthetic models have been tested to validate the effectiveness of the algorithm.

Although a procedure for the interpretation of magnetic data in combination with the frequency EM technique in presence of strong RM is established, some practical issues still exist.

For the joint inversion of magnetic field and analytic signal, the key problem is the accuracy of inversion algorithm. The analytic signal inversion is unstable when the magnetic anomaly is similar to a monopole. Because the analytic signal enhances the responses caused by shallow sources and reduces the responses caused by deep sources; in addition to the reduction of long wavelength anomalies, the analytic signal is a high-pass filter and therefore there is an increase of the short-wavelength Gaussian noise. When the cylinder is deep it can be modeled as a magnetic monopole and in that case neither the TM nor the diameter of the cylindrical pipe can be resolved but only the product of the TM by the section area ($\sim a^2$). Therefore, the results of analytic signal inversion is non-unique causing the algorithm to be unstable and inaccurate,the data misfit still being very small.

For the EM inversion of conductivity and susceptibility, the algorithm of inversion may be unstable and inaccurate. The results of conductivity and susceptibility models from inversion depend on reference conductivity and susceptibility models. Because the main purpose of "EM1DFM" is to recover a good conductivity model unaffected by susceptibility effects in the EM data, so it is rather hard to get a good susceptibility model. Basically, the EM data are mostly sensitive to the conductivity and are only slightly sensitive to susceptibility, because the susceptibility in EM data is a second-order effect that can be detected only at low induction number (e.g. low frequency). Therefore, a strong expertise is needed to obtain good.

There is an additional problem with the analytic signal data. The magnetic survey was flown in the E-W direction (x-axis) and therefore sampling in the x direction is much denser than in the y-direction (orthogonal to the flight lines); in addition, incomplete leveling of the survey data generates corrugation. This causes large elongated anomalies in the x-direction in the analytic signal data computed by Fourier transform.

Based on existing software implementation and my experience, the future work can be outlined as follow:

First, the joint inversion of magnetic field and analytic signal can be improved when the magnetic anomaly is similar to a monopole. In that case it is better to invert for the pole strength (TM x section area). Because the analytic signal increases the short wavelength noise and suppresses the responses of deep anomaly, an increase in the resolution of analytic signal data can improve joint inversion.

Second, the inversion of electromagnetic data needs further improvement. The algorithm of electromagnetic inversion can use a reference model and weightings, and the susceptibility to be only in certain depth ranges in the model. The in-phase data only could be used because the magnetic susceptibility can be observed in the negative low-frequency in-phase values.

Finally, the kimberlite exploration needs a integrated interpretation of the magnetic data, the EM data, the geological information, environment setting, and any prior knowledge and information. Although the inversion algorithm suits for most cases and is independent on the initial parameters and reference parameters, the final success of exploration depends on the interpreter's experience and local knowledge.

REFERENCES

Anderson, W. L. (1982). Fast Hankel transforms using related and lagged convolutions: *ACM Trans. Math. Software*, 8, 344-368.

Arnott, F., and Kostlin, E. (2003). Petrophysics of kimberlites: 8th *International Kimberlite Conference (IKC).*

Atkinson, W. J. (1989). Diamond exploration philosophy, practice, and promises: a review. kimberlite and related rocks: their mantle-crust setting, diamonds, and diamond exploration. Vol.2. Edited by J. Ross, A. L. Jaques, J. Ferguson, D. H. Green, S. Y. O' Reilly, R. V. Duncan, and A. J. A. Janse. *Proceedings* 4th *International Kimberlite Conference, Perth, Australia, 1986. Geological Society of Australia Sciety of Australia Special Publication,* 14.1075-1107.

Ballantyne Jr., E. J. (1980). Magnetic curve fit for a thin dike-calculator program (TI-59): *Geophysics*, 45,447-445.

Barongo, J. O. (1985). Method for depth estimation and aeromagnetic vertical gradient anomalies: *Geophysics*, 50, 963-968.

Beamier, M., Dion, D. J., Lasalle, P. And Moorhead, J. (1993). Exploration du diamant au Temiscamingue: *RRO 93-08, Quebec.*

Beard, L. P., and Nyquist, J. E. (1998). Simultaneous inversion of airborne electromagnetic data for resistivity and magnetic permeability: *Geophysics*, 63, 1556-1564.

Bhattacharyya, B. K. (1980). A generalized multibody model for inversion of magnetic anomalies: *Geophysics*, 45, 255-270.

Blakely, R. J. (1996). Potential theory in gravity and magnetic applications: *Cambridge University Press.*

Burley, A. J., and Greenwood, P. G. (1972). Geophysical survey over kimberlite pipes in Lesotho. London*: Institute of Geological Science, Geophysical Division, Applied GEOPHYSICS Unit.*

Cheman, A. (2006). Inversion magnetique tridimensinnelle des anomalies circulaires "kimberliteques" isolees avec presence ou sans remanence. *M.Sc A. inédit, École Polytechnique, Montréal (Canada).*

Chen, J. (2009). Joint inversion of magnetic field and analytic signals due to a vertical right circular cylinder with arbitrary polarization in the presence of remanent magnetization. *M.Sc A. inédit, École Polytechnique, Montréal (Canada).*

Clark, D. A. (1983). Comments on magnetic petrophysics. Bull. *Aust. Soc. Explor. Geophys.,* 14(2): 49-62.

Coopersmith, H. G., and Mitchell, R. G. (1989). Geology and exploration of the rose lamproite, south-east Kansas. kimberlite and related rocks.*: Their Mantle-Crust Setting, Diamonds, and Diamond Exploration.* Vol.2. Edited by Ross, J., Jaques, A. L., Ferguson, J., Green, D. H., O' Reilly, S. Y., Duncan, R. V., and Janse, A. J. A. *Proceedings 4th International Kimberlite Conference, Perth, Australia, 1986. Geological Society of Australia Sciety of Australia Special Publication* 14.1179-1191.

Cowan, D. R., Tompkins, L. A., and Cowan, C. (2000). Screening kimberlite magnetic anomalies in magnetically active areas: *Exploration Geophysics*, 31, 66-72.

Debeglia, N., and Corpel, J. (1997). Automatic 3-D interpretation of potential field data using analytic signal Derivatives: *Geophysics,* 62(1), 87-96.

Dortman, N. B. (2004). Les propriétés physiques des roches et des minéraux utiles (Petrophysique): *Edition "Nedra" no 2, Moscou.*

Farquharson, C. G., Oldenburg, D. W., and Routh, P. S. (1993). Inversion of time-domain electromagnetic data for a horizontally layered earth: *Geophys. J. Internate.*, 114, 433-442.

Farquharson, C. G., Oldenburg, D. W., and Routh, P. S. (1996). Approximate sensitivities for the electromagnetic inverse problem: *Geophys. J. Internate.*, 126, 235-252.

Farquharson, C. G., Oldenburg, D. W., and Routh, P. S. (2003). Simultaneous 1D inversion of loop-loop electromagnetic data for magnetic susceptibility and electrical conductivity: *Geophysics*, 68, 1857-1869.

Forrest, M. (2006). Diamond life diamond exploration in Canada: *Materials World*, 14(8), 25-27.

Fraser, D. C., and Hodges, G. (2007). Induction-response functions for frequency-domain electromagnetic mapping system for airborne and ground configurations: *Geophysics*, 72(2), 35-44.

Gerryts, E. (1967). Diamond prospecting by geophysical methods-a review of current practice. *Mining and Groundwater Geophysics. Geological Survey of Canada Economic Report* 26. 439-446.

Golub, G. H., and Reinsch, C. (1970). Singular value decomposition and least squares solution: *Handbook for Automatic Computation, II, Linear Algebra, eds. J. Wilkinson and C. Reinsch, Springer-Verlag, Berlin, Heidelberg, New York.*

Grant, F. S., and Martin, L. (1966). Interpretation of aeromagnetic anomalies by the use of characteristic curves: *Geophysics*, 31, 135-148.

Graybill, F. A. (1975). Introduction to matrices with application in Statistics: *Wadsworth Publishing Co. Inc., Belmont.*

Haber, E., and Oldenburg, D. W. (2000). A GCV based method for nonlinear ill-posed problems: *Computa. Geosci.*, 4, 41-63.

Haney, M., and Li, Y. (2002). Total magnetization direction and dip from multiscale edges: *72nd Annual International Meeting, SEG, Expanded Abstracts,* 735-738.

Hansen, P. C. (1998). Rank-deficient and discrete ill-posed problems: numerical aspects of linear inversion: *Soc. Ind. Appl. Math.*

Hansen, R. O., and Suciu, L. (2002). Multiple sources Euler deconvolution: *Geophysics*, 67, 525-535.

Hargraves, R. B. (1989). Paleomagnetism of mesozoic kimberlites in southern Africa and the cretaceous apparent polar wander curve for Africa. *J. Geophys. Res.,* 949B2 (: 1851-1866.

Hartman, R. R., Teskey, D. J., and Frigdberg, J. L. (1971). A system for rapid digital aeromagnetic interpretation: *Geophysics*, 36, 891-918.

Henderson, R. G., and Zietz, I. (1984). Analysis of total magnetic intensity anomalies produced by point and line sources: *Geophysics*, 13,428-436.

Huang, H., and Fraser, D. C. (1998). Magnetic permeability and electrical resistivity mapping with a multifrequency airborne EM system: *Expl. Geophysics*, 29, 249-253.

Huang, H., and Fraser, D. C. (2001). Mapping of the resistivity, susceptibility and permittivity of the earth using a helicopter-borne EM system: *Geophysics*, 66, 148-157.

Huang, H., and Fraser, D. C. (2002). Dielectric permittivity and resistivity mapping using high-frequency, helicopter-borne EM data: *Geophysics*, 67, 727-738.

Huang, H., and Fraser, D. C. (2003). Inversion of helicopter electromagnetic data to a magnetic conductive layered earth: *Geophysics,* 68, 1211-1223.

Hutchison, R. D. (1985). Magnetic analysis by logarithmic curves: *Geophysics*, 23, 749-769.

Jain, S. (1976). An automatic method of direct interpretation of magnetic profiles: *Geophysics*, 41, 531-541.

Jaques, A. L., Lewis, J. D. and Smith, C. B. (1986). The kimberlite and lamproites of western Australia. *Geological Survey of Western Australia Bulletin* 132.

Keating, P. (1995). A simple technique to identify magnetic anomalies due to kimberlite pipes: *Exploration and Mining Geology,* 4, 121-125.

Keating, P., and Pilkington, M. (2000). Euler deconvolution of the analytic signal: 62nd *Annual International Meeting, EAGE,* Session P0193.

Keating, P., and Sailhac, P. (2004). Use of the analytic signal to identify magnetic anomalies due to kimberlite pipes: *Geophysics*, 69(1), 180-190.

Koulomzine, T., Lamontagne, Y., and Nadeau. A. (1975). New methods for the direct interpretation of magnetic anomalies caused by inclined dikes of infinite length: *Geophysics*, 35, 821-830.

Krishna Singh, S., and Sabina, F. J. (1978). Magnetic anomaly due to a vertical right circular cylinder with arbitrary polarization: *Geophysics,* 43(1), 173-178.

Lawson, C. L., and Hanson, R. J. (1974). Solving least squares problems: *Prentice-Hall, Englewood Cliffs. New Jersey.*

Leite, L. W. B., and Leao, J. W. D. (1985). Ridge regression applied to the inversion of two-dimensional aeromagnetic anomalies: *Geophysics,* 50(8), 1294-1306.

Levenberg, K. (1994). A method for the solution of certain nonlinear problems in least squares: *Quarterly of Applied Mathematics 2,* 164-168.

Lockhart, G., Grutter, H., and Garlson, J. (2004). Temporal, geomagnetic and related attributes of kimberlite magmatism at Ekati, Northwest Territories, Canada: *Lithos,* 77, 665-682.

Lines, L. R., and Treitel, S. (1984). Tutorial a review of least-squares inversion and its application to geophysical problems: *Geophysical Prospecting,* 32, 159-186.

Li, X. (2006). Understanding 3D analytic signal amplitude: *Geophysics,* 71, No.2 P. L13-L16.

Li, Y., and Oldenburg, D. W. (1993). 3-D inversion of dc resistivity data using an L-curve criterion. 69th *Ann. Internat. Mtg, Soc. Expl. Geophys., Expanded Abstracts*, 251-254.

Li, Y., and Oldenburg, D. W. (1996). 3-D inversion of magnetic data: *Geophysics* 61(2), 394.

Macnae, C. J. (1979). Kimberlite and exploration geophysics: *Geophysics* 44, 1395-1416.

Macnae, C. J. (1995). Application of geophysics for the detection of kimberlites and lamproites: *Journal of Geochemical Exploration* 53, 213-243.

Marquardt, D. W. (1963). An algorithm for least-squares estimation of non-linear parameters, *J. SIAM,* 11,431-441.

Menichetti, V., and Guillen, A. (1983). Simultaneous interactive magnetic and gravity inversion: *Geophysical Prospecting,* 31, 929-944.

Mitchell, R. H. (1986). Kimberlites: mineralogy, geochemistry and petrology. *New York: Plenum Press.*

Mitchell, R. H., and Bergman, S. C. (1991). Petrology of lamproites: *New York: Plenum Press.*

Nabighian M. N. (1972). The analytic signal of two-dimensional magnetic bodies with polygonal cross-section-its properties and use for automated anomaly interpretation: *Geophysics,* 37, 507-517.

Nabighian M. N. (1974). Additional comments on the analytic signal of two-dimensional magnetic bodies with polygonal cross section: *Geophysics,* 39(1), 85-92.

Nabighian M. N. (1984). Toward a three dimensional automatic interpretation of potential field data via generalized Hilbert transforms-fundamental relations: *Geophysics,* 49, 780-786.

Nabighian M. N., and Hansen, R. O. (2001). Unification of Euler and Werner deconvolution in three dimensions via the generalized Hilbert transform: *Geophysics,* 66, 1805-1810.

Nabighian M. N., Grauch, V. J. S., Hansen, R. O., LaFehr, T. R., Li, Y., Perice, J. W., Phillips, J. D., and Ruder, M. E. (2005). 75th anniversary the historical development of the magnetic method in exploration: *Geophysics,* 70, No. 6, P. 33ND-61ND.

Naudy, H. (1971). Automatic determination of depth on aeromagnetic profiles: *Geophysics,* 36, 717-722.

Nixon, P. H. (1981). Regional diamond exploration-theory and practice: *J.E. Glover, D.I. Groves (Eds.), Kimberlites and Diamonds, Special Publication of the University of Western Australia Extension Service (1980)*, pp. 64–80.

O' Brien, D. P. (1972). CompuDepth, a new method for depth-to-basement computation: *Presented at the* 42nd *Annual International Meeting, SEG.*

Paige, C. C., and Saunders, M. A. (1982). Algorithm 583, LSQR: Sparse linear equations and least-squares problems: *ACM Trans. Math. Software*, 8, 195-209.

Paine, J., Haederle, M. Et Flis, M. (2001). Using transformed TMI data to invert for remanently magnetised bodies: *Exploration Geophysics*, 32, 238-242.

Parker, R. L. (1972). The rapid calculation of potential anomalies: *Geophysical Journal of the Royal Astronomical Society*, 31, 447-455.

Paterson, N. R., Kwan, K. C. H., and Reford, S. W. (1991). Use of Euler deconvolution in recognizing magnetic anomalies of pipe-like bodies: *61st Annual International Meeting Society Exploration Geophysicists, Expanded Abstracts*, 642-645.

Paulo T. L. (2007). Case history kimberlite exploration at Serra da Canastra province, Brazil: *Geophysics* 72:3: p. M1-M5.

Pedersen, L. B. (1979). Constrained inversion of potential field data: *Geophysical Prospecting,* 27, 726-748.

Phillips, J. D. (1979). ADEPT: A program to estimate depth to magnetic basement from sampled magnetic profiles: *U.S. Geological Survey Open File Report*, 79-367, 1-35.

Pilkington, M., and Crossley, D. J. (1986). Determination of crustal interface topography from potential fields: *Geophysics,* 51, 1277-1284.

Pilkington, M. (1997). 3-D magnetic imaging using conjugate gradients: *Geophysics*, 62, 1132-1142.

Power, M., Belcourt, G., and Rockel, E. (2004). Geophysical methods for kimberlite exploration in northern Canada. *Leading Edge (Tulsa, OK)*, 23(11), 1124-1129.

Raiche, A. (2001). Choosing an AEM system to look for kimberlite-a modeling study: *Exploration Geophysics,* 32, 001-008.

Reid, A. B., Allsop, J. M., Granser, H., Millett, A. J., and Somerton, I. W. (1990). Magnetic interpretation in three dimensions using Euler deconvolution: *Geophysics*, 55, 80-91.

Reynolds, R. L., Goldhaber, M. B., and Snee, L. W. (1997). Paleomagnetic and ^{40}Ar / ^{39}Ar results from the Grant intrusive breccia and comparison to the Permian Downeys Dluff sill-evidence for Permian igneous activity at Hicks Dome, southern Illinois Basin: *U.S. Geological survey bulletin*: 2094-G.

Roest, W. R., Verhoef J., and Pilkington, M. (1992). Magnetic interpretation using the 3D analytic signal: *Geophysics*, 57, 116-125.

Roest, W. R., and Pilkington, M. (1993). Identifying remanent magnetization effects in magnetic data: *Geophysics*, 58, 653-659.

Singh, S. K., and Sabina, F, J. (1978). Magnetic anomaly due to a vertical right circular cylinder with arbitrary polarization. *Geophysics*, 43(1), 173-178.

Sarma, B. S. P., and Verma, B. K. (1996). Negative magnetization contrast in kimberlite search, *Expl. Geophys.*, 26, 31-34.

Sarma, B. S. P., Verma, B. K., and Satyanarayana, S. V. (1999). Magnetic mapping of Majhgawan diamond pipe of central India: *Geophysics* 64: 6: 1735-1739.

Sharma, P. V. (1997). Environmental and engineering geophysics: *Cambridge University Press*.

Shearer, S., and Li, Y. (2004). 3D Inversion of Magnetic Total Gradient Data In the Presence of Remanent Magnetization: *Soc. Expl. Geophys.*, 2004-0774.

Shearer, S. (2005). Three-dimensional Inversion of Magnetic Data in the Presence of Remanent Magnetization. *Master Thesis, Department of Geophysics, Colorado School of Mines*.

Skinner, E. M. W. (1986). Contrasting group 1 and group 2 kimberlite petrology, towards a genetic model for kimberlites: 4th *International Kimberlite Conference, Geological Society Australia, Extended Abstract Series,* n. 16, 202-204.

Smellie, D. W. (1956). Elementary approximations in aeromagnetic interpretation: *Geophysics*, 21, 1021-1040.

Smith, R. S., Annan, A. P., Lemieux, J., and Pedersen, R. N. (1996). Application of a modified GEOTEM system to reconnaissance exploration for kimberlites in the point lake area, NWT, Canada: *Geophysics*, 61(1) 82-92.

Thompson, D. T. (1982). EULDPH-a new technique for making computer-assisted depth estimates from magnetic data: *Geophysics,* 47, 31-37.

Thurston, J. B., and R. S. Smith, R. S. (1997). Automatic conversion of magnetic data to depth, dip, and susceptibility contrast using the SPI method: *Geophysics,* 62, 807-813.

Thurston, J., J.-C. Guillon, and Smith, R. (1999). Model-independent depth estimation with the SPI method: 69th *Annual International Meeting, SEG, Expanded Abstracts,* 403-406.

Thurston, J. B., Smith, R. S. and Guillon, J.-C. (2002). A multimodel method for depth estimation from magnetic data: *Geophysics,* 67, 555-561.

Uchida, T. (1993). Smooth 2-D inversion for magnetotelluric data based on statistical criterion ABIC: *J. Geomag. Geoelectr.,* 45, 841-858.

Wang, X., and Hansen, R. O. (1990). Inversion for magnetic anomalies of arbitrary three-dimensional bodies: *Geophysics,* 55, 1321-1326.

Ward, S. H., and Hohmann, G. W. (1988). Electromagnetic theory for geophysical applications, in Ed., Nabighian, M. N., Electromagnetic methods in applied geophysics: *Soc. Expl. Geophys.*, 131-311.

Whitehill, D. E. (1973). Automated interpretation of magnetic anomalies using the vertical prism model: *Geophysics*, 38, 1070-1087.

Vozoff, K., and Jupp, D. L. (1975). Joint inversion of geophysical data: *Geophys. J. R. Astr. Soc. 1975, 42*: 977-991.

Zeyen, H., and Pous, J. (1991). A new 3D inversion algorithm for magnetic total field anomalies: *Geophysical Journal International,* 104 583-591.

Zeyen, H., and Pous, J. (1993). 3D joint inversion of magnetic and gravimetric data with a priori information: *Geophysical Journal International* 112, 224-256.

Zhang, Z., and Oldenburg, D. W. (1996). Simultaneous reconstruction of 1-D susceptibility and conductivity from electromagnetic data: *Geophysics,* 64, 33-47.

Zhdanov, M. S., and Pavlov, D. A. (2001). Analysis and interpretation of anomalous conductivity and magnetic permeability effects in time domain electromagnetic data: Part II: $S\mu$-inversion: *J. Appl. Geophysics.*, 46, 235-248.

Zietz, I., and Andreasen, G. E. (1967). Remanent magnetization and aeromagnetic interpretation: *Mining Geophysics,* 2, 569-590.